Ultrafast carrier dynamics investigated by a novel *Pump-and-Probe-Terahertz* technique

Dissertation

zur Erlangung des akademischen Grades
doctor rerum naturalium (Dr. rer. nat.)

vorgelegt dem Rat der
Physikalisch–Astronomischen Fakultät
der Friedrich–Schiller–Universität Jena

von Hagen Wald
geboren am 25. Juli 1971 in Mühlhausen

Contents

1 Introduction

The development of laser systems capable to generate pulses as short as a few femtoseconds ($1\ fs \sim 10^{-15} s$) led to a rapid movement in the field of ultrafast carrier dynamics in different material classes. To improve semiconducting microelectronic devices like transistors, an understanding of the various processes of the charge carrier dynamics is necessary. For example, the maximum attainable speed of gallium arsenide field- effect- and heterojunction-bipolar transistors is limited by the rate at which electrons transfer between the high-mobility and low-mobility regions in the conduction band. Therefore the investigation of the excitation of semiconducting materials out of their equilibrium and subsequent relaxation has become a key area of semiconductor research [Otho 98]. Research groups investigate processes like carrier momentum relaxation, carrier thermalization, energy relaxation, and carrier trapping by excite-and-probe-(or pump-and-probe-) techniques with a resolution limited only by the excitation pulse width [Hu 95]. Different kinds of experimental methods base on this experimental concept: pump-probe-transmission- (and reflection-), time-resolved up-conversions luminescence-, and pump-probe-Raman scattering experiments are examples of these techniques.
In this work a novel pump-and-probe method is proposed: the *pump-and-probe-THz* technique (PPT). This method is used to investigate the ultrafast carrier dynamics of two important materials for high-speed electronical devices: the semiconductor $GaAs$ and the cuprate superconductor $YBa_2Cu_3O_{7-\delta}$.
Concerning the carrier dynamics of GaAs the following physical problems were investigated:

- determination of the carrier relaxation time of low-temperature grown GaAs;
- investigation of the electric field dependence of the carrier recombination process;
- observation of the carrier trapping and the influence of the mid-gap states on the carrier relaxation;
- determination of the dependence of the carrier relaxation on the optically induced carrier density;
- investigation of the possibility of a direct observation of the velocity overshoot effect in GaAs.

A requirement of the PPT method is the capability of the investigated material to emit electromagnetic pulses with duration of at most a few picoseconds ($1\ ps \sim 10^{-12} s$) after fs optical illumination. Therefore the dark resistivity of the semiconducting material has to be very high and its free carrier life time has to be sufficiently short.
The reduction of the geometrical size of microelectronic devices to increase the process

speed and the chip integration owns a physical limitation. Therefore in the future alternative device concepts are necessary and one of them is the usage of superconducting logical devices like the rapid single flux quantum logic (RSFQ), using the single flux quantum as a bit. Another reason to look for possibilities of low power loss solutions is the high energy consumption of electronic devices, which is rapidly increasing further.
Materials with a very low power loss even at high frequencies and which are also capable of THz pulse emission are the cuprate superconductors [Bedn 86]. The discovery of superconductivity of the cuprate ceramics made these materials more interesting for applications, because of the increased device operating temperature compared to low-T_C superconductors. Cuprate superconductors are therefore usually referred to as high-temperature superconductors.

Investigations over the past several years have resulted in a significant improvement in the knowledge of the properties of the cuprate superconductors. Nevertheless the carrier dynamics of these materials is still subject of intensive research. Compared to semiconductors their nonequilibrium physics is more difficult to analyze, because of the existence of different charge carriers: superconducting holes/electrons and electron-/hole-like excitations (quasiparticles). The electron density of states of these materials below the critical temperature is modified by a superconducting gap. The structure of this energy gap in the k-space as well as the detailed energy band structure are still not completely understood by now. The Bardeen-Cooper-Schrieffer-(BCS-) theory describes the equilibrium case of a superconductor in which all carriers are in equilibrium not only with each other but also with the crystal lattice [Schm 97]. The investigation of the nonequilibrium properties of superconductors, the processes of electron thermalization and relaxation back to equilibrium, provides an insight into the mechanism of superconductivity and the know-how, which is necessary for many applications of these materials, e.g. high sensitive detectors. Furthermore many cryoelectronic devices operates under conditions far from the equilibrium.

It was suggested that cuprate superconductors exhibit a relatively strong electron-phonon interaction [Gork 88], [Cohe 90], which is responsible for the ultrashort response time after quasiparticle excitation due to an optical illumination. For this reason much attention has been focused on investigations in this area using ultrashort laser pulses to excite the superconductor from the equilibrium state and observe the relaxation dynamics: time resolved reflectivity measurements [Han 90], [Chwa 90], transient photoimpedance measurements [Bluz 91], [Fren 93], thermal difference reflectance spectra measurements [Holc 94], bulk electric-quadrupol magnetic-dipole optical rectification measurements [Side 99], infrared mixing experiments [Lind 94] and terahertz emission observations [Hang 96], [Hegm 95], [Jaek 96] are examples of these studies.

The investigations of this work concern the cuprate superconductor $YBa_2Cu_3O_{7-\delta}$ (YBCO), which became a standard material under the cuprates, because of the easy deposition of high crystalline YBCO thin films with good properties. The PPT method is putted forward to investigate the nonequilibrium state of YBCO at low temperatures by introduction of a cryostat in the experimental setup. The scientific questions, which will be elucidated by using this novel technique, are the following:

- For an application of YBCO devices as THz emitters high radiation efficiency is appreciated. Therefore in this work it is tried to increase the emitted THz power by increasing the output coupling at the superconductor-substrate interface and analyze the observed effect on the THz radiation.

- A peak in the real part of the conductivity of YBCO at temperatures well below T_C is observed by microwave experiments and time domain spectroscopy (TDS), which is supposed to be caused by an increase in the quasiparticle scattering time [Nuss 91], [Bror 96]. Therefore the temperature dependence of the scattering time of the quasiparticles is investigated.
- Important for the superconducting mechanism are the different kinds of scattering experienced by the charge carriers. A mediation of superconductivity by phonons or spin fluctuation exchange will influence the scattering in the materials and can be measured by the scattering rate and its temperature dependence compared to recent theories [Wilk 00].
- A possible saturation of the PPT signal at higher laser powers reveals information on carrier trapping mechanisms in the YBCO, which could be a limit for some applications.
- The new possibility of the PPT experiment to observe directly and time-resolved the vortex dynamics inside of an YBCO microbridge is of fundamental interest especially for RSFQ electronics. The flux velocity is measured directly and a threshold of the optical activation of flux lines in the YBCO film is observed.

This work is arranged in the following way:

Chapter 2: This chapter introduces the materials GaAs and YBCO. The band structures of both materials are described. An overview over their existing and proposed applications is given to elucidate the motivation of ultrafast time resolved measurements of the optical response and the high frequency properties of these materials.

Chapter 3: The carrier dynamics of YBCO and GaAs are introduced in this chapter. Charge carrier excitation and relaxation, carrier trapping and polarization in external fields and the effect of photoconductivity in semiconductors are briefly described. The *two-fluid model*, which is widely used to explain the carrier transport in superconductors, the influence of the *d-wave symmetry* of the superconducting gap on the scattering rate, the *weak coupled model*, the electron-phonon coupling and the kinetics of quasiparticle excitation described by rate equations (Rothwarf-Taylor-equations [Roth 67]) are treated. To analyze the critical current density of the superconducting devices, equations of the *Anderson-Kim model*, which assumes that flux-creep contribute mainly to the critical current density, are used.

Chapter 4: The experimental setup of the terahertz- (THz-)emission and the novel PPT-experiment of this work are described in detail in this chapter. The Ti:sapphire laser as source of the femtosecond pulses, the photoconductive switches as THz detectors, the THz field optics, the YBCO THz emitters, their operating principle and properties are introduced.

Chapter 5: The results of the time resolved THz emission experiments of semiconducting low-temperature grown GaAs (LT-GaAs) and superconducting YBCO are summarized in this chapter. The dependence of the THz signal on the pump power, the bias current/voltage and the temperature is observed. The influence of carrier doping with Pr in YBCO on the emission efficiency is investigated.

Chapter 6: The results of the novel PPT method on LT-GaAs and the worldwide first results on the material YBCO are summarized in this chapter. The bias current/voltage, temperature and laser pump power dependencies are shown and compared to theoretical models. Carrier scattering and recombination times with trapping effects in the case of LT-GaAs are explained by statistical rate equations [Otho 98] and the *Drude*-model. The possibility of the direct observation of a velocity overshoot effect in GaAs is mentioned.
In the case of superconducting YBCO the quasiparticle excitation and subsequent scattering and recombination to form Cooper pairs can be observed. It is unique to this technique that the response of the superconductor to a THz signal *and* to a femtosecond signal can be observed at the same time. Quasiparticle scattering rates at THz frequencies are measured and compared to results of TDS experiments by other groups ([Wilk 00] and [Bror 96]). Different models (*weak coupling model*, *two-fluid model*) are used to explain the temperature dependence of the observed scattering rates and the PPT signals. Quasiparticle relaxation and recombination to Cooper pairs after femtosecond optical illumination is additionally observed and compared to results of optical pump-and-probe methods ([Han 90] and [Kaba 99]).

Chapter 7: In the last chapter the results of the measurements, a prospect of the possibilities, the advantages and disadvantages of the PPT method are summarized.

2 The Investigated Materials and their Applications

In this work the PPT-technique is proposed as a novel tool to investigate the ultrafast carrier dynamics in semiconductors and cuprate superconductors. This chapter summarizes the most important properties and applications of the investigated materials which motivated the experiments. The compound gallium arsenide (GaAs) as a semiconducting material and the ceramic $YBa_2Cu_3O_{7-\delta}$ (YBCO) as a cuprate superconductor are used as examples for the investigation.

2.1 The Material GaAs

GaAs is a typical III-V direct band gap semiconductor in a mixed *ionic-covalent* bond. One electron moves from Ga to As leading to an *ionic* structure Ga^+As^- and an additional *covalent* portion resulting in the typical sp^3 bond and a tetrahedral crystal structure of the ZnS-type. The gap energy at room temperature is $E_g = 1.43\ eV$. The direct band gap and the availability of high quality crystals made GaAs to the material of choice in studying ultrafast carrier dynamics.
Fig. 2.1 shows a schematic of the band structure of GaAs. The top of the *valence band* is fourfold degenerated at k = 0 (Γ point).

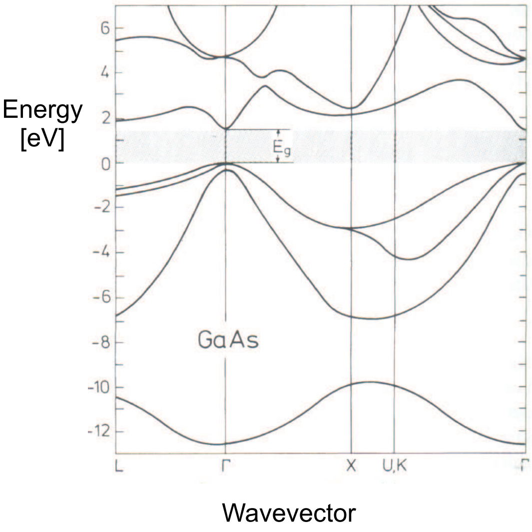

Fig. 2.1: The schematic band structure of GaAs.

Away from the Γ-point the degeneracy is lifted and there are two twofold degenerated bands: the upper heavy-hole band and the lower light-hole band. Below the top of the

Property	Reported data
gap energy (T = 300 K)[1]	1.43 eV
gap energy (T ≈ 0 K)[3]	1.52 eV
spec. resistivity ρ (T = 300 K)[4]	$> 10^7 \Omega m$
effective electron mass m_e^*[1,3]	$0.07 \cdot m_e$
eff. heavy hole mass m_{hh}^*[3]	$0.5 \cdot m_e$
eff. light hole mass m_{lh}^*[3]	$0.08 \cdot m_e$
eff. split-off hole mass m_{soh}^*[3]	$0.15 \cdot m_e$
static dielectric constant ϵ[1]	12.3
intrinsic carrier density n_i[2]	$9.2 \cdot 10^{-6} cm^{-3}$
electron mobility μ_e[2]	$8800\ cm^2/Vs$
hole mobility μ_h[2]	$450\ cm^2/Vs$
split-off energy[3]	0.34 eV

Table 2.1: Some properties of GaAs taken from [1][Osba 97]; [2][Hins 96]; [3][Ibac 99]; [4][Sze 96].

valence band lies a twofold degenerated band termed the spin-orbit split-off band. There are two sets of satellite conduction band valleys: the L-valley (minima at boundary of Brillouin-zone in the (111) direction) and the X-valley (minima at the Brillouin-zone edges in the (100) directions). Table 2.1 shows some properties of GaAs.

2.1.1 Low-Temperature Grown GaAs

GaAs thin films are usually grown by molecular beam epitaxy. If the temperature during the film deposition is reduced to about 200 - 300°C under arsenic overpressure an incorporation of excess group V-atoms (As) occurs. Post annealing at temperatures above 600° leads to the nucleation of the excess arsenic in crystalline As precipitates of several nanometer size [Luys 98]. These As clusters act as burried Schottky barriers, form localized mid-gap states and are responsible for trapping of electrons and holes [Sieg 96]. Another type of trapping centers are point defects, which are incorporated during the growth process. They are double donors, which consist of neutral and positively charged arsenic antisites. Energetically the antisite states are localized close to the center of the band gap [Witt 93]. The charged antisites as well as the precipitates are believed to influence the electrical properties of the material and the carrier relaxation after optical excitation [Segs 02]. Due to the fast carrier trapping the carrier lifetime of such low-temperature grown (LT-)GaAs is only about 250..500 fs [Tani 94], [Gren 97] and depends critically on the growth temperature.

The trapping states may consist of Urbach tail states, which are located energetically close to the conduction band edge and the mid-gap states, mentioned above [Segs 02]. The Urbach tail states are caused by disorder in the material, while the mid-gap states formed by the arsenic precipitates and the defects. In LT-GaAs the mid-gap state concentration can be as high as $10^{20} cm^{-3}$ after growth [Otho 98], but decreases while the subsequent annealing to values of about $5 \times 10^{17} cm^{-3}$ to $5 \times 10^{18} cm^{-3}$ depending on

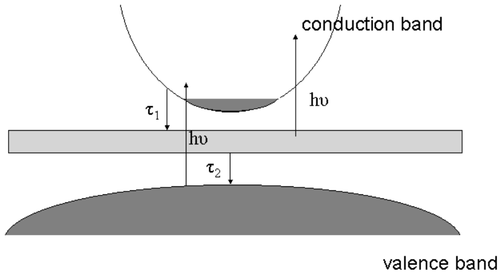

Fig. 2.2: The schematic band structure of LT-GaAs with trapping states and the characteristic relaxation times indicated.

growth and annealing temperature [Look 93], [Pfei 00], [Liu 94]. At high injected carrier densities a saturation of the trapping can occur and therefore the slow recombination of the trapped carriers (τ_2 in fig. 2.2) acts as a bottleneck for the depopulation of the bands via the point defects.

High epitaxial GaAs crystals, grown under standard conditions (not LT-GaAs), exhibit a typical electron-hole recombination time of about 100..500 ps [Otho 98]. Therefore it is obvious that localized states in the energy gap due to defects or impurities (trapping states) can act as recombination centers for non-radiative processes, which change the recombination time substantially. If the density of trapped states is sufficiently high, carriers can tunnel through these centers to the *valence band*. Because the trapping of carriers due to these localized states occurs very fast, the recombination time is reduced to about 10 ps [Segs 97].

This effect is important for the development of fast photoconductive switches with sub-picosecond response times, which can be used for THz pulse emission [Smit 88]. With a bandwidth extending up to 5 THz and a good signal-to-noise ratio, such THz pulses are a promising tool for far-infrared spectroscopy of solids, liquids, and gases. However due to the introduced defects and impurities the statistical probability of scattering is increased and the mobility of the carriers is therefore reduced, what causes an increase in resistivity. This leads on the opposite side to a decrease in the sensitivity of the device to external electrical fields.

2.1.2 The Gunn Effect

The Gunn effect is connected to interband scattering of hot carriers in GaAs, while an electrical field is applied. If the energy is high enough, carriers are scattered to the energetically upper bands next to the Γ valley, the X- and L-valley. The effective mass m^* of the carriers is higher there, and this redistribution of the carriers to the band edges of the different valleys leads to a reduction of the conductivity. The saturation velocity $\vec{v}_s$ of free electrons with the effective mass m^* is given by:

$$\vec{v}_s = \frac{e\vec{E}_{loc}\tau_{rel}}{m^*}. \tag{2.1}$$

If the field strength in GaAs is increased to values of about $3 \cdot 10^3 Vcm^{-1}$ the drift velocity reaches a maximum and decreases with higher field strength (fig. 2.3). The reason for this effect is the above mentioned scattering of electrons (due to phonon emission) from the central Γ valley of the band to a neighbor valley with a higher effective mass and a lower saturation velocity. Therefore an area of negative differential conductivity exists above a critical value of the electrical field strength. Such states of negative differential conductivity are not stable. This effect is also called the *velocity overshoot* effect, because the carriers which are scattered to the side valleys (and own a higher drift velocity) are slowed down. Fig 2.3 indicates the dependence of the drift velocity of some important semiconductors on the applied electrical field. For GaAs a peak in the drift velocity is observed at electric field strength of about 2 kV/cm. This peak is connected to the velocity overshoot effect in GaAs.

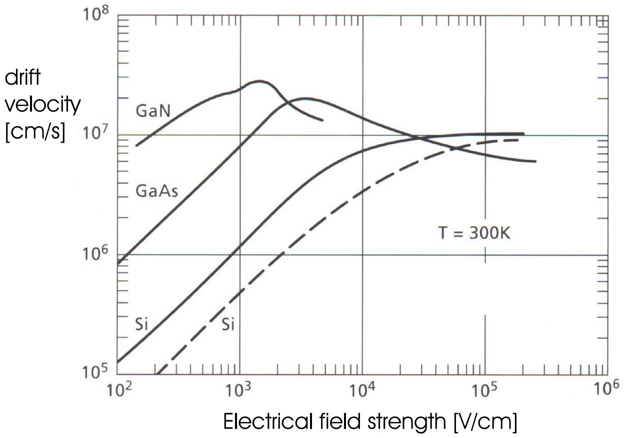

Fig. 2.3: The drift velocity as function of the electric field strength for GaAs, GaN, Si [Ibac 99].

To observe the *velocity overshoot* the carrier density must be low enough to get larger scattering times of the carrier-carrier scattering τ_{rel} [Jeps 96]. Therefore this effect is only observed at low optical induced carrier densities (below about $5 \cdot 10^{16} cm^{-3}$). Another requirement to observe the effect is that the energy difference between the center Γ valley and the neighbor valleys is not too small, so carriers cannot be thermal excited to these valleys. On the other side this energy difference should not be too large, so enough hot carriers can be scattered. This effect is only observed in direct band gap semiconductors.

2.1.3 Applications of GaAs

GaAs is one basic material for fast electronic, opto-electronic and microwave devices (like *Gunn-diodes* and *Gunn-oscillators*) and therefore an investigation of its carrier dynamics is interesting. The high dark resistivity, high carrier mobility and subpicosecond response time make LT-GaAs an interesting material for ultrafast, laser activated switches and photodetectors [Otho 98]. Another application of LT-GaAs is the usage as electric insulator in microelectronics [Mell 95]. In laser science, the carrier trapping time in LT-semiconductors determines the recovery time of fast saturable absorbers, which are used to generate picosecond and femtosecond pulses with solid-state lasers [Brov 95]. Another important application is the photoconductive mixing in LT-GaAs, which generates a THz difference frequency from two single-frequency tunable lasers and makes widely tunable optoelectronic sweepers possible [McIn 95]. This opens opportunities of coherent sources for high-resolution molecular spectroscopy [Pine 96], optical-heterodyne converters for frequency meterology of visible and near-infrared lasers [Walt 96] and local oscillators for superconducting bolometric mixers [Golt 95] or superconductor-insulator-superconductor mixers. Important advantages of LT-GaAs to other photoconductors are the high electrical breakdown field of about $> 5 \cdot 10^5\ Vcm^{-1}$ and the relatively high mobility of about $> 200\ cm^2V^{-1}s^{-1}$ for photoexcited electrons, depending on the photon energy [Brow 93].

2.2 The Material YBCO and its Band Structure

The material $YBa_2Cu_3O_{7-\delta}$ (YBCO, Y123) in its orthorhombic crystalline form is a superconductor with a transition temperature of about 90 K [Wu 87]. The crystal structure of YBCO consists of three perovskite units on top of each other: the top unit $BaCuO_2$ and bottom unit $BaCuO_3$ encloses a Ba atom and the center unit $YCuO_2$ an Y atom, see fig. 2.4. The corner Cu is surrounded by O forming either CuO_2-planes or CuO-chains. Besides the orthorhombic phase of YBCO there exist a tetragonal crystal structure, which does not show superconductivity. The oxygen content and order of the material has a critical influence on the electronical properties of it. In the tetragonal phase the oxygen sites in the chain layer are about half occupied in a random disordered manner. In the orthorhombic phase these oxygen atoms are ordered into -Cu-O- chains

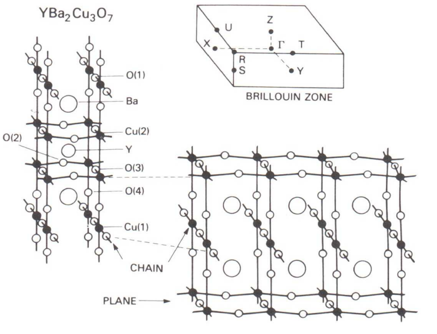

Fig. 2.4: A schematic picture of the YBCO unit cell and a sketch of the corresponding Brillouin zone [Pool 95].

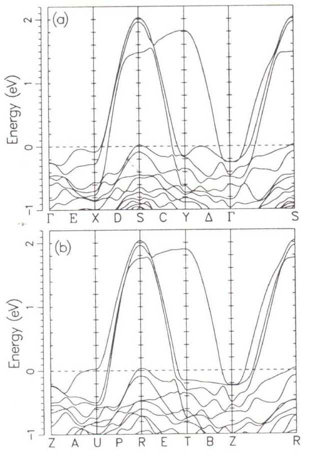

Fig. 2.5: The energy band structure of YBCO.

along the b direction and here the oxygen vacancies along the a direction causes the unit cell to compress slightly so that $a<b$ [Pool 95p185].
In order to form chain-bonds electrons are moved to the chains and dragged out of the planes, leaving mobile holes behind. The CuO_2 planes are therefore metallic conducting (YBCO is a hole-conductor) and a part of these holes build up Cooper pairs when T drops below T_C [Bror 96]. Both, the copper oxide chains and planes, contribute to the superconducting properties. The transition temperature T_C depends on the oxygen concentration in the chains and with decreasing oxygen content it decreases, until for $\delta > 0.64$ the material no longer superconducts [Ye 95]. This behavior is accompanied by a transition from the orthorhombic structure to the tetragonal structure, where $a=b$, and can be adjusted by the deposition parameters. Common property of all cuprate oxide high-T_C materials is the layered, strong anisotropic structure with at least one CuO_2 plane, which causes the strong anisotropic electronic properties.
The band structure of YBCO along the directions connected to the symmetry points Γ, X, Y, and S in the central horizontal plane of the Brillouin zone ($k_z = 0$) is shown in fig. 2.5 [Pick 90]. It reflects the principle features of the compound: the two CuO_2 planes containing the Cu(2),O(2) and O(3) atoms, and a third plane containing chains of Cu(1)-O(1) atoms along the b-direction. The orthorhombic Brillouin zone, indicated in fig. 2.4, has a height-to-width ratio

$$\frac{2\pi}{c} \cdot \frac{a}{2\pi} = \frac{a}{c} \approx 0.33, \tag{2.2}$$

which is the reciprocal of the height-to-width ratio of the unit cell in coordinate space. The two narrow CuO plane-related bands in fig. 2.6 strongly dispersed, i.e., rising far above the Fermi surface at the corner points S and R of the Brillouin zone. These bands are almost identical, resembling the so called Hubbard band. The broader chain band, that is dispersed in the chain directions S and Y (also in R and T) far above the Fermi energy arises from the Cu-O sigma bonds along the chains formed from the oxygen p_y and copper $d_{x^2-y^2}$ orbitals. Another chain band undergoes only little dispersion, staying close to the Fermi surface, but rises slightly above the Fermi energy at S and R. Oxygen deficiency depopulates the chains, and this is reflected in the absence of chain bands in the semiconducting compounds [Yu 87].
The low dispersion in the bands along the k_z direction means that the effective mass m^* in this direction is very large and since the electrical conductivity is low along the c-direction. In contrast, the plane and chain bands appear parabolic in shape along k_x and k_y, corresponding to a much lower effective mass. This explains the observed anisotropy in the normal-state electrical conductivity.
The total density of states (DOS) and the contribution of the copper and oxygen is shown in fig. 2.6. There exist *van Hove singularities* in the partial DOS of the planar O(2) and O(3) at energies at which the planar Cu(2) atoms also have peaks, whereas the chain Cu(1) have peaks that match with those of the O(1) and O(4) oxygens bonded to it. This suggests that the planes and chains are partially decoupled from each other. Supercurrent can flow along both the chains and the planes [Pool 95].
Information of the charge distributions around the atoms can be obtained from the knowledge of the energy bands. This is carried out by a Fourier transformation from the reciprocal k space to the coordinate space, see fig. 2.7. The high density at the Y^{3+}

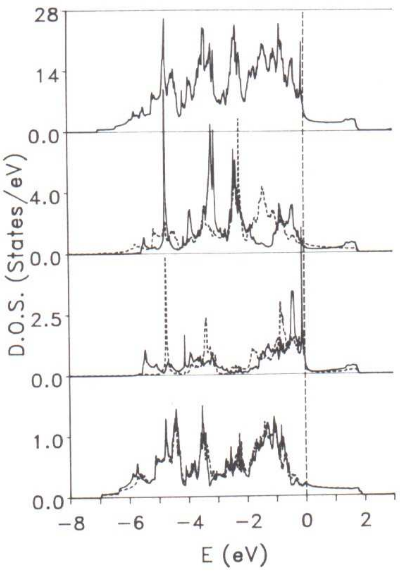

Fig. 2.6: The top panel gives the total DOS of YBCO, the second panel gives the partial DOS of Cu(1) (solid line) and Cu(2)(dashed line), the third O(1) and O(4) and the bottom panel gives O(2) and O(3) [Krak 88].

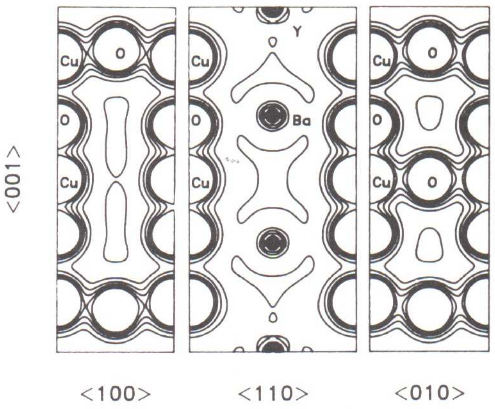

Fig. 2.7: The charge density of YBCO in three symmetry planes, indicated in the figure. The results are obtained from band structure calculations [Krak 88].

and the Ba^{2+} sites and the lack of contours around these sites indicate that these atoms are almost completely ionized and decoupled from the planes above and below. This accounts for the magnetic isolation of the Y site whereby magnetic ions substituted for yttrium do not interfere with the superconducting properties. In contrast, the contours surrounding the Cu and O atoms are not characteristic of an ionic bond. The short Cu-O bonds in the plane and chains (0.193-0.196 nm) increase the charge overlap. The least overlap appears in the Cu(2)-O(4) vertical bridging bond. Therefore the Cu-O bonds are partly ionic and partly covalent.

2.2.1 The Material YPBCO

It is reported that the critical temperature of the superconductor $Y_xPr_{1-x}Ba_2Cu_3O_7$ (YPBCO) decreases from the value of pure YBCO (90 K) with an increasing Pr content until the sample no longer superconducts at around 50% of Pr substitution [Rado 95]. At the same time the normal resistance increases with increasing Pr content. The optical induced transient reflectivity change of YPBCO thin films investigated by means of a time resolved pump-and-probe method differs significantly from that of YBCO thin films [Nash 00], [Kaze 91]. Superconducting YPBCO has the same orthorhombic structure as YBCO but in contrast it retains the full stoichiometric oxygen content. By varying the Pr content the superconducting properties can be influenced without causing changes in the crystal symmetry. Brorson *et al.* used YPBCO for TDS measurements of the complex transmission coefficient [Bror 96]. They reported an increase in the transmittance of YPBCO thin films in the THz frequency range with an increasing content of Pr atoms for temperatures between 10 and 300 K. For pure YBCO the BCS-gap value is about $2\Delta(0) = 6.8$ THz $= 28$ meV. For YPBCO the gap size should shrink and could be observable within the spectral range of a THz spectrometer, nevertheless no gap features were measured by the mentioned authors.

Two processes were proposed in the past to be responsible for the change of the superconducting properties of the YPBCO [Bror 96]: a) magnetic pair breaking and b) reduction of mobile holes in the Cu-O planes. In the first case Pr was assumed to enter the YPBCO alloy in the 3+ valence state and therefore it would carry a magnetic moment. In the later case Pr enters the compound in the 4+ valence state and remove mobile holes from the conduction planes. Quantum chemical calculations revealed that the introduction of Pr into the Y-sites leads to a hybridization of the Pr *4f*-level and the O *p*-bands of the planes. This causes the appearance of new unoccupied states above the Fermi level which grab holes out of the CuO_2 planes. The mobile carrier density influences the plasma frequency of the material. TDS measurements observed a decrease of the plasma frequency with increasing Pr content and confirm that the effect of Pr doping is to reduce the mobile carrier density [Bror 96].

The higher transmittance of the YPBCO suggests an increase of the THz radiation efficiency of this material compared to that of pure YBCO under the same conditions of excitation (bias current, laser power, temperature). This fact make the material interesting for further investigations.

2.2.2 Applications of YBCO

The high frequency properties of YBCO make it suitable for applications at microwave frequencies, despite the fact of necessary cooling [Hein 99]. There exist different kinds of such passive and active electronic devices: rapid-single-flux-quantum (RSFQ) logic circuits, transmission lines, microwave antennas, optical modulators and switches (see fig. 2.8), bolometers, frequency mixers, opto-electrical input devices, Josephson junctions (*voltage normal*) and pulsed THz radiation sources.

The possibility of generation, manipulation and detection of high frequency electromagnetic fields of wavelengths λ between around 3 mm (100 GHz, microwaves) and 30 μm (10 THz, near infrared) is of crucial interest for space radiometry, optical communication, thermal imaging, biomedical applications, spectroscopy and pyrometry [Zhan 94a]. Optical detection with YBCO is anticipated because of its low reflectivity (less than 50% [Fren 93]) and high absorption coefficient (α in the order of 10^4 to 10^5 cm^{-1} [Kell 89]) from ultraviolet to infrared. High-T_C superconducting detectors are the most sensitive detectors for radiation at a wavelength longer than 20 μm, which operate at temperatures above 77 K [Rich 89].

The usage of the free propagating THz pulses emitted by photoconducting or superconducting devices as broadband radiation source in a TDS system was proposed by van Exter *et al.* at IBM in 1989 [vanE 89]. Until to date THz TDS has been used to investigate the far-infrared properties of many materials: gases [Hard 91]; dielectrics and semiconductors [Gris 90b]; flames [Chev 98]; liquids [Pede 92] and superconduc-

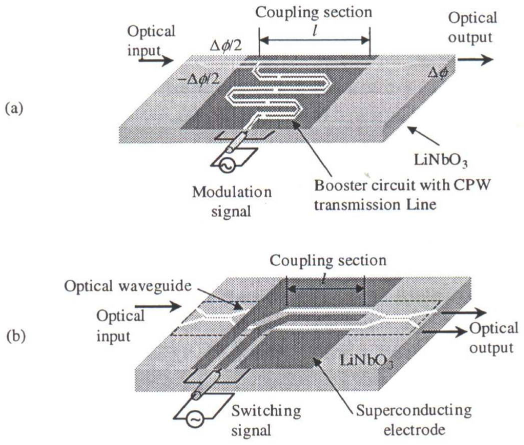

Fig. 2.8: Schematic of a frequency modulator (a) and an optical switch (b).

tors [Nuss 91].

In the area of biotechnology it is important to investigate rotations and oscillations of large organic molecules, which have resonances in the THz frequency range. To analyze such spectrums THz frequency sources of high output power, which are compact and cheap, are necessary. Information about the atomic distances, force constants, order parameters of polymeers, crystal parameters and charge contributions inside of large molecules can be measured using this technique. On the other hand properties of dielectric materials like the dielectric constant ϵ, the complex refractive index n and the complex conductivity can be determined. Therefore with regard to such applications superconducting THz emitters has to be compared to the best pulsed THz sources: semiconducting surface emitters.

For many practical applications and experimental techniques it is impossible or very difficult to utilize single crystals of YBCO. For example high frequency electronics for satellite communications and broad-band high-sensitive photodetectors consist mostly of thin-film structures. For this reasons thin films and thin film devices are investigated in this work.

To exploit the full bandwidth of optical fibers for telecommunications new optoelectronic devices based on the unique properties of the cuprates have been proposed [Bunt 00], [Sobo 01]. They are founded on their ultrafast electrical response that can exceed frequencies of 1 THz. The switching between the electrical behavior of the normal and superconducting state results in corresponding changes of optical transmission in a superconducting thin film and can be used to modulate far-infrared light beams [Puze 93]. This is the concept of the optical modulator by Puzey (fig. 2.8).

Because the PPT technique is introduced here as a novel method to investigate the carrier dynamics of semiconducting and superconducting materials, the materials under investigation are YBCO and LT-GaAs, both very well investigated materials. YBCO is the material of choice because previous reports described the ultrafast carrier dynamics of this material in detail [Bluz 92], [Chwa 90], [Fren 93], [Han 90] and this results can now be compared with the results of our experiments to analyze the data of the novel PPT technique. Another important point is the possibility of the deposition of the superconducting thin films of YBCO and LT-GaAs which exhibit homogeneous high crystalline quality.

3 The Dynamics of Carrier Excitation

In this work the PPT method is used as a novel tool to investigate the carrier dynamics of the in chapter 2 introduced semiconductor LT-GaAs and the cuprate superconductor YBCO on an ultrashort time scale. Therefore before the PPT method is described in more detail in chapter 4, some basic theories of the carrier dynamics of both materials are overviewed in this chapter. Processes, which occur after an excitation of the samples by a femtosecond laser pulse are summarized. The knowlegde of these processes is necessary to explain the measured excitation behavior of the materials.

3.1 Excitation Dynamics in Semiconductors

First an ideal, intrinsic semiconductor is considered, without donor or acceptor centers in the crystal. Under equilibrium conditions electrons and holes in this semiconductor are distributed at the energy states according to Fermi-Dirac statistics and the phonons following the Bose-Einstein statistics. Without external fields carriers and phonons interact via carrier-carrier and carrier-phonon scattering and keep the equilibrium temperature between carriers and lattice. The average momentum of the carrier and phonon systems is zero and the average energy corresponds to the temperature T of the material.
The free electron density n_{free} results from the Fermi-function $f(E,T)$ and the density of states in the conduction band $D_C(E)$:

$$n_{free} = \int_{E_C}^{\infty} D_C(E) f(E,T) dE. \tag{3.1}$$

Illumination of a semiconductor with photons of an energy higher than the band gap energy results in a generation of large nonequilibrium carrier densities and elevated carrier temperatures [Alfa 84]. Depending on the incident fluence and the photon energy, the free carrier density can increase several orders of magnitude and carrier temperatures of several thousands degrees can be reached. The absorption of one photon by an electron in the *valence band* creates a transition from the *valence* to the *conduction band*, leaving a hole in the *valence band*. After the optical excitation electrons and holes undergo a spatial and temporal evolution with characteristic times which depend on different processes, see table 3.1.

Initially the excitation energy of the photons is transfered to the carriers creating a nonequilibrium state of hot carriers with specific momentum and elevated temperature. This process occurs due to an instantaneous polarization of the photoinjected electron-hole pairs in the field of the laser beam [Chua 92], [Kuzn 93]. After a short ballistic regime of carrier acceleration without scattering, the momentum relaxation starts on a femtosecond time scale via elastic and inelastic scattering between the carriers [Otho 98]. The relaxation rate of the momentum and the energy of the carriers to the equilibrium

Microscopic process	Characteristic time /s
carrier-carrier scattering	$10^{-15} - 10^{-12}$
intervalley scattering	$\geq 10^{-14}$
intravalley scattering	$\approx 10^{-13}$
carrier-optical phonon thermalization	$\geq 10^{-12}$
optical phonon-acoustic phonon interaction	$\approx 10^{-11}$
carrier diffusion 100 nm	$\approx 10^{-11}$
Auger recombination	$\approx 10^{-10}$
radiative recombination	$\geq 10^{-9}$
lattice heat diffusion 100 nm	$\approx 10^{-8}$

Table 3.1: Characteristic times of the microscopic processes in semiconductors following optical illumination [Otho 98].

value is determined by the nature of the scattering and the number of processes involved. Excitation by an ultrashort, monochromatic, polarized laser pulse produces distributions of electrons and holes that are narrow in energy and peaked in particular directions of momentum space, see fig. 3.1 a).

Carrier-carrier scattering randomizes the momentum within tenth of femtoseconds (fig. 3.1 a) - b)) and results in a Coulomb thermalization (fig. 3.1 b)-c)). This allows that the carrier distribution can be described by using the Fermi-Dirac distribution function with temperature T_{exc}. The energy relaxation occurs primarily via the emission of optical phonons of small wave-vectors (intravalley scattering) on a time scale of about $10^{-12}s$, fig. 4.1 d) [Otho 98]. Zhou *et al.* have reported that the cooling rate of hot carriers is reduced substantially in precence of nonequilibrium longitudinal optical (LO) phonons [Zhou 92]. The cooling rate in their experiment was determined from femtosecond, time-resolved luminescence spectroscopy. The hot phonons generated during the carrier cooling process will remain for a longer time compared to the hot carrier life time in LT-GaAs. The devay time of the hot phonon relaxation was determined to be about 4 ps. The free electrons in the conduction band can as well interact with large wave-vector phonons and be scattered from the central valley to various side valleys (intervalley scattering) [Seeg 88]. Depending on the induced carrier density, electron-hole recombination occurs on a time scale of about 100 ps via the Auger process or other recombination processes, which can take place on even longer time scales and do not have to be considered here, because the observation of the described PPT experiments are on a time scale of 50 ps at maximum. The absorption of visible light occurs in GaAs over a depth of about 0.1 μm at 800 nm wavelength. Most of the free carriers are generated in this surface-near region and this leads to a carrier diffusion, depending on the carrier temperature T_{exc}. The diffusion time is reported to be about 10 ps for a 100 nm diffusion length. The initial rise in carrier temperature due to the excess kinetic energy causes a substantial increase in the diffusion coefficient and a rapid movement of the carriers out of the surface region [Otho 91]. The diffusion persists until the spatial inhomogeneity of carrier temperature in the surface region returns to equilibrium.

In the simpliest case the excitation of electrons from the valence band to the conduction band due to a pump pulse can be approximated by a differential rate equation with a

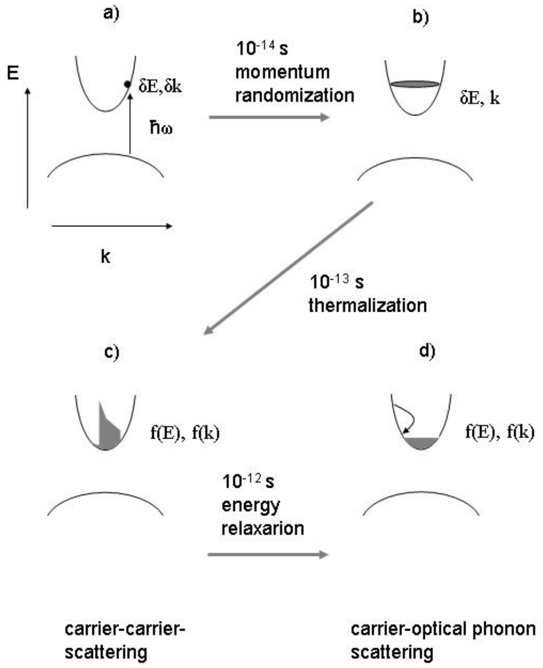

Fig. 3.1: Schematic diagram of the photoexcitation process of a semiconductor, described in the text, from [Otho 98].

carrier recombination time τ_{rec} [Jeps 96]. Than the density of free carriers is modified, what can be described by a carrier generation term $G(t)$:

$$\frac{dn_{free}}{dt} = -\frac{n_{free}}{\tau_{rec}} + G(t). \tag{3.2}$$

The carrier generation term $G(t)$ can be described by a δ-function for extreme short pulses or a Gauss-shaped pulse, if the laser pulse duration is not well below τ_{rec} of the investigated material.

The maximum density of carriers, which are optically induced by a laser pulse, can be estimated by:

$$\Delta n_{max} = \frac{P_{laser}\lambda\eta}{f_{laser}hcA\delta}, \tag{3.3}$$

where P_{laser} is the average laser power, λ is the light wavelength, η is the quantum efficiency, f_{laser} is the repetition frequency of the laser, A is the beam spot area and δ is the penetration depth. Assuming $P_{laser} = 1$ to 35 mW, $A = 5\times10^{-6} cm^2$, $\delta = 100$ nm, $f_{laser} = 80$ MHz, $\eta = 1$ which are realistic values for the described experiments, yields a maximum excited carrier density of $\Delta n_{max} = 1 \times 10^{18} cm^{-3}$ to $3.5 \times 10^{19} cm^{-3}$.

3.1.1 Carrier trapping

In a real semiconductor the free carrier distribution is dominated not by carriers, which are intrinsically excited from the valence band, but by electrons or holes which are introduced to the crystal lattice by natural or artificial dopants near the conduction band (donors) or the valence band (acceptors). LT-GaAs crystals exhibit a large density of As anticipates acting as donor centers, like described in a previous section (2.1.1), and these donor centers cause localized states in the energy gap. Carrier trapping due to such localized states can modify the carrier relaxation dynamics substantially. Othonos *et al.* have developed a rate equation formalism to model the carrier dynamics in LT-GaAs, which includes the influence of the midgap states [Otho 98]. Using this formalism experimental results of pump-and-probe transmission measurements, sensitive to a refractive index change could be explained very accurate. Fig. 3.2. shows a schematic band diagram and the excitation and relaxation processes, which are involved.

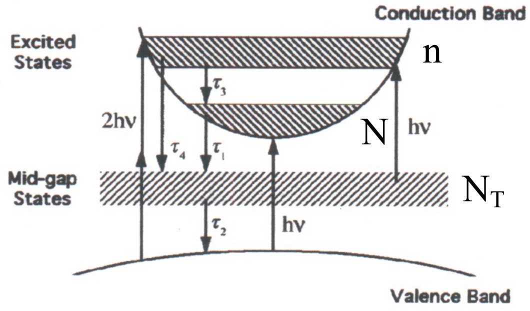

Fig. 3.2: Schematic picture of the energy band of LT-GaAs with trapping states and the corresponding relaxation times.

The localized states trap rapidly excited carriers and reduce the free carrier density very fast. In fig. 3.2. excitation from the valence to the conduction band by an one photon process and by a two photon process is indicated. From the localized states additional excitation can occur, which produces high energy carriers at energy states well above the gap.

Those high energy carriers are trapped very fast (τ_4). The carrier transition from the mid-gap states to the valence band is described by τ_2. The carrier trapping from the conduction band edge occurs on a time scale of τ_1 and the slow carrier relaxation by emission of optical phonons takes a time of τ_3. Values reported in literature depend sensitively on the growing conditions of the LT-GaAs. The main assumptions of the rate equation model by Othonos *et al.* are:

- The population of carriers N, at the bottom of the conduction band, contributes to absorption saturation.
- The whole population of excited carriers in the conduction band (N and n) contributes to the refractive index change.

- The trap-states population, N_T, contributes to the absorption, but not to the refractive index change.

Under these conditions the rate equations of the model are as follows:

$$\frac{dN}{dt} = \frac{\alpha I_0}{\hbar\omega} - \frac{N}{\tau_1} + \frac{n}{\tau_3}, \tag{3.4}$$

$$\frac{dN_T}{dt} = -\frac{\alpha_T I_0}{\hbar\omega} - \frac{N_T}{\tau_2} + \frac{N}{\tau_1} + \frac{n}{\tau_4} \tag{3.5}$$

and

$$\frac{dn}{dt} = -\frac{\alpha_T I_0}{\hbar\omega} + \frac{I_0^2\beta}{\hbar\omega} - \frac{n}{\tau_3} - \frac{n}{\tau_4}, \tag{3.6}$$

where I_0 is the laser intensity, α is the band-to-band absorption coefficient, α_T is the absorption coefficient from the traps to excited states in the conduction band, and β is the two-photon absorption coefficient. After photoexcitation of electrons to the bottom of the conduction band (N) some carriers can be trapped in the mid-gap states (N_T), from where they can be excited again to high energy states in the conduction band (n). This process gives rise to an additional absorption mechanism in LT-GaAs and can lead to a much larger carrier concentration in the conduction band compared to pure band-to-band absorption. These equations (3.4. - 3.6.) determine not only the refractive index and absorption change but (together with the mobility of the carriers) basically the temporal evolution of a carrier polarization inside the investigated sample under a bias field. This polarization leads to a screening of an applied bias field, which is measured in the PPT experiment. In the next sections the connection between the measured signal and the free carrier density $n_{free} = n + N$ will be explained. By fitting these and the following equations to the experimental results, the carrier trapping time and carrier relaxation time can be estimated, based on the rate equation model by Othonos *et al.*.

3.1.2 Photoconductivity

In the previous section carrier excitation without an external bias field is described. In the PPT experiment a transient photocurrent driven by an external bias field is observed and therefore the influence of this bias field has to be taken into account. The bias field accelerates the free carriers and leads to an ultrashort current pulse, the photocurrent. The current modulation depends on the change of the conductivity σ of the excited area. Optical illumination of a semiconductor with photons of energies larger than the energy gap $E_{ph} = h\nu \geq E_g$ leads to an increase in the carrier number and therefore likewise in σ compared to the dark conductivity. This effect is called *photoconductivity.* In general σ depends on the free carrier density of electrons and holes and their mobility, like described by the following equation:

$$\sigma(T) = |e|(\mu_e n_e(T) + \mu_h n_h(T)), \tag{3.7}$$

where $\mu_{e,h}$ are the carrier mobilities and $n_{e,h}$ the carrier densities, respectively. A change in σ can either be caused by a change in the free carrier number (described in the previous section) or the carrier mobility or both. Therefore in the experiments to the carrier dynamics of GaAs the effects of carrier excitation and carrier mobility changes has to be taken into account. The electron and hole mobilities indicated earlier in table 2.1 are values at the thermal equilibrium of GaAs. Instantly after an excitation due to an optical pulse the high energy electrons change their mobility beginning from an initial mobility μ_i back to the equilibrium value μ_{eq}, described by an exponential law with the average scattering time τ_s:

$$\mu(t) = \mu_{eq} - (\mu_{eq} - \mu_i)e^{-t/\tau_s} \tag{3.8}$$

In the case of GaAs $\mu_{eq} = 8800\ cm^2(Vs)^{-1}$ and $\mu_i = 1400\ cm^2(Vs)^{-1}$ for 1.5 eV excitation and $\mu_i = 300\ cm^2(VS)^{-1}$ for a 2 eV excitation [Beni 94].

3.1.3 Carrier polarization

In the PPT experiment the carriers are optical injected into a high resistive gap of the LT-GaAs between two charged electrodes. The stored energy of this capacitance is now transformed to kinetic energy of the free carriers (electrons and holes) and the motion of the carriers leads to a polarization and a screening of the applied bias voltage due to a *space-charge* field. The local electrical field in the illuminated area is reduced. If the external voltage is screened completely, the carrier motion becomes randomly distributed because of carrier-carrier scattering and the photocurrent vanishes. The observed PPT signal (the experiment is described in detail in the next chapter) depends on the local electrical field and gives therefore information about the temporal evolution of the polarization which includes mainly the dynamics of the electrons. In LT-GaAs the mobility of holes is much lower than that of the electrons and the contribution of the holes can therefore be neglected. The temporal resolved evolution of the PPT signal is governed by the mentioned space-charge field, which is proportional to the average distance and density of the electrons-hole pairs separated in the bias field, see fig. 3.3. The local field $\vec{E}_{loc}$ results from the biased field $\vec{E}_{bias}$ and this space-charge field $\vec{E}_{sc}$:

$$\vec{E}_{loc} = \vec{E}_{bias} + \vec{E}_{sc} = \vec{E}_{bias} - \frac{\vec{P}_{sc}}{\eta\epsilon}, \tag{3.9}$$

where $\vec{P}_{sc}$ is the polarization, η is a geometrical factor and ϵ is the dielectric constant. The induced polarization changes with time, what can be described by [Bror 94]:

$$\frac{d\vec{P}_{sc}(t)}{dt} = -\frac{\vec{P}_{sc}(t)}{\tau_{rec}} + \vec{j}(t), \tag{3.10}$$

where τ_{rec} is the carrier lifetime, which is in LT-GaAs determined by the fast carrier trapping, and $\vec{j}(t)$ is the photocurrent. The bias field accelerates the optical induced carriers until they reach the saturation velocity $\vec{v}_s$. Some authors have previously used the *Drude-Lorentz model* to describe the carrier dynamics without screening effects [Beni 93]

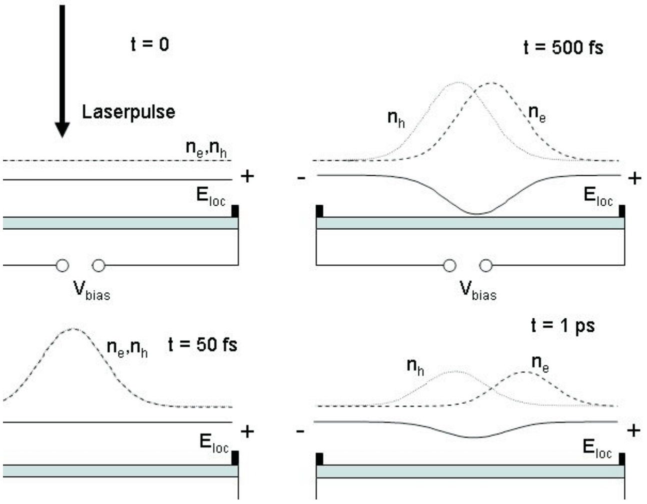

Fig. 3.3: Schematic diagram of the temporal development of the free carrier densities and the local electrical field after femtosecond excitation.

and with screening included [Jeps 96]. The current density in the antenna is related to the free carrier density n_{free} and velocity $\vec{v}$ by the equation:

$$\vec{j} = -en_{free}\vec{v}. \tag{3.11}$$

Because of the 10 times lower mobility of the holes, the small contribution to the current resulting from hole motion is neglected. In the *Drude-model* the motion of electrons in a local electrical field $\vec{E}_{loc}$ is slowed down by scattering:

$$\frac{d\vec{v}(t)}{dt} = -\frac{\vec{v}}{\tau_{rel}} + \frac{e}{m^*}\vec{E}_{loc}. \tag{3.12}$$

Here τ_{rel} is the carrier momentum relaxation time. Introducing the equations (3.10 - 3.11) and taking the time derivative, a second order differential equation is obtained:

$$\frac{d^2\vec{v}}{dt^2} = -\frac{1}{\tau_{rel}}\frac{d\vec{v}}{dt} - \frac{\omega_{pl}^2\vec{v}}{\eta} + \frac{e\vec{P}_{sc}}{m^*\eta\epsilon\tau_{rec}}, \tag{3.13}$$

with the plasma frequency $\omega_{pl}^2 = ne^2/m^*\epsilon$ and τ_{rec} from equation (3.2). The *Drude-model* is only applicable if the approximation of a *free electron gas* is valid. This is the case for a large number of excited electrons. Solving these equations gives the information of the carrier dynamics via the parameter τ_{rel} and τ_{rec} necessary to describe the results of the PPT experiment. This is the connection between the measured THz signal and the carrier dynamics. Fits of this theory to the experimental results of the PPT technique are summarized in chapter 6.

3.2 Carrier Transport in YBCO

The carrier transport of YBCO is very anisotropic, which influences all electrical and optical properties, as mentioned in chapter 2. Therefore the resistivity ρ is a tensor for YBCO in the normal state. The temperature dependence of ρ_{ab} (along the planes) of high quality thin films of YBCO with optimum oxygen doping shows a linear behavior well above T_C (dc resistivity). Flik *et al.* supposed to extrapolate the normal state resistivity of YBCO to temperatures below T_C by using Matthiessens rule to provide a hypothetical electrical resistivity below T_C as if the material were in the normal state [Flik 92], [Zima 60]. Here ρ_d is a residual resistance due to crystal imperfections, which is independent of temperature, and $\rho_s(T)$ is the electrical resistivity from scattering by phonons:

$$\rho(T)_{ab} = \rho_d + \rho_s(T). \tag{3.14}$$

In a normal metal ρ_s can be described by the *Bloch-Grüneisen*-equation [Zima 60]:

$$\rho_s(T) = 4\rho_\Theta \left[\frac{T}{\Theta}\right]^5 \int_0^{\Theta/T} \frac{x^5 e^x}{(e^x - 1)^2} dx, \tag{3.15}$$

where Θ is the Debye temperature and ρ_Θ is a constant. From specific heat measurements Θ of YBCO was determined by Flik *et al.* [Flik 92] to be 470 K. From the electrical dc resistivity in the normal state the electron scattering rate $\Gamma = 1/\tau$ can be (in the simpliest case of isotrop material with quasi-free carriers) approximatly calculated by:

$$\frac{1}{\tau} = \rho \frac{ne^2}{m^*} \tag{3.16}$$

where m* is the effective electron mass and n the electron number density, which can be found in literature: $m^* \approx 4.3 \times 10^{-30} kg$ and $n \approx 4 \times 10^{27} m^{-3}$ [Fior 90]. The scattering rate is therefore also a tensor.

In a parabolic band approximation of quasi-free electrons with constant effective mass m* and with kT<< E_F the dc conductivity as ratio of the current density to the electric field is:

$$\sigma_{dc} \simeq \frac{e^2 \tau(E_F) n}{m^*}, \tag{3.17}$$

with n is the free electron concentration and $\tau(E_F)$ is the relaxation time at the Fermi energy. Perfect conductivity can be described by $\tau(E_F) = \infty$. When an electrical field $E = E_0 e^{-i\omega t}$ accelerates the conduction electrons, they undergo random collisions, which interrupt their regular oscillations. The most simple model to describe this process is the *Drude-model*, which accounts for the collisions by adding a friction term to the equation of motion of the electrons. Therefore the free-carrier conductivity σ_n can be expressed as a function of the frequency of the applied field and the dc conductivity by:

$$\sigma_n(\omega) = \frac{\sigma_{dc}}{1 - i\omega\tau_D}, \tag{3.18}$$

where τ_D is the average time between the collisions and σ_{dc} is the dc conductivity given above in equation (3.17). At temperatures above T_C the *Drude-model* generally describes the frequency dependence of YBCO up to the THz region well [Bror 96].

Below T$_C$ an electromagnetic field $E = E_0 e^{-i\omega t}$ interacts with the thermally excited quasiparticles and the correlated super-carriers (Cooper pairs) which are condensed in the same coherent quantum state following to BCS theory. In the case of an ac current flow the superconductor always shows dissipation and a part of the current will be carried by thermally excited quasiparticles.

The conductivity of a superconductor is determined by the partition of the current transport between the types of charge carriers and the scattering mechanisms of the quasiparticles, which are dependent on frequency of the electric field and the temperature, the number of impurities, grain boundaries and defects, etc. The response of superconductors to alternating electromagnetic field below T$_C$ is often described by the *two-fluid-model.* This model separates the response into two independent "superconducting" and "normal fluid" reactions to the applied field. It is only valid for frequencies below the energy-gap frequency, since above this frequency additional losses (Cooper pair breaking) leads to a dissipation approaching that of the normal state.

The conductivity σ can be estimated by using the relative normal carrier fraction: $f_n = 1 - f_s = \mathrm{n}_n(T)/N$ and the supercarrier fraction: $f_s = \mathrm{n}_s(T)/N$ of the whole carrier number N, which are assumed to be independent from each other:

$$\sigma(\omega) = f_s\sigma_s(\omega) + (1 - f_s)\sigma_n(\omega). \tag{3.19}$$

Here f_n and σ_n are the fraction and conductivity of the residual normal electrons and σ_s is the conductivity of the BCS-like electrons, i.e. Cooper pairs and quasiparticle whose behavior can be described by BCS theory. The complex conductivity σ_s of the BCS electrons can be calculated by an algorithm of Zimmermann *et al.* [Zimm 91], the factor $(1 - f_n)$ in this model is proportional to $[1 - (T/T_C)^4]$ [Gort 34] below T$_C$ and σ_n is calculated from a temperature and frequency dependent scattering rate Γ. Following the *two-fluid-model* the conductivity can be written as follows:

$$\sigma(\omega, T) = \frac{\sigma_{dc}}{(1 - i\omega\tau_D(T))} f_n(T) + \frac{i}{\mu_0\lambda_L^2(0)}(1/\omega - i\pi\delta(\omega))f_s(T). \tag{3.20}$$

The first term describes the normal component (Drude-term) and the second term the inductive behavior of the supercarriers (London-term). From fits of equation (3.20) to THz TDS measurements σ_{dc}=3000 S/cm, $\tau_D = 1 \times 10^{-13}$s and the London penetration depth λ_L=150 nm in the case of YBCO at T = 0 K were deduced [Wilk 00], [Bror 96]. To satisfy the Kramers-Kronig relations and causality the δ-function at zero temperature has to be added in the superconducting term without experimental evidance at THz frequencies. It has to be taken care that the *two-fluid-model* assumes a *local* carrier response to the applied field:

$$\vec{E}(\vec{r}) = \vec{j}(\vec{r}), \tag{3.21}$$

where the current density at the point $\vec{r}$ is determined by the electrical field at that point $\vec{E}(\vec{r})$. In the case of YBCO at THz frequencies this is appropriate, since the coherence length is about 1 nm much smaller than the wavelength in the THz frequancy region.

3.2.1 Influence of the d-wave Symmetry

The possibility of an energy gap $\Delta(T)$ which is not isotropic in k-space is of great contemporary interest. In the case of cuprate superconductors some theories propose a carrier coupling which is mediated by the exchange of spin fluctuations, which predicts also an d-wave symmetry of the order parameter [Levi 93]. A consequence of the d-wave pairing is that the spectrum of the excited states reaches down to zero energy and the temperature dependence of the normal carrier fraction $f_n(T)$ and the London penetration depth will not follow the BCS theory, but rather a power law:

$$f_n(T) \simeq \left(\frac{T}{T_C}\right)^{\alpha} \tag{3.22}$$

and

$$(\lambda_L)^{-1} \simeq \sqrt{1 - \left(\frac{T}{T_C}\right)^{\alpha}}. \tag{3.23}$$

For T near T$_C$, the weak coupling limit and s-wave pairing [Mühl 59] BCS-theory predicts $\alpha = 1$. Some experiments at YBCO near T$_C$ [Anla 89], [Lee 95] have indicated a different temperature dependence following more close to the *two-fluid* model of Gorter and Casimir [Gort 34] with $\alpha = 4$. Other groups reported a quadratic temperature dependence of λ_L with $\alpha = 2$ for YBCO at temperatures above $T > 0.5 \times T_C$ [Ilic 96], [Lee 93]. This result is supported by microwave-, muon spin rotation-, and low field magnetization measurements [Bonn 92].
The *two-fluid-model*, despite its common practical usage, fails to explain some experimental results: e.g. the observed frequency dependence of the surface resistance at THz frequencies. Therefore more recent theories take mechanisms into account, which are neglected by the *two-fluid-model*: e.g. the residual losses at grain boundaries, the phase slip processes, and the d-wave symmetry of the order parameter. The temperature dependence of the surface resistance of YBCO thin films at THz frequencies can be qualitatively described by a *weak coupling model* of d-wave superconductivity [Wilk 00]. Hensen *et al.* used in this model the predicted symmetry of the order parameter $\Phi = \Delta_0 cos 2\phi$ to explain microwave losses at f = 0.087 THz [Hens 97]. The carrier scattering in this model is described by: a) an elastic scattering rate Γ_N^{el} resulting from the density of point defects n$_{imp}$ which are scatter centers on the density of states N(0) at the Fermi level:

$$\Gamma_N^{el} = \frac{n_{imp}}{\pi N(0)} sin^2 \delta_N. \tag{3.24}$$

and b) an inelastic phenomenological scattering rate Γ^{inel} with a temperature dependence:

$$\Gamma^{inel}(T) = \Gamma^{inel}(T_C)[at^3 + (1-a)e^{b_1(t-1)[1+b_2(t-1)^2]}], \tag{3.25}$$

with t as the reduced temperature, δ_N as a scattering phase shift and a ,$b_{1,2}$ as fitting constants [Hens 97]. The temperature dependence of equation (3.25) is similar to the temperature dependence of inelastic scattering caused by Spin-fluctuation exchange within the *nested-Fermi-liquid* model [Ruva 96]. Additional losses can be induced by grain boundaries in the film, which cause an temperature independent residual resistance. Reported fit parameters of the described model to measured data of the THz surface resistance are: $\Gamma_N^{el} = 1.2$ meV, $\Gamma^{inel}(T_C) = 35.8$ meV, a = 0.11, b$_1$ = 15, b$_2$ = 1 [Wilk 00].

3.2.2 Electron-Phonon Coupling

The time resolved PPT experiment allows the direct observation of the quasiparticle relaxation time. The quasiparticle scattering rate is a basic parameter to describe thermal and electrical transport properties and the optical behavior of materials. It has to taken into account that for geometries which are smaller then the electron mean free path (e.g. thin films), the electron scattering is increased by boundary scattering. The scattering of quasiparticles with LO phonons is assumed to give the main contribution to the relaxation after an optical excitation. Therefore the measured decay times of the PPT signal are connected to the electron-phonon coupling. For a theoretical description of the relaxation process the relationship of the scatter rate and the electron-phonon coupling constant is needed. This coupling constant is important at different theories, which try to describe the superconducting state by phonon mediated electron-electron interaction, e.g. the Eliashberg theory.
Allen *et al.* compared the experimental results of the temperature dependence of the conductivity with band-structure calculations and supposed that the main contribution to the transport current relaxation comes from the scattering of electrons by phonons [Alle 88]. Here the conductivity tensor is expressed in the isotropic relaxation time approximation:

$$\sigma_{\alpha\beta} = \frac{\tau(\Omega_p^2)_{\alpha\beta}}{4\pi}, \tag{3.26}$$

with the plasma frequency tensor:

$$(\Omega_p^2)_{\alpha\beta} = \frac{4\pi e^2}{V_0} \sum_k v_{k\alpha} v_{k\beta} \delta(\epsilon_k) = 4\pi e^2 N(0) \langle v_\alpha v_\beta \rangle. \tag{3.27}$$

Where V_0 is the volume of the primitive cell, N(0) is the density of states at the Fermi energy per atom and $v_{k\alpha}$ is the group velocity of the quasiparticles with spectrum ϵ_k. The possible anisotropy of the transport coefficient is determined by the anisoptropy of the Fermi surface [Plak 95]. In these calculations the transport relaxation time at high temperatures is estimated by:

$$\frac{\hbar}{\tau_{tr}} = 2\pi\lambda_{tr} kT (1 - \frac{\hbar^2 \langle \omega^2 \rangle}{12(kT)9^2} + ...), \tag{3.28}$$

where λ_{tr} is the electron-phonon coupling constant and determined by the function $\alpha_{tr}^2 F(\omega)$ with the matrix element of the electron-phonon interaction α_{tr} and the phonon density of states $F(\omega)$. α_{tr} determines the relaxation of quasiparticle momentum. However this theoretical model gives values of $\lambda_{tr} = 0.32$ and $\rho_{ab} = 37 \mu\Omega cm$ for YBCO at T = 300 K, which are several times less than the experimental data. This could be caused by: 1) higher values of λ_{tr}, 2) smaller Ω_p or 3) additional scattering mechanisms. The existence of antoferromagnetic spin fluctuations provides a strong scattering of carriers and could be responsible for the measured higher values of the resistivity [Ihle 91]. Experiments which sheed light on the different quasiparticle scattering processes in YBCO are therefore usefull to result in a progress in the theory of superconductivity. Kamaras *et al.* performed infrared spectroscopy studies on YBCO thin films and used the *Drude model* to explain the results above T_C [Kama 90]. Electron motion in the *ab* plane of YBCO above T$_C$ resembles that in a normal metal [Flik 92]. Orenstein *et al.* [Oren 90] discussed the residual scattering rate of YBCO crystals due to impurity and defect scattering and the temperature dependent scattering rate due to electron-phonon-interactions. Miller *et al.* fitted the microwave absorption of epitaxial YBCO with a *two-fluid* model and obtained an average scattering rate of 400 cm^{-1} at T = 2 K [Mill 91]. Using infrared spectroscopy Flik *et al.* determined the scattering rate Γ in the normal and superconducting state of YBCO films [Flik 92]. In the normal state the scattering rate is usually calculated by means of the *Drude model* and below T$_C$ an algorithm developed by Zimmerman was established to fit the spectroscopy data by a frequency-dependent conductivity with arbitrary purity [Zimm 91]. Zimmermann used as parameters the reduced temperature t, the dc conductivity σ_{dc} and the normalized scattering rate Y:

$$Y = \frac{h}{4\pi\tau\Delta}. \tag{3.29}$$

At zero temperature this equation becomes: Y=$(\pi/2) \cdot (\xi/l)$, where ξ is the coherence length and l is the electron mean free path.
A more general expression of the quasiparticle scattering rate in the phenomenological marginal Fermi liquid theory is given by [Bror 96]:

$$1/\tau \simeq g^2 N(0) max(\hbar\omega, kT), \tag{3.30}$$

where g is a coupling constant. This model describes properly the normal resistivity, the anomalous coherence peak in the conductivity at low temperatures, the voltage dependence of the tunneling conductance, results of THz TDS and the temperature dependence of the NMR relaxation rate of cuprate superconductors.

3.2.3 Kinetics of Quasiparticle Recombination

The quasiparticle-to-Cooper pair recombination in superconductors was first discussed by Rothwarf and Taylor [Roth 67] in terms of two rate equations for the excess quasiparticles and the phonons released in the recombination process. Theoretically the nonequilibrium distributions of phonons and quasiparticles can be bescribed by a system of such time-dependent coupled kinetic equations [Chan 77]. The Rothwarf-Taylor (RT-) equations are nonlinear differential equations and describe the deviations of the system from the equilibrium as the interplay between quasipartilces and phonons with energies greater 2Δ:

$$\frac{dn_{qp}}{dt} = -Rn_{qp}^2 + 2\frac{n_{ph}}{\tau_{break}} \tag{3.31}$$

and

$$\frac{dn_{ph}}{dt} = \frac{Rn_{qp}^2}{2} - \frac{n_{ph}}{\tau_{break}} - \frac{n_{ph}}{\tau_\gamma}, \tag{3.32}$$

where n$_{qp}$ and n$_{ph}$ are the numbers of quasiparticles and phonons with energy exceeding the energy gap 2Δ. R is the quasiparticle recombination rate constant, τ_{break} is the Cooper pair breaking time and τ_γ is the phonon decay time.

Han [Han 90] used the RT-equations to explain the delay of the maximum change in the reflectivity after the end of the optical excitaton. Jaekel *et al.* assumed that in the case of YBCO the excited quasiparticles are resulting mostly from broken Cooper pairs: $\Delta n_{qp} \simeq n_{CP}$.

If the PPT signal S is asssumed to depend linearly on the transmittivity of the superconductor, the change of the signal ΔS is therefore connected to the number of broken pairs like:

$$\frac{\Delta S}{S_0}(T,t) = \frac{1}{S_0} \cdot \frac{\partial S}{\partial n_{CP}} \Delta n_{CP}(T,t), \tag{3.33}$$

and therefore the maximum in the PPT signal change is connected to the maximum number of excited quasiparticles. After the optical Cooper pair breaking is finished, high energy phonons and quasiparticles continue to break supercarriers and a cascade effect due to high energy quasiparticles occurs [Han 90]. The RT-equations are valied for T << T$_C$ ([Roth 67]), where the quasiparticle energies are much smaller than the energy gap Δ. In this case all quasiparticle can be considered to have the same energy and their total number is an appropriate parameter. Using the RT-equations Jaekel *et al.* calculated $\tau_{break} \simeq 60$ fs for the initial Cooper pair breaking time at T = 0 K and a recombination time $\tau_{r,0} \simeq$1.5 ps with the following temperature dependence:

$$\tau_r = \tau_{r,0} + 1.15 \cdot \tau_{e-ph} \frac{T}{T_C} \cdot \frac{1}{\sqrt{1 - \frac{T}{T_C}}} \tag{3.34}$$

where $\tau_{e-ph} = 385$ fs is a characteristic scattering time derived from the BCS theory [Kadi 86]. Kabanov *et al.* developed a model to describe the temperature dependence of the photoinduced quasiparticle population and the relaxation times [Kaba 99]. They obtained for the phonon decay time:

$$\frac{1}{\tau_\gamma} = \frac{12\Gamma_\omega k_B T \Delta(T)}{\hbar\omega^2}, \tag{3.35}$$

where Γ_ω is the Raman-phonon linewidth, which is an experimental parameter and measured to be $\Gamma_\omega = 13$ cm^{-1} for the A$_{1g}$-symmetry apical O(4) phonon mode and ω the phonon frequency, which can be approximated by $\omega \simeq 400$ cm^{-1} in the case of YBCO [Miha 93]. The temperature dependence of the phonon decay time shows therefore a divergence at T$_C$: $\tau_\gamma \simeq 1/\Delta(T)$. This behavior is observed in optimally doped cuprates [Han 90], [Easl 90].

Near T → T$_C$ the energy spectrum of quasiparticles cannot be neglected and an *effective temperature* is introduced as a parameter to describe the quasiparticle energy distribution. The usage of different effective temperatures to characterize the nonequilibrium distributions of electrons and phonons proofed to be a good approximation for the carrier dynamics of superconductors [Perr 83], [Gers 84], [Alle 87]. The model supposes a very fast quasiparticle thermalization at high energies via electron-electron interaction and electron scattering by optical phonons [Reiz 89], [Bluz 91], [Gers 89]. In the *two temperature model* (2T-model) [Seme 95] two different temperatures T$_e$ and T$_{ph}$ are assigned to the quasiparticle and phonon nonequilibrium distributions, respectively. The temporal evolutions of both temperatures are connected to the changes in the energy spectra of the electrons and of the phonons.

When a short optical pulse is applied to a superconductor the energy balance of the whole electron-phonon system is governed by a pair of nonlinear coupled differential equations [Anis 75]:

$$C_e \frac{dT_e}{dt} = +\kappa_e \nabla^2 T_e - g_{e-ph}(T_e - T_{ph}) - g_{e-v}\Delta T_e(t) + P(\vec{r}, t) \tag{3.36}$$

and

$$C_{ph} \frac{dT_e}{dt} = +\kappa_{ph} \nabla^2 T_{ph} + g_{e-ph}(T_e - T_{ph}) - g_{ph-v}\Delta T_{ph}(t) + P_d(t), \tag{3.37}$$

where g_{e-ph} is the electron-phonon coupling constant, g_{e-v} is the electron-vortex interaction constant, g_{ph-v} is the phonon-vortex interaction constant, $C_{e,ph}$ is the electron/phonon specific heat, $\kappa_{e,ph}$ is the electron/phonon heat conductivity, P is the laser fluence and P_d the dissipated energy. The first term reflects the diffusion process, the second term the electron-phonon interaction, the third term reflects the interaction with high energy electrons (equation (3.36)) and phonons (equation (3.37)).
Using standard scattering rate equations ([Zima 60]), Allen ([Alle 87]) was able to relate the relaxation rate of the electron temperature T_e to the electron-phonon coupling constant λ_{e-ph} used in the Eliashberg generalization of the BCS theory [McMi 68] as:

$$T_e \frac{\partial T_e}{\partial t} \simeq -\frac{3\hbar}{\pi k_B} \lambda_{e_ph} \langle \omega^2 \rangle (T_e - T_{ph}) \tag{3.38}$$

here $\langle \omega^2 \rangle$ is the second moment of the phonon spectrum defined by McMillan. Equation (3.38) assumes that the energy deposited in the sample by the laser pulse is distributed uniformly, so that effects of heat transport (the κ_e term) can be neglected. The coupling constants g_{e-ph} and λ_{e-ph} are connected by:

$$g_{e-ph} = \frac{3\hbar\gamma\lambda_{e-ph}\langle \omega^2 \rangle}{\pi k_B}, \tag{3.39}$$

where γ is the normal-state electronic specific heat constant (or Sommerfeld constant). A superconducting film is now considered to carry a constant current and driven in the resistive state at the temperature T near T_C. At this condition the energy gap is small compared to k_BT and the quasiparticle energy spectrum is close to that of electrons in the normal state. Consequently the ineleastic scattering of quasiparticles as well as their recombination into Cooper pairs can be described by the electron-phonon interaction time [Kapl 76]. Joule heating by the bias current is neglected and only small deviations from equilibrium are considered. This enables to use a linearized form of the equation (3.36) [Lind 99]:

$$C_e \frac{dT_e}{dt} = \frac{\alpha P(t)}{V} - \frac{C_e}{\tau_{e-ph}}(T_e - T_{ph}) \tag{3.40}$$

and

$$C_{ph} \frac{dT_{ph}}{dt} = \frac{C_{ph}}{\tau_{ph-e}}(T_e - T_{ph}) - \frac{C_{ph}}{\tau_\gamma}(T_{ph} - T_s), \tag{3.41}$$

α as the absorption coefficient, V as the volume of the bridge under illumination, τ_{e-ph} as the electron-phonon scattering time, τ_γ as the phonon escape time into the substrate, τ_{ph-e} as the phonon-electron scattering time, and T$_s$ as the sample temperature. This analysis bases on the assumption, that for the resistive state of a film the characteristic time of the resistance is shorter or equal to the relaxation time of the nonequilibrium quasiparticle distribution. Accordingly the response time of the film in the resistive state should be the quasiparticle relaxation time.

3.2.4 Vortice Dynamics

YBCO is a superconductor of type *II*. Therefore flux pinning is necessary for a dc current transport without dissipation below T$_C$. Because of the relatively small pinning energies compared to the large superconducting temperature range [Yesh 88], it has been suggested that the critical currents in cuprate superconductors are limited by *flux-creep* described by the *Anderson-Kim model* [Ande 62], [Kim 64] at temperatures far below T$_C$. If the critical current is limited by *flux-creep*, the average critical current density $\mid \vec{j}_c(\vec{B},t) \mid = I_c/wd$ (with the reduced temperature $t = T/T_C$) can be calculated following Tinkham [Tink 88]:

$$\vec{j}_c(\vec{B},t) = \vec{j}_c(\vec{B},0)(1-\alpha(\vec{B})t-\beta t^2) \tag{3.42}$$

for $t << 1$, where $\vec{B}$ is the magnetic flux density. The β-term describes the temperature dependence of the free-energy difference of pinned and unpinned vortices in the film ($U(\vec{B},t) \simeq U(\vec{B},0)(1-\beta t^2)$). The $\alpha(\vec{B})$-term characterizes the thermally activated *flux-creep* [Tink 88] and can be written as:

$$\alpha(\vec{B}) = \frac{k_B T_C}{U(\vec{B},0)} ln \left[\frac{a \mid \vec{B} \mid \Omega}{E_{min}} \right], \tag{3.43}$$

where a is the average hopping distance of the vortices, Ω is the attempt frequency of escape, E_{min} is the electric field criteria that defines j$_c$.

4 Experimental Methods

This chapter describes the PPT method, which bases on the possibility of the emission of subpicosecond pulses by the material under investigation, in detail.
On one side various materials which exhibit high resistivity and very short carrier lifetime are able to emit THz radiation, such as crystalline-distorted, impurity-dominated materials [Tono 02]. On the other side the wide range of different high-temperature cuprate superconductors (samples of reported THz emitting materials:YBCO [Hang 96], YPBCO [Wald 00], $Bi_2Sr_2CaCu_2O_{8+\delta}$ [Mura 01], $Tl_2Ba_2CaCu_2O_{8+\delta}$ [Tomi 02]) are suitable for the PPT method, because thin film devices for picosecond and subpicosecond electromagnetical pulse emission can be prepared. By using this technique different materials or samples of the same material, grown under different conditions (like temperature), or with different atomic substitutions can be compared. Using the PPT technique the carrier dynamics of a semiconducting material can be studied even under high fields up to 100 $kVcm^{-1}$ or of a superconductor under high bias current densities up to $10^6 Acm^{-2}$. Because of its importance the photoconductive dipole antenna, used as detector for the THz radiation, is explained in more detail.

4.1 Experimental Set-up

4.1.1 Femtosecond Laser System

The source of the 100 fs laser pulses is a commonly used mode-locked Ti:sapphire oscillator (Tsunami ©) of the company Spectra-Physics [Spec]. The Ti:sapphire oscillator is pumped by a cw-solid-state laser (Millenia ©) at a frequency of about 532 nm and 5 W. The maximum average output power on the fs-laser is $P_{laser} \approx 0.7\ W$. The emitted wavelength can be tuned in a range of 710 to 980 nm and is adjusted to about 800 nm ($E_{photon} = 1.55\ eV$) with a width of about 20 nm. The nominal repetition rate is 82 MHz, i.e. a repetition time of 12.5 ns between two laser pulses. The highest emitted energy per pulse is given by $E_{pulse} \approx 0.7W/80MHz = 8.7\ nJ$ and the maximum power $P_{max} \approx E_{pulse}/(\Delta t) = 87\ kW$. This leads to local maximum electrical field strength of the pulse of about:

$$|\vec{\mathcal{E}}_{max}| \approx \sqrt{\frac{2P_{max}}{\pi r^2 c\epsilon_0}} \tag{4.1}$$

$= 1.83\ \times 10^8\ V/m$.
In comparison to this value the "atomistic" field strength can be calculated approximately [Mesc 99]:

$$|\vec{\mathcal{E}}_{at}| = \frac{e}{4\pi\epsilon_0 a_0^2} \tag{4.2}$$

$= 10^{11} V/m$, where a_0 is the *Bohr radius*. Ofcourse the field strength of the ionization of atoms in solids depends on the detailed band structure, what can not be considered here. The magnetic field strength in vacuum can be estimated by: $|\vec{\mathcal{H}}_{max}| \approx |\vec{\mathcal{E}}_{max}|/(377\Omega) = 4.8 \times 10^5 A/m$ equal to a magnetic induction $|\vec{\mathcal{B}}_{max}| \approx 0.6T$. Near the sample the laser average power is reduced to about 1..100 mW by the reflection and transmission losses inside the optical system. Assuming a laser spot diameter size at the sample surface of about 10 μm, the laser fluence can be calculated to be about 16 $\mu J cm^{-2}$ per mW laser power.

4.1.2 The THz Emission Experiment

The detection of electromagnetic fields in the THz frequency range is complicated because of the lack of sensitive detectors. The time resolved THz spectroscopy setup, shown in fig. 4.1 enables the user to measure the signal shape and phase in the time domain directly and coherent with a resolution limited by the femtosecond laser pulse width. This technique is used in the experiments to measure the THz emission of photoswitches and HTSCs and it is described in detail in different publications [Aust 84], [Smit 88], [Hang 96], [Tono 96]. The 100 fs optical excitation pulse is generated by a Ti:sapphire oscillator with the properties described above. The laser beam is divided by a beam splitter in a 20/80 ratio into a *trigger* pulse for the detector (20 % beam) and into an *excitation* pulse, which produces the radiation of the YBCO or the LT-GaAs device, respectively. Both laser pulses are coherent to each other. The time delay between the pulses can be changed by the difference in the length of the optical pathes due to a retro-reflector on a translation stage with a accuracy of 1 μm, i.e. 2×3.3 fs = 6.6 fs. A typical waveform of the THz an observed pulse and its Fourier transformation is shown in fig. 4.2 and 4.3. The THz pulse is collimated to the dipole antenna by a hemispherical Si lens on the backside of the GaAs wafer on which the

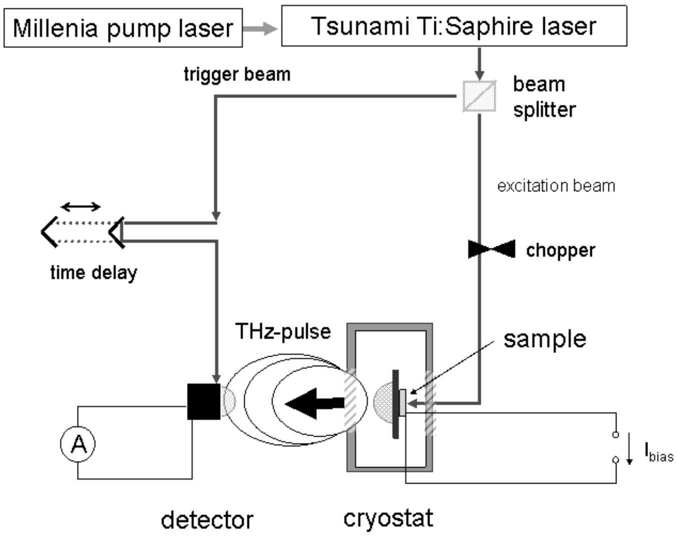

Fig. 4.1: The experimental set-up of the THz emission experiment.

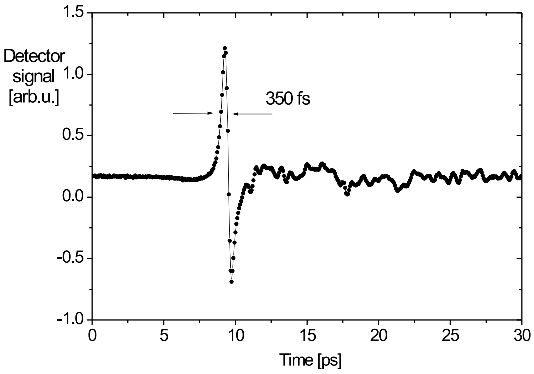

Fig. 4.2: The measured THz pulse shape of an LT-GaAs dipole antenna at T = 300 K, P_{laser} 10 mW and V_{bias} = 5 V in the time domain.

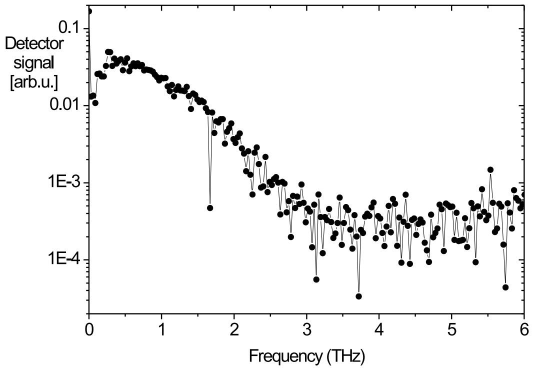

Fig. 4.3: The FFT of the THz pulse amplitude of fig. 4.2 in the frequency domain.

LT-GaAs layer is grown. The detector of the THz radiation is a photoconductive dipole antenna, described in detail in the next section, connected to a pre-amplifier (amplification factor: 10^5) to measure the THz field induced photocurrent. After the excitation due to the trigger pulse the photoconductive antenna is only a very short time sensitive to external electrical fields. The trigger laser beam is focused to the detector antenna due to an optical lens. The trigger average power is adjusted to about 10 mW and the focus size 10 μm, leading to an energy density of about $E_{laser} = 160\ \mu J cm^{-2}$.
For measurements with the superconducting devices at low temperatures down to 17 K an optical close-cycle He-cryostat is used for the sample cooling. Only below its critical temperature the HTSC can emit THz radiation. The cryostat windows are made of fused quartz with a high transmission coefficient in the visible and in the THz frequency range. For the LT-GaAs experiments the cryostat was not used, because it makes the allignment more complicated.
The spectral resolution of the system is about 10 GHz (equal to 0.3 cm^{-1}), which is defined by the maximum length of the optical path difference between trigger and excitation bream. To determine the value of the emitted THz radiation power a bolometer device can be used [Tani 94]. In our experiments the absolute THz power is not so important and for THz detection only photoswitches are used.

4.1.3 Auston Switches as Detectors

This section describes the properties of the LT-GaAs dipole antennas [Aust 84]. These photoconductive switches (Auston switches) detect the THz signals, emitted by the superconducting or the photoconductive emitters, respectively.
The LT-GaAs film, used in our experiments as photoconducting material with excellent properties, is a $2\mu m$ thick layer grown on a 0.5 mm thick GaAs wafer. The film is deposited by molecular beam epitaxy (MBE) at $250°C$ and post annealed at $600°C$ for 5 min [Tono 02]. An AuGe/Ni/Au layer on top of the LT-GaAs is patterned into a

coplanar transmission line geometry with a dipole structure and a gap in the middle. A schematic of the antenna as detector is shown in fig. 4.4 b). The dipole antennas are used for detection and emission of the THz radiation. The femtosecond trigger- (or gate-) laser pulse illuminates the area between the two electrodes. The sample is not biased by a external source if it works as detector.

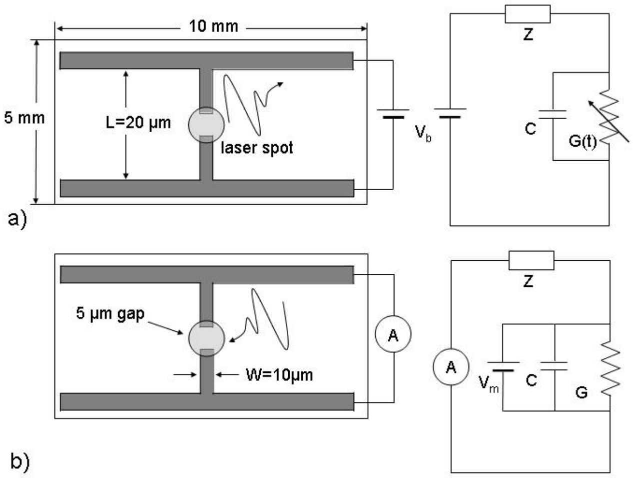

Fig. 4.4: Schematic picture of the GaAs antenna as a) THz emitter and b) THz detector.

The detection mechanism can be understand as follows: The laser beam generates free electrons above the energy gap in the conduction band of the GaAs. Therefore the photon energy has to be greater than the energy gap (1.43 eV). The injected, free charge carriers reduce the electrical resistivity of the material (GaAs exhibits a dark resistivity of $> 10^7 \Omega cm$) by many orders. The lifetime of the free charge carriers opens a time window during which the detector is sensitive to external electrical fields. That means if a electrical field is radiated to the dipole antenna at the moment during this window is open, this field accelerates the free electrons (and holes), produces a polarization and leads to a photocurrent [Jeps 96]. This photocurrent is in the order of some nA and usually a lock-in technique is used to measure it. This lock-in techique amplifies the small photocurrent and therefore the excitation signal must be modulated (in our experiment at 2 kHz (0.5 ms) due to an optical chopper). Because of the high repetition rate of the Ti:sapphire oscillator of 82 MHz a high amplification is realized (4×10^4). By changing the trigger time, compared to the exictation time of the emitting device, the whole temporal evolution of the applied electrical field can be measured. Because the amplitude and phase information is measured at every point in time this method is a coherent technique and non-coherent radiation (noise) is not observed. Therefore and because of the high repetition rate of the femtosecond laser the signal-to-noise ratio of this method is very high: 10000:1 and more. To calculate the exact strength $\vec{\mathcal{E}}_{THz}$ of the field from the measured photocurrent is difficult, because this current depends on the number of the excited carriers, which depend on the penetration depth δ, the quantum efficiency η, the laser focus area A and the mobility of the charge carriers. Furthermore the emitted THz field strength will be much higher than the field strength at the detector position, because of the absorption along the THz optics between emitter and detector. This is described in the next section.

An ideal detector would provide the correct shape of the measured pulse. Nevertheless because of the finite bandwidth and frequency dependent sensitivity of the detector a reshaping of the signal occurs. The modification of the measured THz signal is described by the so called *geometrical response function* (GFR) of the detector. The geometry of the detector (detection area) and the carrier dynamics of the detector material (carrier lifetime) influences this GFR. The detector measures a current flow induced by the average field over the detection area and not the local field. The focus size of the THz pulse is frequency dependent: smaller frequency components have a larger focus size. Therefore the area size will have an influence on the signal shape, which has to be estimated.

The detector area length L = 20 μm is the total length of the dipole (electrodes L_m plus gap length L_g). The width of the detection area is: W = 10 μm and the thickness of the LT-GaAs layer: T = 2 μm. Usual antenna theory fails to explain the antenna response, because the electric field amplitude varies substantially over the antenna area. The GFR is proportional to the current flow across the gap, which is determined by the voltage and the resistance R. The resistance is a serial combination of the two electrodes and the gap:

$$R = \frac{\rho_m L_m + \rho_g L_g}{TW} \approx \frac{\rho_g L_g}{T \cdot W}, \tag{4.3}$$

because the resistivity ρ_m of the electrodes is much smaller than the resisitivity of the gap ρ_g. The resistivity ρ_g depends on the photogenerated carrier density (equation 3.3). Approximating a homogeneous illumination over the whole LT-GaAs layer thickness and the antenna area it follows:

$$\rho_g = \frac{L_g W}{P_{laser} a}, \tag{4.4}$$

where a is a conversion factor between the laser power P_{laser} and the resistivity, which follows from equation 3.3:

$$a = \frac{|e| \mu_e \lambda \eta}{f_{laser} h c \delta}. \tag{4.5}$$

The hole contribution to the conductivity is neglected here. The average field strength $\vec{\mathcal{E}}$ produces the potential: $V = |\vec{\mathcal{E}}|L$ and this leads to a average current I (not the transient photocurrent):

$$I = \frac{V}{R} = \frac{|\vec{\mathcal{E}}|L \cdot P_{laser} a \cdot T}{L_g^2}. \tag{4.6}$$

The average electric field across the detection area L×W is given by [Jeps 96]:

$$|\vec{\mathcal{E}}| = \frac{1}{L \cdot W} \int_{-L/2}^{L/2} \int_{-W/2}^{W/2} \vec{\mathcal{E}}(x,y) dx dy = \frac{|\vec{\mathcal{E}}_{THz}| \pi w_{min}}{L \cdot W} \cdot Erf\left(\frac{L}{2w_{min}}\right) Erf\left(\frac{W}{2w_{min}}\right), \tag{4.7}$$

with the error function:

$$Erf(\chi) = \left(\frac{2}{\sqrt{\pi}}\right) \int_0^{\chi} e^{-u^2} du. \tag{4.8}$$

The maximum field strength $|\vec{\mathcal{E}}_{THz}|$ as function of the THz radiation power is given by the *Pointing theorem*:

$$|\vec{\mathcal{E}}_{THz}| = \frac{2}{w_{min}} \sqrt{\frac{P_{THz}}{\pi c \epsilon_0}}. \tag{4.9}$$

w_{min} is the waist of the focus of the THz field at the detector position. It depends on the wavelength like described by equation 4.19 in the next section. This leads to the following dependence of the average current I in the antenna on the THz signal power P_{THz} and the wavelength λ_{THz} in the case of $\lambda_{THz} >> L$ (this is valid in the case of our experiment, where $\lambda_{THz} = 300$ μm and L = 20 μm):

$$I = \frac{2 P_{laser} a T w_0 (n-1) L}{L_g^2 c R_l} \sqrt{\frac{P_{THz}}{\pi c \epsilon_0}} \frac{1}{\lambda_{THz}}. \tag{4.10}$$

Here w_0 is the waist of the THz pulse at the zero position. This GFR of the detecting device leads to a signal time differentiation at low frequencies. For very small antennas this approximation is valid even at several THz [Jeps 96], i.e. a signal very close to the differentiated original signal is detected. To obtain a large bandwidth and high signal a very small detector area is useful.
Finally in the detection process the THz field $|\mathcal{E}_{THz}(t)|$ is sampled by the time dependent conductivity $\sigma(t)$ of the photoconducting gap and the photocurrent j(t), which is the measured quantity, can be described by the equation:

$$j(t) = \frac{1}{t_{rep}} \int_0^{t_{rep}} |\vec{\mathcal{E}}_{THz}(t)| \sigma(t) dt, \tag{4.11}$$

where t_{rep} is the repetition time of the laser pulse (12.5 ns). If the carrier lifetime of the antenna material is sufficiently short and $\sigma(t)$ is nearly a delta function, the photocurrent directly represents the field of the THz pulse [Jeps 96].

4.1.4 THz Field Optics

The emitted THz power of the dipole antennas in the experiments, measured by a hot-electron bolometer, is very low: between 0.1 and 0.3 μ W at optimum excitation conditions [Tani 97b]. Therefore and because of the long wavelength λ_{THz} a *quasi-optical* system of two paraboloidal mirrors and two spherical lenses is used to focus the THz wave to the detector antenna for a better signal to noise ratio. Like mentioned earlier the bandwidth of the THz radiation is extremly wide and therefore the optical system has a critical influence on the THz pulse shape. Because the emitting device size is small compared to the emitted wavelength: $l \approx 25 \mu m < \lambda_{THz} \approx 300 \mu m$ (i.e. the emitter is a so called *small aperture antenna*, or a point source) the radiation of this antenna in the far-field (where $|\vec{r}| >> \lambda_{THz}$) can be described by a *dipole field.*

Oscillations of two charges q_+ and q_- with the distance: $z=z_0 e^{-i\omega t}$ produce the dipole moment:

$$\vec{d}(t) = d_0 e^{-i\omega t}\vec{e}_z, \tag{4.12}$$

where the charges are moving in z-direction. This changing dipole moment radiates a dipole wave into free space. If the wavelength is much larger than the charge distance, the idealized picture of the *Hertzian dipole*[1] can be used. In this case the electrical field amplitude can be written in spherical coordinates (r,θ,ϕ) [Mesc 99]:

$$\vec{E} = k^2|\vec{d}|sin\theta\frac{e^{-i(\omega t-kr)}}{r}\vec{e}_\theta. \tag{4.13}$$

$k = |\vec{k}| = \omega/c$ is the wave vector. Equation (4.13) describes a dipole field in a homogeneous medium, but in our experiment the antenna is situated at the surface of a dielectric. A part of the field directed toward the dielectric interface is reflected by *Fresnel's law* and a wide-angle interference occurs, leading to a radiation pattern inside the substrate which was calculated by Fattinger *et al.* [Fatt 89]. After emission by the superconducting (or photoconductive) antenna the electrical THz-field propagates through the substrate and is collimated by a spherical MgO lens on the backside of the substrate in the case of the superconducting antenna and a spherical Si lens for the LT-GaAs emitter. This lens were first used by Fattinger and Grischkowsky [Fatt 89]. The MgO material is highly transparent in the THz frequency range [Gris 90]. The index of refraction is nearly constant and matches to the index of the MgO substrate, but not to the index of the $LaAlO_3$ substrates, leading to resonance features in the frequency spectrum for these substrates. A further collimation of the THz beam is realized by a Si spherical lens, attached to the backside of the GaAs substrate of the detector. Highly crystalline silicon is transparent and dispersion free in the frequency range of interest. The lenses on detector and emitter side must be aligned carefully in axis with the center of the emitting antenna to obtain the full bandwidth of the pulse.
The radiation pattern emitted from a spherical lens-coupled THz system is modeled by Jepsen *et al.* [Jeps 96] in detail. Because the refractive index of the lens is higher than in air, there exist an angle of total internal reflection above which the electrical field will not coupled out of the lens. The size of this angle defines a circular aperture on the lens surface, which causes diffraction features in the radiation field. The diameter of the focus area of the MgO lens is estimated by 2 mm and for simplicity the THz pulse is assumed to be a *Gauss-shaped* pulse [Jac 00] (propagation in z-direction) in a paraxial *Fresnel*-approximation (the *Gouy phase* is neglected) [Mesc 99]:

$$E(z,\rho) \simeq \frac{A_0}{kq(z)}e^{i\frac{k\rho^2}{2q(z)}}e^{ikz}, \tag{4.14}$$

with q(z) as a complex number, which can be expressed as:

---

[1] The *Hertzian dipole* has no spatial dimension, but a non zero dipole moment.

$$\frac{1}{q(z)} = \frac{z + iz_0}{z^2 + z_0^2} = \frac{1}{R(z)} + i\frac{2}{kw^2(z)}, \tag{4.15}$$

where $R(z)$ is the wave front radius and $w(z)$ is the radiation waist. The radiation waist allows an estimation about the possible focus size, which can be reached in dependence on the wavelength λ_{THz} in free space. The pulse waist perpendicular to the propagation direction increases with distance z like:

$$w^2(z) = w_0^2 \left(1 + \left(\frac{z\lambda_{THz}}{\pi w_0^2}\right)^2\right), \tag{4.16}$$

where w_0 is the waist in zero position. Following equation (4.16) the waist radius is dependent on λ_{THz} and it is more complicated to focus the low frequency components, which have a larger waist $w(z)$.

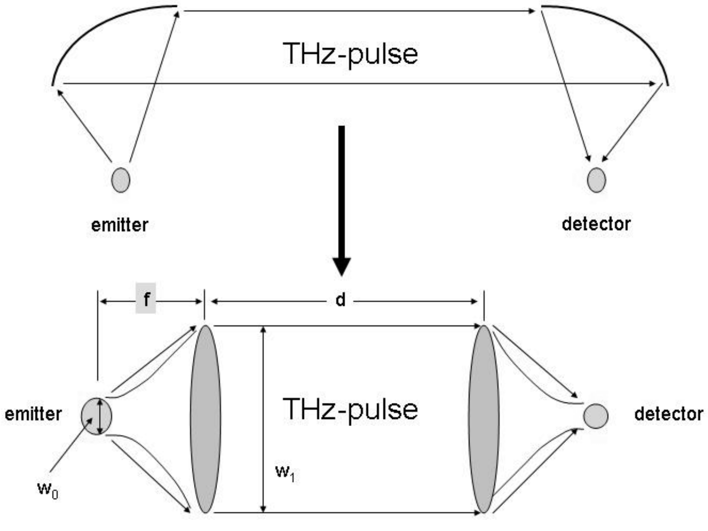

Fig. 4.5: The quasi-optical THz collimation system of 2 paraboloidal mirrors, which can be approximated by 2 lenses [Mesc 99].

The whole THz quasi-optical system consits of two spherical lenses, mentioned above, and two parabolodial mirrors between them. In the experimental set-up the emitting and detecting antennas are situated in the focus point of the paraboloidal mirrors, therefore the distance between the devices and the parabolodial mirrors is the focus length f, respectively. The distance between the two parabolodial mirrors is $d = Af$, where A is a constant. The parabolodial mirrors can be modeled by two thin lenses (fig. 4.5) and the propagation matrix M of the whole optical system can be calculated by the *ABCD-matrix theory* [Mesc 99] like [Jeps 96]:

$$M = \begin{pmatrix} \frac{fz_f(n-1)+R_l z_f(A-2)}{R_l n} & -\frac{z_f}{n} \\ \frac{f(n-1)+R_l z_f(A-2)}{R_l n f} & -\frac{1}{n} \end{pmatrix},$$

where z_f is the distance the beam travels into the lens which is fixed at the detector, n is the refractive index of the lenses and R_l is the radius of the lenses, assumed to be equal for both lenses because of simplicity. In the simpliest case of $A = 2$ the waist of the beam as function of the distance z_f can be written as [Jeps 96]:

$$w(z_f) = \frac{1}{n\pi w_0 R_l}\sqrt{[z_f(1-n)+nR_l]^2\pi^2 w_0^4 + z_0^2 R_l^2 \lambda_{THz}^2}. \tag{4.17}$$

The smallest focus size is given by the condition:

$$\frac{\partial w(z_f)}{\partial z_f} \doteq 0 \tag{4.18}$$

This results in a frequency-dependent focus size at the detector [Jeps 96]:

$$w_{min} = \frac{\lambda_{THz} R_l}{\pi w_0 \sqrt{(n-1)^2 + \left(\frac{R_l \lambda_{THz}}{\pi w_0^2}\right)^2}}. \tag{4.19}$$

For wavelength λ_{THz} smaller than w_0 this focus size can be approximated by:

$$w_{min} = \frac{\lambda_{THz} R_l}{\pi w_0 (n-1)}. \tag{4.20}$$

For the experimental geometrical and optical parameters: $R_l = 4$ mm; $w_0 = 2$ mm; n = 3 the minimal focus waist is $w_{min} = 0.5$ mm at 200 GHz and 50 μm at 2 THz.
The focus area $A_{THz} = \pi w_{min}^2$ is very important because the measured signal is proportional to the electrical field which is in turn proportional to $(A_{THz})^{1/2}$, following the *Poynting-theorem*:

$$E_{THz} = 2\sqrt{\frac{P_{THz}}{A_{THz} c \epsilon_0}}. \tag{4.21}$$

P_{THz} is the THz-power on the detector. To increase the signal to noise ratio the focus has to be as small as possible, but because of the large wavelength of the THz pulse (1 THz ≡ 300 μm) and the dispersion limit the THz radiation can not be focused to very small spot sizes especially for the lowest frequencies of about 200 GHz. In this simplified consideration the effects of the dispersion in the dielectric materials (substrate, windows, lenses, air, GaAs-wafer, etc.), which changes additionally the THz pulse shape, are neglected. Because of the mentioned reasons of disalignment and dispersion the measured pulse at the detector has not exactly the shape of the pulse, which is emitted by the YBCO or LT-GaAs device. The pulse shape depends critical on the alignment of the quasi-optical system, which has to be adjusted very carefully to the smallest full width at half-maximum (FWHM) of the pulse.

4.1.5 Auston Switches as Emitters

In section 4.1.3 Auston switches were introduced as detectors of THz radiation. A photocurrent was measured generated by acceleration of optical injected free carriers due to an (unknown) external field. Neverthelss if a voltage is biased to an Auston switch this switch can *emit* THz pulses as well. The photoswitch consists of a coplanar transmission line of an AuGe/Ni/Au layer, which is patterned in the center to a dipole structure with a gap (5 μm long and 10 μm wide). The THz emission of such photoconductive antennas, illuminated by femtosecond laser pulses, is explained by optical carrier generation and subsequent acceleration in the applied electrical bias field resulting in a polarization P acting as source of the THz radiation. This is the so called *current surge model.*

Another possible way to generate a polarization of the charge carriers due to laser-mater interaction is the nonlinear χ^2 process [Jeps 96], where:

$$P = \chi^2(0, -\omega, \omega)E(\omega)E^*(-\omega). \tag{4.22}$$

This is a second order nonlinear process and therefore important at high laser intensities and not for the weak exciation limit. This interesting effect does not play a role in our experiment.

A schematic of the antenna, in a geometry proposed by Grischkowsky *et al.* [Kroek 89] is shown in fig. 4.4 a). The applied bias voltages (about 1..20 V in our experiment) generates high electrical fields $E_{bias} \approx 2..40\ kVcm^{-1}$ at the gap between the electrodes, because of the small geometrical size and the high dark resistance of GaAs. This electrical bias field results in a transient current flow and polarization of the electron-hole pairs after the optical illumination. From the *Maxwell laws* it can be understand, that this transient current generates an electrical field, which is emitted into free space. The emitted electrical field can be calculated by [Jac 00]:

$$\vec{E}_{THz} = -\vec{E}_{bias} \frac{\sigma_s(t) Z_0}{\sigma_s(t) Z_0 + 1 + \sqrt{\epsilon}}, \tag{4.23}$$

where $\sigma_s(t)$ is the surface conductivity, Z_0 is the free space impedance of about 377 Ω and ϵ is the dielectric constant of GaAs. The surface conductivity changes dramatically with the optical carrier injection. The dependence of the surface conductivity on laser intensity $I(t')$ and carrier mobility $\mu(t)$ can be written as [Beni 94]:

$$\sigma_s(t) = \frac{e(1-R)}{\hbar\omega} \int_{-\infty}^{t} \mu(t-t') I(t') e^{-(t-t')/\tau_c} dt'. \tag{4.24}$$

The time dependence of the mobility is described by equation (3.8). The emitted THz field E_{THz} can therefore be determined with the scattering time τ_s (equation (3.8)) and the carrier life time τ_c (equation (4.24)) as model fit parameters.

Because of the small size of the antenna compared to the emitted wavelength, the emitter can be treated as a point source. From the electrical circuit analogy of fig 4.4 the antenna can be described by a changing conductance G(t) parallel with a capacitance C and in line with an impedance Z. The antenna consists of a gap between two metal contacts and acts therefore like a capacitance and it is charged if an external dc bias voltage is applied [Sha 92] with a stored electrostatic energy of about:

$$E_{stored} = \frac{CV_{bias}^2}{2}, \tag{4.25}$$

where C is the capacitance of about 10 fF and V_{bias} the bias voltage smaller 10 V leading to E_{stored} <1 pJ [Jeps 96].

4.2 YBCO Devices as Emitters

In the previous section photoconductive antennas as emitters of THz radiation were introduced. A very different kind of material is also capable of THz emission: the high-T_C cuprate superconductors. As reported by different authors, current biased, optically excited superconducting microbridges emit submillimeter-wave radiation, which can be detected by means of a THz TDS set up [Nuss 91], [Jaek 96], [Hegm 95], [Hang 96] or by usage of the electro-optical sampling technique [Lind 99]. The THz TDS set-up used for the LT-GaAs samples, shown in fig. 4.1 is putted forward by introducing an optical cryostat for measurements at cryogenic temperatures. The THz pulse detector is a LT-GaAs dipole antenna. The cuprate superconductor, which is used in our experiments, is the material YBCO, described in chapter 2.

The characteristics of the radiation emitted by the cuprate superconductors can be related to the quasiparticle dynamics, described in the previous chapter. Two theories of explanation of the THz emission of YBCO microbridges exist: the *kinetic inductance model* [Bluz 92] and the *current modulation model* [Tono 96].

It is generally assumed that the THz emission is based on an optical induced transient change in the Cooper pair density. Previous investigations revealed, that the subpicosecond electrical field transients can be observed in optical thick films, where the film thickness is larger than the penetration depth (d>100 nm), and in ultrathin films with d in order of 10 nm, without significant differences in the emitted pulse shape. This excludes bolometric effects for an explanation of the emission [Hegm 95], because the heat escape to the substrate, which depends on the film thickness, would influence the signal shape.

The Cooper pair breaking and recombination can be qualitatively explained by rate equations which follow the 2T-model or the RT-model. Except for $T \rightarrow T_C$ the change in the Cooper pair density $\Delta n_s(T)$ is small compared to the overall Cooper pair density $n_s(T)$ (weak excitation limit). For $T << T_C$ it can be estimated that around 1% of the Cooper pairs are broken at moderate excitation conditions [Jaek 96]. After the cascade-Cooper pair breaking due to high-energy quasiparticles the maximum number of broken pairs is given by:

$$\Delta n_{max}(T) = \frac{E_{laser}}{2\Delta(T)}, \tag{4.26}$$

where $\Delta(T)$ is the temperature dependent superconducting gap energy. Taken the non-zero reflectance R($\approx 20\%$) into account the formula changes slightly[Tani 97]:

$$\Delta n_{max}(T) = (1-R)\frac{E_{laser}}{2\Delta(T)}\frac{(1-exp(-\alpha_p d))}{Ad}, \tag{4.27}$$

where α_p is the absorption coefficient, A the area of illumination, d the penetration depth. For laser powers of about 100 mW, the density of broken pairs is assumed to reach the total number of Cooper pairs (2 to $6\times10^{21}cm^{-3}$). The change in the Cooper pair density is assumed to cause the observed subpicosecond electromagnetic field, which is emitted if the superconductor is current biased or in the flux trapped state. A transport or a shielding current is necessary for the emission. After the generation of the pulse inside the film it is radiated through the substrate into free space. Because the refractive index missmatch between the YBCO film and the substrate is very high, the output coupling reduces the radiation power substantially. For a high radiation efficiency the refractive index missmatch has to be minimized for a higher output coupling. Due to trapping of mobile carriers by a substituation of Y by Pr atoms an improvement of the radiation efficiency of one order is reached and an optimum carrier doping is found experimentally by the author [Wald 02].

4.2.1 Thermal Properties and Heat Escape

In this section the thermal heating of the used YBCO thin film microbridge samples due to an optical excitation by a femtosecond laser illumination is described. The time constants of the processes are caclulated for the particular case of the used substrate materials and geometries. It is shown, that the time resolved evaluation of the heat transfer from the film to the substrate exhibits a characteristic duration longer than the observation time. The temperature fluctuations of the device are observed by an average signal offset in the measured response data of the PPT experiment. It has to be taken into account, that the repetition rate of the laser is 80 MHz and the laser beam is in addition chopped mechanically at 2 kHz to use a lock-in amplification technique.
The sample heating has an obvious critical influence on the sample properties near the transition temperature and can not be neglected at T near T_C even for low laser fluences, because of the very sensitive bolometric response. Also it has to be taken into account, that the quasiparticle lifetime (relaxation time) τ_{rec} is proportional to $1/\Delta$(T) and therefore it is depending on temperature [Han 90]. Δ(T) decreases abruptly when T_C is approached and a small temperature change results in a large change in τ_{rec} [Kaba 00]. The heat diffusion to the substrate is the bottleneck of the heat escape. This can explain that the observed long time fluctations in the PPT experiment are caused by an average temperature increase of the sample, which is not measurable by the temperature controller situated in the cold finger. An estimation of this effect is necessary because the amplitude of the investigated THz signal depends on temperature, see section 5.2.3. Below a threshold laser power, which depends on temperature, only the fast response signal appears and no bolometric response is observable [Zhao 98]. At temperatures above T_C but in the transition region the shift in the dc resistance R owing to laser heating can be used as a sensitive measure of the change in the average sample temperature. For YBCO the optical penetration depth δ at a wavelength of $\lambda = 810$ nm is around

100 nm [Yasu 91] and the absorption constant is $\alpha \approx 1.1 \times 10^5 cm^{-1}$ [Fren 93]. The film thickness d in the experiment is between 100 and 200 nm and for this calculation d= 150 nm is used. The calculation is made for 1 mm thick $LaAlO_3$ and 0.5 mm thick MgO substrates. The heat diffusion involves four processes if the YBCO film thickness is about the penetration depth [Zhao 98]:

- the diffusion from the absorption layer to the film/substrate boundary;
- the flow of heat over the film/substrate boundary;
- the diffusion inside the substrate to the substrate/heat sink boundary and
- the flow from the substrate into the heat sink across the boundary.

The characteristic time constant of the first process can be calculated by using the equation [Hegm 93]:

$$\tau_{diff} = \frac{d^2 C_{YBCO}}{\kappa}, \tag{4.28}$$

where κ is the thermal conductivity and C_{YBCO} is the specific heat of YBCO, respectively. The values for κ of YBCO are measured at single crystals [Peac 91] and depend on the sample quality and the direction of the heat flow [Hage 89]. At T = 80 K the value of κ in the ab-plane is about 0.12 W/cmK and 4 to 5 times smaller along the c-axis [Hage 89]. Introducing the concrete values: d=150 nm, $C_{YBCO} = 1\ J/cm^3$K and $\kappa = 0.026\ W/cmK$ (c-axis) the equation gives the result:

$\tau_{diff} = 8.6$ ns.

If large temperature changes are induced due to the laser illumination the temperature dependence of the specific heat of YBCO has to be taken into account: it changes from values of about $C_{YBCO} = 0.1\ J/cm^3K$ at T = 20 K to $C_{YBCO} = 1\ J/cm^3K$ at 85 K [Atake 91], [Sanc 92].
For the second process, the heat escape to the substrate, the characteristic time constant is given by:

$$\tau_{esc} = C_{YBCO} R_{bd} d, \tag{4.29}$$

here R_{bd} is the boundary resistance between YBCO and the substrate, $R_{bd} = 10^{-3}$Kcm^2/W for $LaAlO_3$ [Hegm 95]. This results in an escape time with the value:

$\tau_{esc} = 15$ ns.

At lower temperatures (below 30 K) the boundary resistance becomes temperature dependent like:

$$R_{bd} = \frac{B}{T^3}, \tag{4.30}$$

with the constant B$\approx 17 K^4 cm^2/W$ for YBCO on sapphire [Nahu 91]. Therefore the T^3 behavior will become significant below T=30 K and the thermal escape time of the film will increase further.
For the third process, the heat diffusion inside the substrate, the time constant is:

$$\tau_{sub} = \frac{d_{sub}^2 C_{sub}}{\kappa_{sub}}, \tag{4.31}$$

where for LaAlO$_3$: C$_{sub}$ = 0.4 $Jcm^{-3}K^{-1}$, κ_{sub} = 0.35 $Wcm^{-1}K^{-1}$ [Serg 94] and d$_{sub}$ = 1 mm. This leads to:

τ_{sub} = 11 ms.

For the used MgO substrate the parameters are: C$_{sub}$ = 3 $Jcm^{-3}K^{-1}$, κ_{sub} = 0.4 $Wcm^{-1}K^{-1}$ [Crys 01] and d$_{sub}$ = 0.5 mm. This leads to:

τ_{sub} = 19 ms.

For thinner films ($d \approx \delta$) the thermal boundary model is in a better agreement with the experimental results [Hegm 93], but thermal diffusion becomes more significant in thicker films ($d > \delta$), since the light is absorbed mainly in the 100 nm thick absorption layer.
The pulse train interval of the Ti:sapphire oscillator is 12.5 ns. The chopping time for the login amplification is about 500 μs. This is shorter than the time constant of the third process. In the THz emission experiment and the PPT method the longest used observation time is 100 ps. That means that above described bolometric processes do not play a role in the evaluation of the THz pulse, but has to be taken in to account for the estimation of the real temperature of the sample.
The temperature increase of the device due to laser illumination can be calculated by using [Nahu 91]:

$$\Delta T = \frac{F}{C_{YBCO}\delta}(1-R)(1-exp(\frac{-d}{\delta})), \tag{4.32}$$

where R is the reflectivity of YBCO. With the values at λ = 810 nm: R = 0.1 [Hegm 93], [Zibo 92] and δ = 100 nm and a laser fluence of F = 25 $\mu J/cm^2$ (laser power is assumed to be P = 10 mW and the laser focus to be 25μm, the laser can not be focused to such small spot sizes as for the LT-GaAs because of the used cryostat). This results in:

ΔT $\approx$ 2 K.

This corresponds to the highest transient temperature change during the experiment, not to the average temperature. Because in this model the temperature depends linearly on the laser fluence for the highest laser powers of about 100 mW a large temperature increase of about 20 K can be estimated.

4.2.2 Kinetic Inductance Model

In the superconducting state at temperatures $T < T_C$ the dc electrical current is carried by Coper pairs without dissipation. The superconducting carriers own a finite inertia, which causes a kinetic inductance. The kinetic inductance of superconducting strip lines has been investigated extensively [Pond 87]. If a femtosecond laser pulse illuminates a YBCO microbridge in the superconducting state, the photons break Cooper pairs. In the *kinetic inductance model* it is assumed that this results in a change of the kinetic inductance of the thin film microbridge [Bluz 92]:

$$\frac{\Delta L_{kin}}{\Delta t} = -\frac{m_s^*}{e^2 n_s^2} \frac{l}{wd} \frac{\Delta n_s}{\Delta t}. \tag{4.33}$$

Here m_s^* is the effective mass of the Cooper pairs, l, w, d are respectively the length, width and thickness of the YBCO microbridge. Because of this change in the kinetic inductance at a constant bias current a voltage transient across the film appears, which contributes to the photoresponse [Bluz 92], [Hegm 93], [Zhao 98], [Jaek 96]. Neglecting the normal carrier contribution, the current density is given by:

$$\vec{j}_s = e n_s \vec{v}_s, \tag{4.34}$$

where $\vec{v}_s$ is the Cooper pair velocity. If a constant bias current is applied to the bridge and the supercarrier density is decreased by the optical illumination, the velocity of the supercarriers will have to increase in order to maintain a constant current following the *kinetic-inductance model.* If the effect of the transient voltage on the normal carriers is not considered it can be written:

$$\frac{\partial \vec{j}_s}{\partial t} = n_s e \frac{\partial \vec{v}_s}{\partial t} + e \vec{v}_s \frac{\partial n_s}{\partial t}. \tag{4.35}$$

The first *London equation* and the condition of a constant current leads to a formula for the emitted electrical THz-field $\vec{E}_{THz}$:

$$\vec{E}_{THz}(T,t) = -\vec{j}_s \frac{m_s}{4e^2 n_s^2(T)} \cdot \frac{\partial n_s(T)}{\partial t}. \tag{4.36}$$

The emitted field is therefore proportional to the supercurrent density $\vec{j}_s$ and to $1/n_s^2$(T). A positive field tansient represents Cooper pair breaking and a negative field transient indicates Cooper pair recombination. The temporal change in the Cooper pair density can be described by using the 2T-model or the RT-equations [Lind 99], resulting in a normalized function $f(t)$ containing the full temporal evolution of the broken-pair density. This function $f(t)$ can be measured by means of optical time-domain transient reflectivity or transmission measurements [Jaek 96]. Lindgren *et al.* found by fitting the 2T- and RT-model to the THz pulse shape of YBCO a ratio for the specific heats of

phonons and electrons of C_{ph}/C_e=38 and a phonon-electron scattering time τ_{ph-e} of 42 ps.
Because following equation (4.26) the maximum number of broken pairs depends on temperature, we rewrite equation (4.36) in a way to predict a defined temperature dependence of the generated THz field:

$$\vec{E}_{THz}(T,t) \sim \frac{\Delta n_{max}(T)}{n_s^2(T)} \cdot \frac{\partial f}{\partial t}. \tag{4.37}$$

The temperature dependence of $n_{max}(T)$ and $n_s(T)$ is determined by the superconducting gap $\Delta(T)$. Nevertheless it is necessary to take the output coupling of the device into account, because in the low excitation limit the reflection and absorption losses at the film/substrate and substrate/air interfaces determine the temperature dependence of the measured THz signal in the far field [Jaek 96], [Tani 97].

4.2.3 Current Modulation Model

In the *kinetic inductance model* a constant bias current is assumed. But because no current source can supply constant currents coupled over coplanar transmission lines to the sample at frequencies above some GHz, this assumption is doubtfully. If it is supposed that the local current density can vary after the optical illumination, this effect leads to the THz emission in analogy with the widely accepted explanation of the emission mechanism of photoconductive emitters. This effect is described by the following *current modulation model* [Tono 96]. Here the emitted radiation field $\vec{E}_{THz}$ is proportional to the time derivation of the jurrent density $\vec{j}_s$:

$$\vec{E}_{THz} \sim \frac{\partial \vec{j}_s}{\partial t}. \tag{4.38}$$

It is mentioned above that the time derivation of the current density can be expressed as described by equation (4.35) and that the carrier density n$_s$ is reduced by optical induced Cooper pair breaking. In the *current modulation model* it is assumed now, that the average velocity $\vec{v}_s$ of the superconducting carriers remains nearly unchanged: $\partial\vec{v}_s/\partial t \approx 0$. Using again the *London equation* we get:

$$\vec{E}_{THz} \sim \frac{\vec{j}_s}{n_s(T)} \frac{\partial n_s(T)}{\partial t}. \tag{4.39}$$

The emitted THz field is therefore proportional to the supercurrent density $\vec{j}_s$ like in the *kinetic inductance model* but the dependence on the superconducting carrier density changes from $1/n_s^2$(T) to $1/n_s(T)$. Therefore by analyzing the temperature dependence both models could be compared theoretically. Nevertheless for an exact calculation the additional losses from the absorption inside the superconducting film and the reflection at the film/substrate interface has to be included, see the next section. The absorption and reflection losses change also with the complex conductivity of the superconducting film which depends on the mobile carrier density and the normal/superconducting carrier fractions inside the YBCO. This complicates the calculations.

4.2.4 Output Coupling

The radiation efficiency of the THz wave emitted by the YBCO device is defined by the ratio of the emitted THz power P_{THz} to the illuminated laser power P_{laser} and it is limited by several factors. The most important factors are: the absorption inside YBCO thin film itself, the output coupling at the film/substrate interface, at the substrate/lens and at the lens/free-space boundary and the transmission through the cryostat windows, reflection losses at the parabolodial mirrors, at the silicon lens and the at the lens/detector interface. For a simplification only the main loss mechanism are considered here: inside the film and at the film/substrate interface. Than the output coupling can be treated in the following way [Jaek 96]:

- Absorption: The absorption of the electrical field inside the film can be described by:

  $$E(x,T) = E_0\sqrt{t_1(T)t_2 e^{\left(\frac{-\alpha(T)x}{2}\right)}}, \tag{4.40}$$

  where x is the optical path of the THz pulse, t is the transmission coefficient and α the absorption coefficient. The absorption coefficient is connected to the reflectivity R and the real part of the complex conductivity σ_1 by the equation:

  $$\alpha = \frac{\sigma_1}{Rc\epsilon_0}. \tag{4.41}$$

  Here c is the speed of light and ϵ_0 the permittivity of free space. The complex conductivity can be measured by TDS measurements [Bror 96] yielding absorption length of about 100 nm at T=10 K for f = 0.5 THz.

- Transmission: The temperature dependent transmission coefficients of the interface between the superconducting film and the dielectric substrate are given by the formula:

  $$t_1(T) = \frac{4\bar{n}_{ybco}(T)\bar{n}_{sub}}{[(\bar{n}_{ybco}(T)+\bar{n}_{sub})^2 + \kappa^2_{ybco}(T)]}, \tag{4.42}$$

  with $n_{ybco} = \bar{n}_{ybco} - i\kappa_{ybco}$ as the temperature dependent complex refractive index of YBCO and $\bar{n}_{sub}$ as the refractive index of the substrate material (MgO or $\mathrm{LaAlO_3}$: $\bar{n}_{MgO}$=3.2 at f = 0.5 THz; $\bar{n}_{LaAlO_3}$=5 at f = 0.5 THz). The complex transmission coefficient $t_1(T)$ can be measured directly by means of the THz TDS [Bror 96]. The transmission coefficient of the substrate/air interface does not exhibit a significant temperature dependence in the temperature range of interest and it is given by:

  $$t_2 = \frac{4\bar{n}_{sub}}{(\bar{n}_{sub}+1)^2}. \tag{4.43}$$

- Refractive index $\bar{n}_{ybco}$(T): The refractive index of the superconductor depends on temperature and on the frequency of the electromagnetic wave. It can be estimated by using the general dependence [Jaek 96]:

  $$\bar{n}_{ybco}(T) = \frac{c}{\lambda_L(T)\omega}, \tag{4.44}$$

  where λ_L is the temperature dependent penetration depth of YBCO, which can be measured by different methods: THz time-domain spectroscopy [Bror 96] or SQUID (superconducting quantum interference device) measurements [Ilic 96]. Values of about 160 to 180 nm for λ_L(T = 0) are reported, yielding a $\bar{n}_{ybco}$(T→0)≈ 600 at f=0.5 THz.

Because the value of $\bar{n}_{ybco}$(T), mentioned above, is very high, the transmission coefficient t is very small: in order of 10^{-3}. It is therefore usefull to operate the superconducting devices at a temperature near T_C, where the refractive index decreases. In the weak excitation limit, when only about 1% of the Cooper pairs are broken, the temperature dependence of the THz radiation emission can be mainly attributed to the output coupling of the device [Tani 97]. The temperature dependence of the penetration depth was discussed earlier in section 3.2.1. Here it is assumed, that the absorbed energy from the laser pulse does not change with temperature, the temporal evolution of the gap parameter is neglected and n_s is assumed to be time independent because of the low density of broken pairs. At temperatures close to T_C the existence of the normal fluid has to be considered and the transient voltage causes resistive losses and heating, which reduces the emitted field.

Deviations from the behavior of equation (4.37) at high temperatures T→ T_C (>60 K) can be explained by the aproach of the current density to the critical value. Here the assumption of the weak excitation limit condition is not valid [Jaek 96], [Hegm 95]. For an exact temperature dependence of the THz emission the thermal shrinkage of the superconducting gap and the temperature dependent transmission and absorption coefficients of the film and the film/substrate interface have to be taken into account.

4.3 YBCO Device Preparation

The YBCO thin films with thickness of about 100 to 200 nm are grown by magnetron sputtering technique [Tono 02] and pulsed laser deposition (PLD) technique on dielectric MgO and $LaAlO_3$ 10×10 mm^2 substrates, 0.5 mm and 1 mm thick, respectively [Borc 93]. After film deposition the films are patterned by photolithography and ion beam etching. The sample structures consist of a coplanar transmission line structure about 6 mm long and connected in the middle by a 20 μm wide and 25 μm long dipole antenna, see fig. 4.6.

MgO substrates exhibit excellent high frequency properties: loss tan $\delta = 9 \times 10^{-3}$ and $\epsilon \approx 8.1$ at T=77 K and f = 10 GHz [Crys 01]. The refractive index in the THz frequency range (200 GHz to 2 THz) is about 3.1 and does only slightly depend on frequency, and the power absorption at these frequencies is below 1 cm^{-1} at T = 77 K [Gris 90]. The

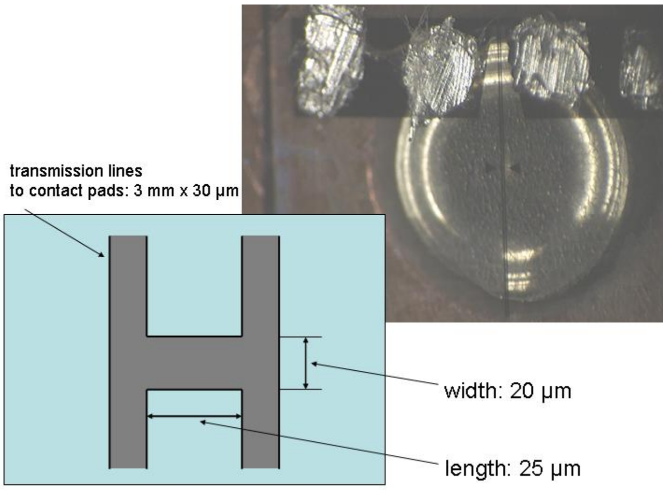

Fig. 4.6: Schematic picture and photograph of the YBCO dipole antenna.

lattice misfit of MgO to the YBCO crystal *a*-*b*-plane (9%) is larger compared to other commonly used substrates (e.g. $SrTiO_3$ 1%).
$LaAlO_3$ substrates exhibit worse high frequency properties compared to MgO: loss tan $\delta = 2 \times 10^{-4}$ and $\epsilon \approx 22$ at T = 77 K and f = 8.8 GHz [Crys 01]. The refrative index at liquid nitrogen temperature is about 4.8 at f = 200 GHz and 5.1 at f = 2 THz and the power absorption at those frequencies reaches 15 cm^{-1} with a strong frequency dependence [Gris 90]. Nevertheless both substrates are favorable to $SrTiO_3$, which has the best lattice adaption, because this substrate material exhibit high losses at f = 10 GHz: $\epsilon = 300..2000$ and loss tangent $tan\delta \approx 2 \times 10^{-2}$.
The concrete deposition conditions of the PLD films used in the experiments are the following: the residual gas pressure after evacuation of the chamber: $p \approx 10^{-4}$Pa, the oxygen gas pressure while deposition: $p_{O_2} \approx 20...70 Pa$, the heater temperature while deposition: $T_h \approx 670..710$ °C, the laser energy: $E = 550 mJ$ and a repetition rate of f = 5 Hz.
Experimental results of the temperature dependence of the critical current density and the specific resistivity of the superconducting samples are summarized in section 5.1.

4.3.1 Multilayer Samples

Experiments on ultrathin YBCO layers, embedded into isolating $PrBa_2Cu_3O_7$ (PBCO) layers, show that the transition temperature and the critical current density decreases with a decreasing thickness of the superconducting layers [Tris 90]. This effect is explained by a depletion of mobile charge carriers in the YBCO. The emptying of the mobile holes occurs by a transfer across the interface to the adjacent material [Ciep 94]. In experiments to investigate the dependence of the THz radiation efficiency on the carrier doping, the free carrier number is reduced by deposition of such a multilayer system, see fig 4.7, consisting of thin isolating PBCO layers and superconducting YBCO layers, like described elsewhere [Ciep 94].

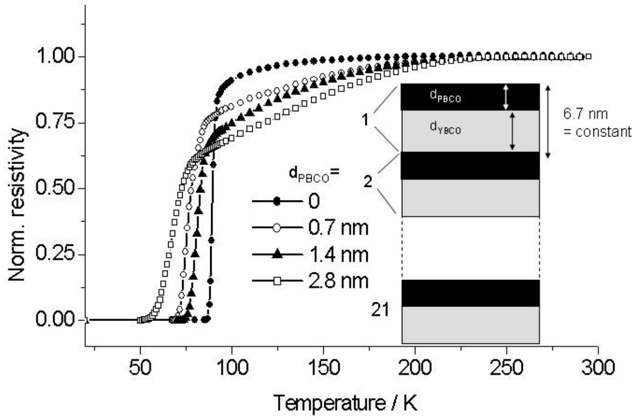

Fig. 4.7: Schematic picture of the YBCO/PBCO multilayer structure and the connected change in the temperature dependence of the normalized specific resisitivity.

The substrate material is 1 mm thick $LaAlO_3$ 10× 10 mm^2 and the PLD technique is used for deposition.
The thickness of the whole multilayer structure is about 150 nm. One double layer of YBCO/PBCO is around 6.6 nm thick. In dependence on the doping, which is tried to obtained, the ratio of the PBCO and YBCO layers is varied. For instance in the case of x = 20 % doping there is an 1.3 nm PBCO layer and a 5.3 nm thick YBCO layer ablated in one double layer and 22 of such double layers form the whole multilayer, i.e. 20 % of the multilayer consists of PBCO. The doping content varies from 0 % (pure YBCO) to 40 %.
In a post annealing process all multilayer samples are together heated to 500 °C in oxygen atmosphere for one our. After annealing the T_C and j_C of the pure YBCO film does not change significantly, but the T_C's and j_C's of the multilayers changes like predicted previously [Ciep 94], see fig. 4.7.

4.4 The PPT Experiment

For the THz emission, described in section 4.1.5 and 4.2, a femtosecond laser pulse is radiated to the emitter. The set-up is now changed in that way that an *additional* laser pulse excites the sample (a YBCO or a LT-GaAs antenna, respectively), before and during the THz pulse is generated by the antenna. To realize this *additional* excitation, the laser beam is divided into three beams: the *trigger* pulse for the LT-GaAs detector and the *probe* laser pulse, which generates the THz signal (which is measured) like described before and the *pump* laser pulse for the excitation of the sample (see fig. 4.8). Because two laser pulses excite the sample in this experiment, two THz pulses will be emitted, delayed to each other by the time delay between the pump and the probe laser pulse (fig. 4.9). The THz radiation (2) emitted by the probe laser pulse is changed due

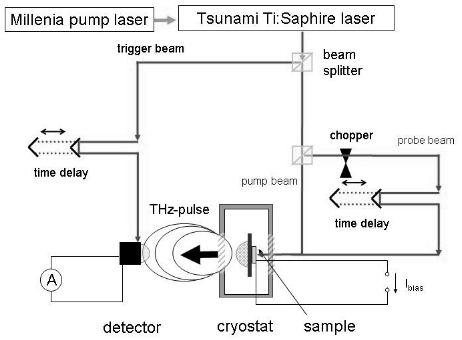

Fig. 4.8: The experimental set-up of the PPT system.

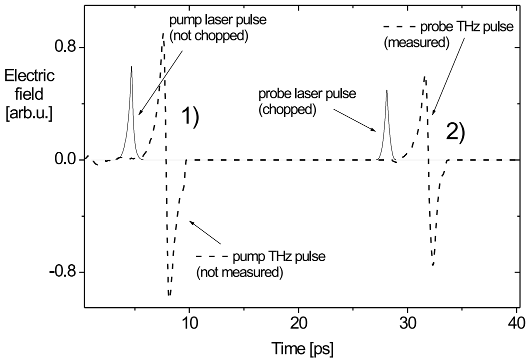

Fig. 4.9: The temporal regime of the laser and the THz pulses (schematically).

to the pump laser excitation. This time resolved change can be measured by the variable pump-probe time delay (-50 to 150 ps), which is realized by an additional translation stage. The spatial resolution of the translation stage is $1\mu m$ (6.6 fs in time domain). Only the probe laser beam is chopped by usage of a mechanical chopper at a frequency of 2 kHz to realize the lock-in amplification technique. This separates pump and probe THz signals. Therefore the THz signal (1) generated by the pump pulse is not observed with the detector, an dipole LT-GaAs antenna. Nevertheless, if the probe laser pulse arrives before the pump laser pulse (at negative time delays) this THz pulse (1) can be changed by the probe laser pulse, and this change will be measured by the detector, because it is modulated at the chopper frequency. That means the probe laser power has to be much smaller than the pump power. Because pump and probe laser pulses are coherent to each other a coherence peak appears in the signal. This can be described by the first-order autocorrelation function [Verg 96]:

$$g^{(1)}(\tau) = \frac{\langle E^*(t)E(t+\tau)\rangle}{\langle E^*(t)E(t)\rangle}. \tag{4.45}$$

The measured autocorrelation trace of both laser beams indicates that the time resolution of the system is almost 100 fs. To avoid coherent artifacts of the autocorrelation, the laser beams can be polarized orthogonally by using $\lambda/2$-plates. The position of the coherent artifact is not the moment which we choose as zero point of the pump-probe time delay in our experiment. But this artifact indicates the zero position with respect to the both *laser* pulses. Nevertheless the *measured* THz probe signal (2) is delayed to the probe laser pulse, fig. 4.9, and therefore it starts to change because of the pump laser beam induced changes *before* the coherent artifact appears. To make the situation more clear in the figs. 4.10 to 4.14 schematic pictures of different positions in time of the pump laser pulse, the probe laser pulse, the pump THz pulse and the probe THz pulse are drawn. The time in all the figures is fixed at the pump laser pulse position and the probe laser pulse moves in time from minus (before pumping) to plus (after pumpig). Because the probe THz signal is measured in our experiment, the pump-probe time delay t is the time delay between the *pump laser pulse* and the *probe THz pulse amplitude*. In fig. 4.10, at negative pump-probe time delays, the probe THz amplitude, which will be called PPT signal from now, is not influenced neither by the pump laser pulse nor by the pump THz pulse. From the moment t = 0 the PPT signal starts to change because it is influenced by the excitation of the sample due to the laser pump beam. This time nevertheless can not be determined exactly, because we do not know how long the probe THz pulse is delayed to the probe laser pulse. Therefore we choose the zero point at the position when the measured signal starts to deviate from its constant value more than the noise level of about 15 μV (fig. 4.11). Here it has to be considered that the lock-in technique produces a PPT signal which is influenced by the earlier mentioned changes of the *pump THz pulse* induced by the chopped probe laser beam and oscillating at 2 kHz. In fig. 4.12 the probe laser is still ahead to the pump laser, but the PPT signal is situated after the pump laser and while the pump THz pulse is generated. Therefore the PPT signal itself is influenced by both: pump laser and pump THz pulse. From the position of the mentioned coherent artifact, when the laser pump and probe pulses arrive at the same time (fig. 4.13), the probe laser beam itself will be influenced by the pump laser beam and at time delays after the pump THz pulse is emitted, the PPT signal will still be influenced by the induced changes due to the laser pump pulse but no longer by the pump THz pulse (fig. 4.14).

Two different experiments, using the above described set-up, where realized:

- The first experiment measures the temporal evaluation of the THz pulse amplitude after the optical excitation by changing only the pump-probe time delay, while the trigger time of the detector is always in the maximum amplitude of the probe THz pulse (2).
- The second experiment measures the whole waveform of the probe THz pulse (2) by changing the trigger time (as in the THz emission experiment) for different pump-probe time delays.

The measurements are carried out with a probe laser energy per pulse of about $E_{probe} =$ 1 to 2 $10^{-2} nJ$ (0.5..1 mW). The energy fluence can be calculated by assuming a focus waist of 10 μm: $F_{probe} \approx$ 8 to 16 $\mu J cm^{-2}$. The maximum laser pump fluence is 560 $\mu J cm^{-2}$. In the case of the superconducting samples the bias current is varied from -350 mA to 350 mA, near the critical current. At experiments with the photoconductive samples bias voltages of about 1 to 20 V have been used.

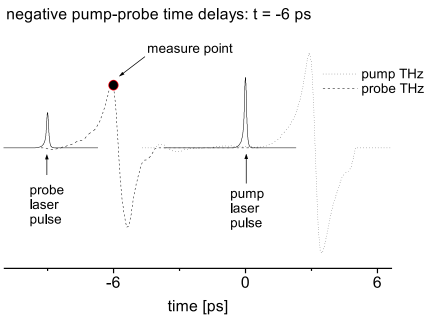

Fig. 4.10: The PPT signal is not influenced by the pump laser.

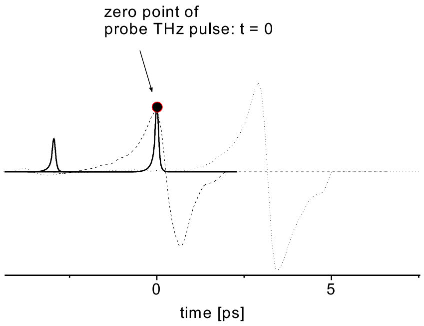

Fig. 4.11: The PPT starts to change because of the pump laser.

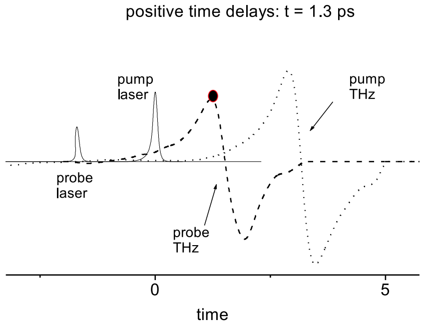

Fig. 4.12: The PPT signal is influenced by both: pump laser/pump THz.

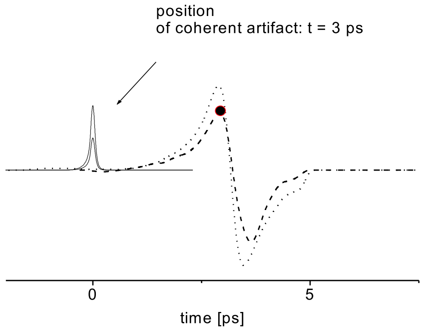

Fig. 4.13: The autocorrelation leads to the coherent artifact in the PPT signal.

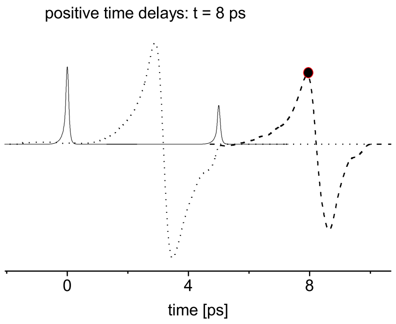

Fig. 4.14: The PPT signal is still influenced by the pump laser.

5 Results of THz Emission Experiments

This chapter summarizes the basic results of the THz emission experiments on YBCO and LT-GaAs dipole antennas under femtosecond optical illumination. The knowledge of the THz emission properties is necessary to analyze and understand the results of the PPT measurements. Especially the dependencies of the emitted THz radiation on the sample properties as well as on the excitation conditions are important. At first the temperature dependence of the critical current density and specific resistivity of the superconducting samples has to be measured, because the THz emission and PPT experiments with the YBCO samples are realized at different temperatures below T_C and it is aspired to relate the results of the PPT method to the superconducting gap $\Delta(T)$.

5.1 Temperature Dependence of the Specific Resistivity and Critical Current Density (YBCO)

After pattering the YBCO thin film microbridges were characterized by measurements of the temperature dependency of the resistivity R(T) from room temperature down to 20 K. The electrical resistivity R is measured by means of a current biased and voltage measured 4-point-method with copper wires contacted to gold pads on the film via an indium paste, see photograph of fig. 4.6. Fig. 5.1 indicates the specific resistance of the microbridge $\rho(T) = (R(T)dw)/l$ (w: width, d: film thickness, l: length) as function of the controller temperature T. The temperature is measured by a Si-diode in thermal contact to the heat sink on which the sample is mounted by a low-temperature paste. The temperature difference between sample and Si-diode is estimated to be smaller than 1 K [Kiwa 98]. The specific resistivity of the investigated YBCO samples is typically about 330 $\mu\Omega cm$ at T=300 K, very close to values reported elsewhere [Pool 95p28].

The fit (solid line without points), shown in fig. 5.1, is calculated by the *Bloch-Grüneisen*-equation (equation (3.15), chapter 3) and gives a theoretical dc resistivity of the normal carriers of about 0.1 $m\Omega cm$ at T = 0 K. A more simple linear fit (dotted line in fig 5.1) to the high temperature linear resistivity behavior gives a $\rho = 0.06$ $m\Omega cm$ at T= 0 K. From the electrical dc resistivity in the normal state the electron (hole) scattering rate Γ can be (in the simpliest case of isotropic material with quasi-free carriers) approximatly calculated by equation 3.16 of chapter 3. From the measurement of $\rho(T)$ and this equation a dc scattering rate Γ of 80 cm^{-1} ($\tau \approx 400$ fs) at T = 10 K can be deduced, which is comparable to the value of scattering rates Γ obtained from infrared spectroscopy of about 100 cm^{-1} ($\tau \approx 330$ fs) [Flik 92] or $\Gamma = 300 cm^{-1}$ ($\tau \approx 110$ fs), ρ = 0.3 $m\Omega cm$ [Bonn 88], despite the very simple model.

The voltage-current characteristics V(I) of the microbridges below T_C show the typical behavior: from zero bias current starting without voltage drop, changing with higher

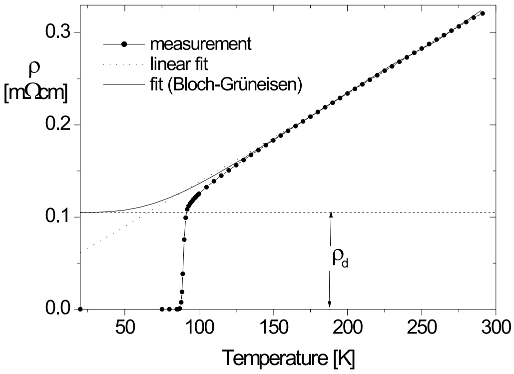

Fig. 5.1: The measured temperature dependence of ρ of the YBCO (line with points) and the Bloch-Grüneisen fit (solid line), described in chapter 3 and a linear fit (points).

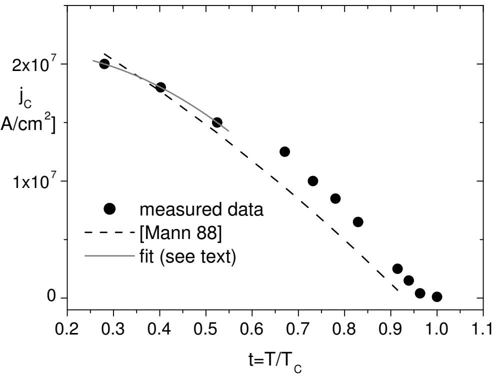

Fig. 5.2: The measured temperature dependence of j_C of YBCO and fits to the flux-creep model, described in chapter 2.

currents to the flux-flow-state with low voltage across the bridge and finally passing into the resistive state. The rapid increase of voltage with current above a certain value in the resistive state depends on the formation of a hot spot in the bridge region, which causes a fast temperature rise [Poul 95], [Fren 89].

The critical bias current I_C of the microbridges at different temperatures from below T_C down to 17 K is determined by a voltage criterion of 5 μV across the microbridge with geometrical size of 20 × 25 μm^2 (width × length), i.e. an average electric field strength of 2 mV/cm. Fig. 5.2 shows the temperature dependence of the critical current density of one sample from $0.2\times T_C$ to T_C. The critical current density of the devices exhibits a nearly linear temperature dependence for temperatures between $0.5\times T_C$ and $0.9\times T_C$ which was previously observed by other groups at thin films of YBCO [Kuma 92]. The measured values of $j_C(T = 77\ K)$ of about $1\times 10^7 A/cm^2$ are comparable to values published elsewhere [Borc 93]. A fit based on equation (3.42) of chapter 3 with $\alpha = 0.31$ and β = -1.62 is indicated in fig. 5.2 as solid line. From this fit a critical current density of $j_C(T{=}0) = 2.3\times 10^7 A/cm^2$ can be deduced. As dashed line in fig. 5.2 a second fit based on the parameters found by Mannhart *et al.* [Mann 88] (α = 0.72; β = -0.38) for critical currents accross [001] tilt boundaries of YBCO on $SrTiO_3$ substrates and a smaller electric field criteria (1mV/cm) is additionally shown. Approximating Ω of equation 3.43 by a typical phonon frequency of 10^{10} Hz [Yesh 88], $|\vec{B}| \approx 12$ mT by the transport current induced self-field, and a by about 7 nm (the average flux line spacing [Flik 92]) yields an activation energy $U(\vec{B},0)$ of about 36 meV for the samples comparable to values of Foldeaki *et al.* of 34 to 67 meV [Folde 89]. Mannhart *et al.* calculated a value of 70 meV for the pinning vortex energy potential. The difference of the energy can be explained by the enhanced pinning in the artificial grain boundary used in the Mannhart *et al.* experiments. The calculated data of the vortex pinning

potential energy is important for the PPT experiments to investigate the dynamics of the *flux-trapped* state of YBCO (chapter 6).
The broaden of the resistance transition as function of the temperature for an increasing bias current [Hegm 93] can be used for analyzing the temperature dependence of the PPT experiment at temperatures near T_C.

5.2 THz Emission Waveforms and their Fourier Transformations

The waveform of the emitted electrical pulses in the far-field is measured by using the time resolved THz spectroscopy technique with a photoconductive dipole detector, like described in chapter 4. It is reported that current biased YBCO microbridges under femtosecond illumination emit electromagnetic fields with a full-width-at-half-maximum (FWHM) shorter than 1 ps [Hang 96], [Tono 96], [Hegm 95], [Jaek 96]. Fig. 5.3 shows the pulse shape of an electrical field emitted by an YBCO dipole antenna at T = 22 K, P_{laser} = 20 mW and I_{bias} = 100 mA in the time domain measured by a LT-GaAs dipole antenna.

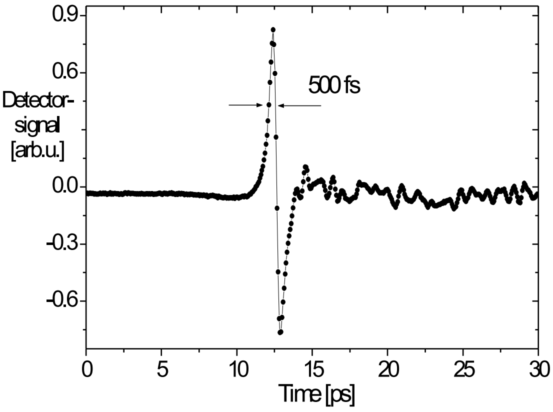

Fig. 5.3: The measured THz pulse shape of an YBCO dipole antenna at T = 22 K, P_{laser} = 20 mW and I_{bias} = 100 mA in the time domain.

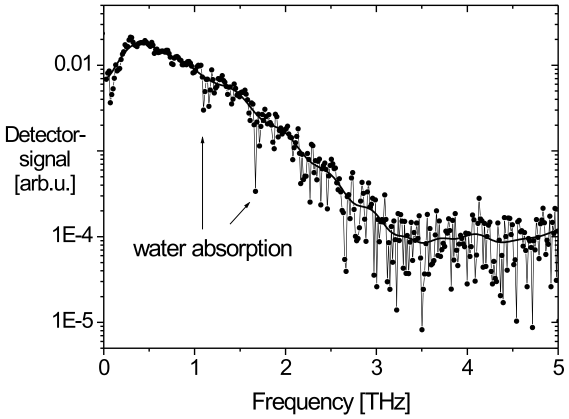

Fig. 5.4: The calculated Fourier transformation of the measured pulse shown in fig. 5.3.

The measured electrical THz field depends on the excitation conditions and the properties of the detecting device, like described in chapter 4. The zero point of the time scale in fig. 5.3 is arbitrary. The pulse shows many small oscillations following the main peak at t = 12 ps. These oscillations are caused by the absorption losses of the electrical field in the water vapor of the air [Tani 97]. The point in time when the optical excitation occurs, can not be identified exactly. In the PPT experiments the optical excitation becomes observable due to the coherent artifact of pump and probe beam. This effect is used to *ad hoc* define t = 0 by a criterion which takes the zero point as the point, when

the PPT signal first deviates from the noise level by $5 \mu V$.
The observed THz pulses emitted by the YBCO devices exhibit in general FWHMs of about 0.5 ps. FWHMs, which were reported previously, are close to this value (Tani *et al.* [Tani 97]: 0.5 ps, Hegmann *et al.*: 1.5 ps [Hegm 95] and Lindgren *et al.* [Lind 99]: 0.86 ps). The experimental technique of [Hegm 95] and [Lind 99] is the electro-optical sampling method. In this technique the field is measured by using a electro-active crystal of $LiTaO_3$ directly contacted to the superconductor, about $20 \mu m$ away from the excitation area. Nevertheless the observed pulse shape is close to the pulses oberserved by photoconductive antennas in the far-field. This implies that the detection device does not influence the detected signal significantly. It is possible to transform the experimental data, which are measured in the time domain, to the frequency domain by using the Fourier Transformation (FT). The result of the FT of the time resolved pulse of fig. 5.3 is shown in fig. 5.4. The amplitude of the signal reach its maximum at frequencies of about 400 to 500 GHz, as reported elsewhere [Jaek 96], [Tono 96]. The highest frequency components have values higher than 2 THz. The mentioned absorption of the pulse due to water vapor in the optical path results in a signal reduction of the FT at defined frequencies. The high-pass behavior at low frequencies is the result of the spectral response of the detector.

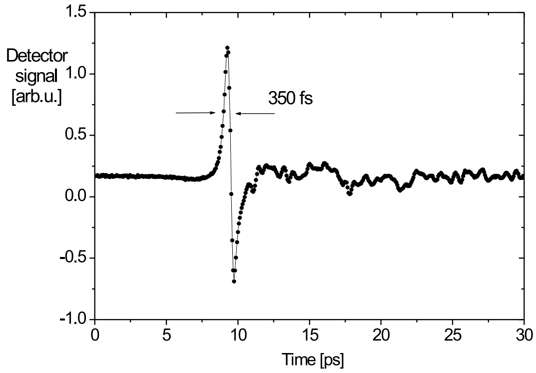

Fig. 5.5: The measured THz pulse shape of an LT-GaAs dipole antenna at T = 300 K, P_{laser} = 10 mW and V_{bias} = 5 V in the time domain.

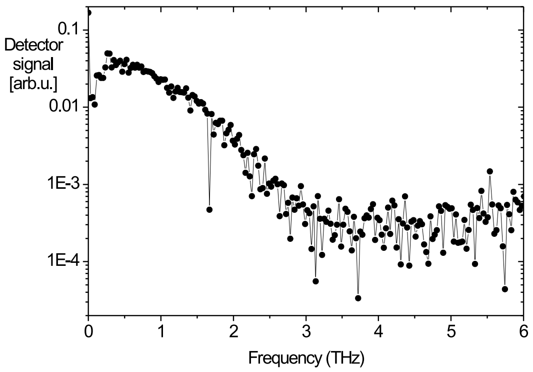

Fig. 5.6: The calculated Fourier transformation of the THz pulse shown in fig. 5.5.

Fig. 5.5 inditates the pulse shape of an electrical field emitted by a LT-GaAs dipole antenna with an identical photoconductive antenna as detecting device in the time domain at a temperature T = 300 K, a bias voltage V = 5 V and a laser power P_{laser} = 10 mW. The FWHM is about 350 fs and the FT of this pulse, see fig. 5.6, shows frequency components up to near 2.5 THz. The pulse exhibits also small oscillations following the main peak, because of the residual water vapor absorption.

5.2.1 Bias Current and Bias Voltage Dependence of the THz-Signal

The amplitude of the emitted THz pulse of an YBCO device is found to be propotional to the bias current E$_{THz} \sim I_{bias}$ [Hegm 93], [Fren 90], [Bluz 91], [Seme 93], [Nebo 93] for a current below the critical value. Fig. 5.7 shows the measured bias current dependence of the THz pulse amplitude of a 200 nm thick, $100 \times 100\mu m^2$ YBCO dipole antenna on a MgO substrate at T = 22 K and a laser power P$_{laser}$ = 50 mW.

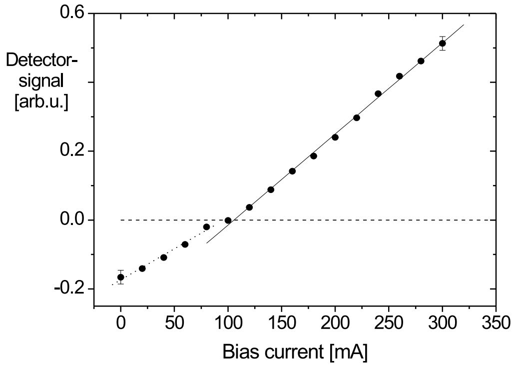

Fig. 5.7: The measured bias current dependence of the emitted pulse amplitude at T = 22 K of the YBCO microbridge device.

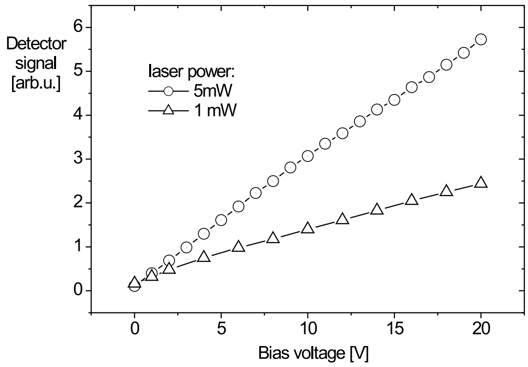

Fig. 5.8: The measured bias voltage dependence of the emitted THz-pulse amplitude at T = 300 K of the LT-GaAs dipole antenna.

The emitted signal amplitude is zero for a non-zero bias current ($\approx$ 100 mA), what can be explained by the flux-trapped state of the superconducting microbridge, where the trapped flux generates a current. Heating up of this device above T$_C$ and subsequent cooling in zero field results in a vanishing zero bias THz emission. The shielding current, produced by the flux pinned inside the film, is about 100 mA in this case. The flux-trapped state can be investigated by means of the PPT method and therefore the bias dependence of the THz emission in the flux-trapped state is measured. Below 100 mA the THz amplitude is negative and changes its sign at a bias current of 100 mA. That means, the order of the value of the trapped magnetic flux density can be estimated by the simple equation:

$$|\vec{B}| = \mu_0 \frac{I_0}{2a} = 630\mu T, \tag{5.1}$$

where $2a$ is the microbridge width of 100 μm and I_0 the bias current at which the THz amplitude is zero. The magnetic flux is than $\Phi = |\vec{B}|(2a)^2 = 6.3\ 10^{-8} Tcm^2 \approx 2.4\ 10^5 \Phi_0$. At bias currents below 100 mA the THz signal amplitude depends not exactly linear on the bias current, because of the decrease in the flux density due to bias current-flux interaction (*Lorentz-force*). This leads to a step in the THz-signal amplitude at I$_{bias}$ = 100 mA and a small nonlinear component at I$_{bias}$ < 100 mA. This nonlinear component is the average value of the *optical injuced flux depinning process*, observed in the PPT

experiment.
The linear bias current dependence of the THz emission amplitude (in fig. 5.7 at bias currents I_{bias} above 100 mA) suggests that a suppression of the superconducting order parameter by the excess quasiparticle distribution is probably not the origin of the nonbolometric effect [Hegm 93]. The models to explain the THz emission due to a change in the kinetic inductance (section 4.2.2, equation (4.36)) as well as due to a bias current modulation (section 4.2.3, equation (4.39)) can explain the linear bias current dependence.
The measured THz amplitude of the LT-GaAs switch depends linearly on the bias voltage (fig. 5.8), like reported elsewhere [Tani 97b]. This behavior is predicted by equation (4.23) of section 4.1.5. For higher bias voltages a saturation effect occurs [Jeps 96], which is not considered here, because the LT-GaAs antennas are operated at not too high voltages. At high fields at the gap of the antenna (20 V$\doteq$ $40kVcm^{-1}$) a destruction of the device due to heating is possible.

5.2.2 Laser Power Dependence of the THz-Signal

The measured THz-signal amplitude of the YBCO device is proportional to the incident laser power: $\mathrm{E}_{THz} \sim P_{laser}$ (fig. 5.9) for the weak excitation limit, like predicted by equation (4.26) of chapter 4.

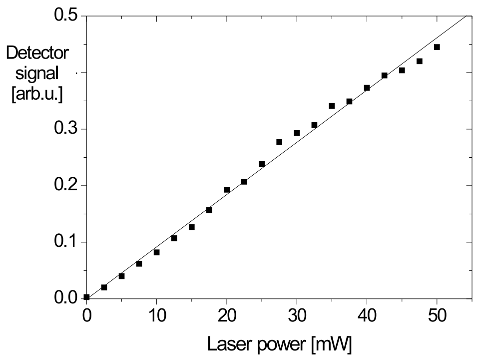

Fig. 5.9: The measured laser power dependence of the emitted pulse amplitude at T = 22 K of the YBCO microbridge device.

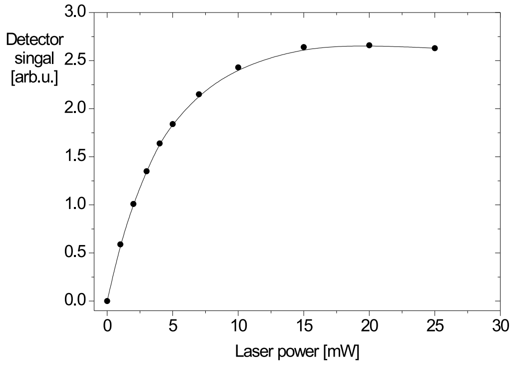

Fig. 5.10: The measured laser power dependence of the emitted THz-pulse amplitude at T = 300 K of the LT-GaAs dipole antenna, the solid line is a fit based on equation (5.2).

At higher laser powers, above a threshold value, the signal amplitude deviates from the linear behavior [Tani 97], what can be explained by a change in the output coupling efficiency by the transient change in the supercarrier density and the heating due to the laser excitation [Tani 97].
The emitted THz ampltitude of the LT-GaAs antenna depends linear on the incident laser power only at very low laser powers < 5 mW, see fig. 5.10. For higher laser powers

the dependence diverges from the linear behavior and saturates at about 15 mW. This saturation of the THz amplitude can be attributed to screening of the bias field by optical excited carriers [Tani 97]. Such saturation effects by carrier screening in the case of large-aperture photoconductive antennas were discussed previously by Darrow *et al.* [Darr 92]. They proposed that the THz amplitude E_{THz} depends on the laser intensity like:

$$E_{THz} \sim \frac{I/I_0}{1+I/I_0}, \tag{5.2}$$

with I/I_0 as the normalized optical intensity. Though the boundary conditions of large aperture antennas and dipole antennas are not equal, the influence of the carrier screening on the THz amplitude can be expected to be the same [Tani 97]. Equation (5.2) can be fitted to the measured laser power dependence well.

5.2.3 Temperature Dependence of the THz-Signal Amplitude (YBCO)

Fig 5.11 shows the temperature dependence of the THz-signal amplitude of an YBCO sample at different laser powers and bias currents, see inset. The signal amplitude increases with increasing temperature, especially near T_C.

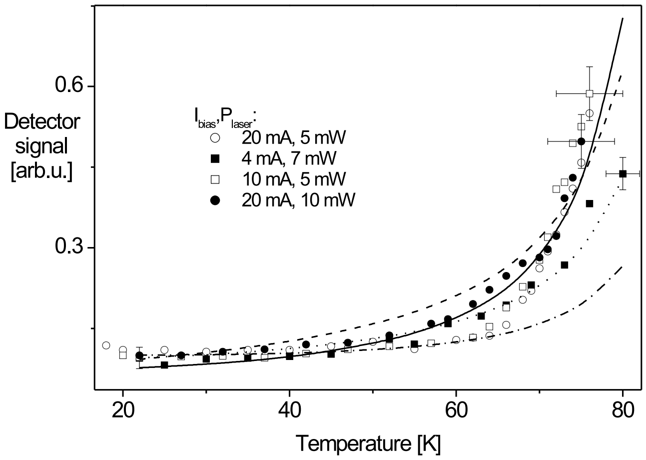

Fig. 5.11: The measured temperature dependence of the emitted THz-pulse amplitude of an YBCO sample. The fits are described in the text.

It is generally assumed, that this observed temperature dependence is caused by a change in the superconducting gap $\Delta(T)$ with T, i.e. the gap shrinkage at higher temperatures [Tani 97], [Jaek 96]. Like described in the previous chapter, the temperature dependence of the superconducting gap influences on one side the generation of the THz radiation, because the number of broken pairs Δn_{max} (equation (4.27)) and the total number of Cooper pairs n_s depend on the gap size. On the other side the output coupling

of the THz wave on the film/substrate interface changes also with the temperature, because the complex conductivity σ depends on T. This dependence is discussed in detail by Brorson *et al.*, who measured σ of YBCO at different temperatures by means of time domain THz spectroscopy (TDS) [Bror 96]. For an exact calculation of the temperature dependence all effects have to be taken into account. The fits, indicated in fig. 5.11, are calculated as follows:
1) The dashed line fit uses the *kinetic inductance model* (equation (4.36)) with a BCS-like temperature dependence ($\alpha = 1$), but does not take the output coupling into account.
2) The solid line fit uses the *current modulation model* (equation (4.39)) with a temperature dependence $\alpha = 2$ and takes the output coupling additionally into account.
3) The dotted line fit uses the *current modulation model* (equation (4.39)) with a temperature dependence $\alpha = 2$, but does not take the output coupling into account.
4) The dash-dotted line uses the *kinetic inductance model* (equation (4.36)) with a temperature dependence of Gorter and Casimir ($\alpha = 4$), but does not take the output coupling into account.
Other fits leads to worse results compared to the measured dependence of the signal amplitude on temperature. If output coupling plays a role in the THz emission, the *current modulation model* gives better agreement to the observed data. Nevertheless it has to be mentioned that at higher temperatures the sample temperature may be higher than the controller temperature because of heating and runnaway effects. Therefore a clear conclusion about the validity of the models is not reached. The temperature dependence following Gorter and Casimir does not fit to the data sufficiently.
Some authors reported the existence of a peak in the THz-signal amplitude at a certain temperature and a subsequent decrease with increasing temperature near T_C [Tani 97]. In our experiments this behavior was only observed at higher laser powers and bias currents. Fig. 5.12 indicates the dependence of the emitted THz amplitude on temperature of a multilayer sample, which shows a reduced critical temperature and critical current density compared to YBCO. Together with the emission amplitude a voltage drop on the bridge is measured, which apears while the laser illumination at higher temperatures. Please note the logarithmic right scale (voltage). Above a voltage of about 0.1 mV the THz amplitude starts to decrease significanly. Therefore it can be assumed, that the reduction of the THz signal amplitude at higher temperatures is due to current induced heating and runnaway effects, leading to hot spot formation. The voltage drop is related to the electron temperature like:

$$\Delta V = I_{bias}\frac{dR}{dT}\Delta T \tag{5.3}$$

The change in the resistivity with temperature can be deduced from the R(T) measurement. From the voltage drop the average temperature rise can be calculated. To measure the temperature dependence of the THz emission the laser power and the bias current has to be choosen very small, because of the heating of the device if its temperature reaches T_C this could destroy the device or enlarge the temperature gradient between sample and controller temperature.
The THz emission of the LT-GaAs dipole antenna is measured solely at room temperature because the cryostat was not used in the experiments with the photoconductive devices. The measurements at low temperatures in the case of GaAs are future prospects.

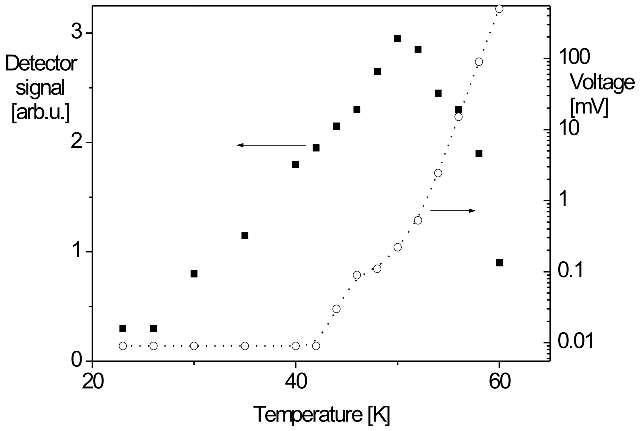

Fig. 5.12: The measured temperature dependence of the emitted THz-pulse amplitude of a multilayer sample at a laser power of P_{laser} = 15 mW and bias current of I_{bias} = 10 mA (filled squares) and the connected voltage drop at the device (open circles).

5.3 Influence of Carrier Doping on the THz Emission Efficiency

The maximum THz radiation output power of the used YBCO devices is a very important issue for the possibility of their application. It is limited by the saturation effect at higher laser powers, the device heating, the output coupling effects and the maximum critical current of the device. To increase the emission power the output coupling can be improved. We reported previosly that by usage of a multilayer system of YBCO/PBCO the emission efficiency of the device can be influenced substantially [Wald 02a]. To compare the signals of the different devices the alignment of all samples has to be exactly the same. It can be assumed, that the influence of the optical path between the radiation source and the detecting device is equal for all samples. There is no significant change in the shape and the width of the pulses emitted from the underdoped devices compared to the sample made of pure YBCO, only the signal amplitude depends clearly on the thickness d_{PBCO} of the PBCO layer in the multilayer structure. There are no resonance features in the signal due to geometrical effects of the multilayer structure, because $d_{PBCO} << \lambda_{THz}$. At a constant bias current and incident laser power the radiation amplitude increases with larger d_{PBCO}, i.e. a lower carrier density n_s. The efficiency of the radiation depends quadratically on the amplitude of the electric field E_{THz}. Fig. 5.13 indicates the bias current dependencies of 4 samples with different d_{PBCO} at the same excitation conditions and the same temperature T= 20 K.

The highest output power of the emitted THz signal is reached in the case of the ≈10% doped samples. Here the signal amplitude is around 6 times larger compared to the YBCO device, operating at the same bias current, and even up to 3 times higher as the signal amplitude of YBCO at the critical current of the device. Calculations of

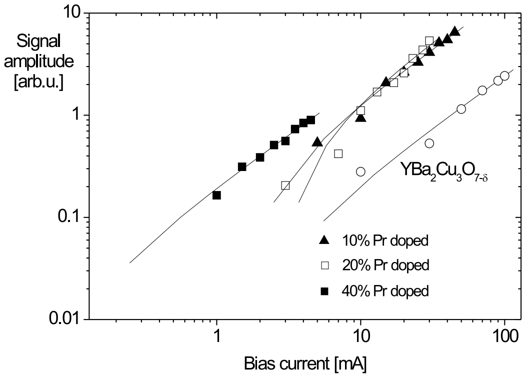

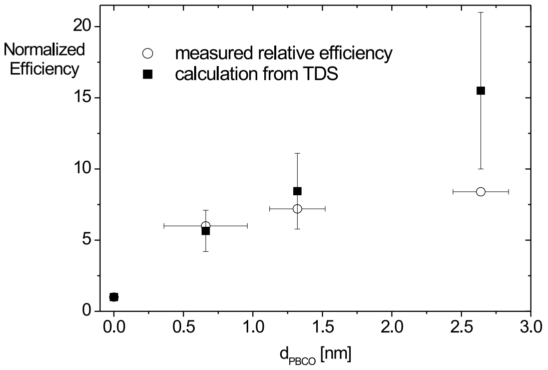

Fig. 5.13: The measured bias current dependence of the emitted THz-pulse amplitude for different PBCO layer thickness.

Fig. 5.14: The measured efficieny of the emitted THz radiation for different d$_{PBCO}$.

the dependence of the signal efficiency on the transmission of the multilayer structure in the THz frequency range are in good agreement to the experimental results in the case of a doping x less than x<0.3, see section 4.3.1. The transmission coefficient t$_1$ of the interface between the superconducting film and the substrate (LaAlO$_3$) can be calculated by equation 4.37. The ratio of the emitted electrical field in the case of the underdoped samples E$_1$ to the emitted electrical field E$_0$ in the case of pure YBCO is given by:

$$\frac{E_1}{E_0} = \frac{n_{s0} t_{11}}{n_{s1} t_{10}} e^{(\alpha_0 - \alpha_1) d}, \tag{5.4}$$

where n$_{s0,s1}$, t$_{10,11}$ and $\alpha_{0,1}$ are the supercarrier density, the transmission coefficient and the absorption coefficient of YBCO and the underdoped samples, respectively. The refractive index missmatch between the substrate LaAlO$_3$ and the MgO spherical lens leads to an additional loss by reflection, but this can be negleted in the ratio of the signals. In this equation it is assumed that the film thickness, the incindent laser power and bias current are the same for all samples. Furthermore the quantum efficiency of the optical Cooper pair breaking process is taken as constant, what explains the derivation of the calculated dependence from the experimental results at lower carrier density. The quantum efficiency of the Cooper pair breaking, i.e. the number of broken pairs by one photon due to the cascade effect, will depend on n$_s$. Nevertheless for low doping x, at temperatures far below T$_C$ and small excitation powers the effect should not be dominant. In the case of x=0.4 the derivation of the calculation from the observed data could be explained by this effect. Here the temperature is not so far from the critical value (T$_C$ = 48 K) and the carrier density is much lower ($n_s < 10^{19} cm^{-3}$). The results are discussed in more detail by the author in [Wald 02a].

6 Results of the PPT Experiments

The time-resolved THz spectroscopy technique, described in chapter 4, opens the possibility to measure the temporal evolution of electrical fields, which changes faster in time than one picosecond. In our experiments the emitters of such electromagnetic THz fields are dipole antennas of LT-GaAs or YBCO, characterized in the previous chapter.

By using the novel PPT technique a change in the emitted THz pulse due to an *additional* femtosecond optical excitation of these dipole emitters in the time domain is observed. The changes of the emitted THz signal are connected to the *nonequilibrium carrier dynamics* of the emitting devices on an time scale below 1 ps. In the case of the photoconductive devices the PPT experiment measures the magnitude of the local field in the emitter as function of the photogenerated carrier density directly, as supposed earlier by Jepsen *et al.* [Jeps 96] and Pedersen *et al.* [Pede 93]. A similar technique was previously used by the mentioned authors and others to characterize the carrier dynamics of THz emitters based on semi-insulating GaAs grown on Si [Pede 93a], GaAs and Si [Hu 95], [Jeps 96]. As mentioned in chapter 2 the semiconductor GaAs is an important material for high speed opto-electronic applications. The PPT technique is used to investigate for the first time small aperture antennas made of GaAs, which is grown at low temperatures, to observe the fast carrier dynamics of this material. LT-GaAs is capable of generating THz radiation and therefore it is an interesting canidate for this method. Other authors observed the excitation dynamics of LT-GaAs previously by a different THz spectroscopy technique [Segs 02]: a thin LT-GaAs layer is excited by a pump laser pulse and the amplitude of a THz pulse, transmitted through this excited layer, was measured in time domain. In difference to our PPT technique, the THz pulse in [Segs 02] was generated by a seperate THz emitter and not by the LT-GaAs sample itself. The reported results of these experiments are closely related to the results of our PPT technique. Nevertheless a clear advance of our PPT method compared to the method of [Segs 02] is the possibility to measure the field dependence of the excitation dynamics.

Previous PPT experiments on GaAs of Hu *et al.* [Hu 95] are focused on the very first events of carrier excitation. With a time resolution limited by the laser pulse width of only about 10 fs Hu *et al.* observed the instantaneous polarization in the electrical field of the coherent laser pulse and the initial ballistic carrier transport in the bias field. In our PPT experiments the temporal resolution is limited to about 150 fs and therefore the mentioned effects can not be measured. We concentrate us therefore on the carrier scattering, diffusion and trapping processes, which happen on a longer time scale. Other interesting experimental techniques to observe the excitation process on an ultrashort time scale are proposed by Sha *et al.* [Sha 92] (the *quantum confined Stark effect*) and Alexandrou *et al.* [Alex 94] (the *electro-optical sampling method*).

The results of the PPT experiments on the semiconducting material GaAs are analyzed by means of the *Drude-Lorentz model* and a rate equation model by Othonos *et al.*

[Otho 98], which can be fitted well by reasonable parameters of the carrier life time, carrier trapping time and carrier density, revealing that this novel method can be used to observe the carrier dynamic on a subpicosecond time scale.
As mentioned above, by using the PPT technique, photoconductive materials where already investigated by different authors. In our work we improved the system by usage of a cryostat and measure for the first time a very different group of materials, which is also capable of THz pulse emission at low temperatures: the high-T_C cuprates, namely YBCO. Transient electrical pulses with picosecond and subpicosecond duration, like described in the previos section for the materials YBCO and LT-GaAs, are observed in experiments using microbridges of various cuprate superconductors: $Y_xPr_{1-x}Ba_2Cu_3O_{7-\delta}$ [Wald 00], $Bi_2Sr_2CaCu_2O_{8+\delta}$ [Mura 01] and $Tl_2Ba_2CaCu_2O_{8+\delta}$ [Tomi 02], [Wald 02]. Therefore the THz radiation emission can be taken as a common property of these materials. The emitted pulses of the cuprates show very different and interessting properties and dependencies on the excitation conditions. For some materials the FT frequency components do not reach 1 THz ($Bi_2Sr_2CaCu_2O_{8+\delta}$) and in the case of $Tl_2Ba_2CaCu_2O_{8+\delta}$ the *c-axis* plasma resonance is observable [Tomi 02].
As we will show, by using the PPT technique it is possible to investigate the *nonequilibrium carrier dynamics* as well as the optical induced *flux-flow dynamics* of the cuprate high-T_C materials. The results of our PPT method (on LT-GaAs), previous optical *pump-and-probe* reflectivity measurements by our group and others and TDS [Bror 96] are used to analyze the data of the experiments on YBCO. The carrier dynamics of the high-T_C material is theoretically described by the *two-fluid model*, the RT- and 2T model, see chapter 3.

6.1 Results on LT-GaAs

In this section the results of the PPT experiment on LT-GaAs dipole antenna devices are summarized. The most important parameters, which influence the THz emission are the photon energy and the laser fluence of the excitation pulse, the bias voltage and the device temperature. All measurements on LT-GaAs are realized at room temperature and a photon energy of 1.55 eV. The laser fluence and the electrical field strength at the antenna (bias voltage) are varied systematically. Fig. 6.1 indicates as an example one result of the PPT experiment on LT-GaAs: it shows the amplitude of the emitted probe THz pulse as function of the pump-probe time delay between -3 and 50 ps.

This probe THz amplitude will be called PPT-signal from now. After the pump laser pulse arrived at t = 0, the signal amplitude decreases very fast. Than the amplitude recovers to a plateau with a value of about 80 percent of the PPT-signal before pumping. At t = 6.5 ps and t = 12 ps weak minima are visible, which are due to multiple reflections of the THz field at the backside of the GaAs wafer (0.5 mm thick, $\epsilon = 12$) of the emitter. If the pump and probe laser pulses are not polarized orthogonally, a coherent artifact apears in the signal, which is *not* the zero point of the time delay in our experiments, as described in section 4.4. The zero point of the pump-probe time delay is choosen here to be the point, when the PPT-signal starts to deviate from its equilibrium value. The Fourier transformation (FT) of the time resolved signal is shown in fig. 6.2. A clear *Drude-like* frequency behavior (fit is shown as solid line) is observed: a decrease

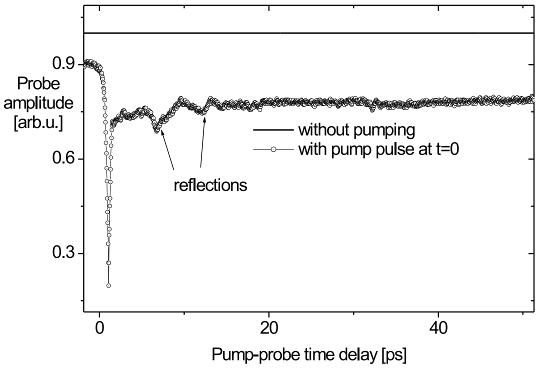

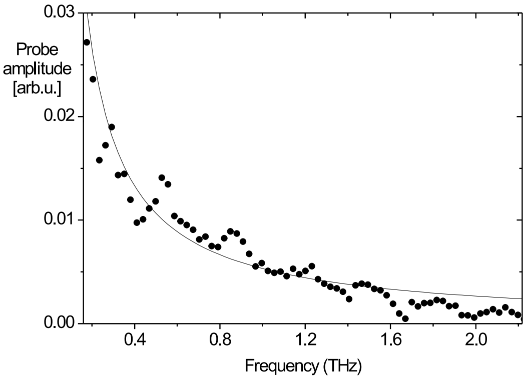

Fig. 6.1: Temporal evolution of the PPT-signal of the LT-GaAs dipole emitter after a pump excitation at t=0.

Fig. 6.2: FT of the PPT-signal shown in fig. 6.1.

of the THz amplitude in turn proportional to the frequency. This is an indicator of the frequency dependence of the carrier dynamics after optical excitation. Therefore in a first analysis of the PPT data a simple *Drude*-approximation is used for modeling the relationship between velocity and electrical field, like described in section 3.1.3. The additional modulation in the FT signal at a frequency of 310 GHz and higher harmonics are due to the multiple reflection at the GaAs wafer surface, like mentioned above.

The experimental observation (fig. 6.1) can be explained like described in section 3.1.3 and summarized as follows: after the pump laser pulse illuminated the antenna area, the free carrier density increases several orders, depending on the laser fluence. The free carriers (electrons and holes) are accelerated by the bias field, which leads to a polarization and a space charge field. This polarization screens the applied external bias field and reduces the local electrical field, which is therefore lower than the bias field and the emitted THz signal decreases. The carrier escape to the electrods at observation time can be neglected [Leite00]. The instantaneous polarization of the optical injected electron-hole pairs in the electrical field of the laser pulse occurs on a time scale of 10 fs, like disscused by Hu *et al.* [Hu 95], but because of the much higher laser fluence and the longer temporal pulse width used in our experiments the coherence of the carriers is erased very fast and the ballistic regime can not be observed.

The temporal evolution of the electron-hole polarization in the external bias field depends on the transient carrier density and on the drift velocity of the carriers. The carrier density depends on the optical generation term (pulse shape and width, laser fluence) in equation (3.2) and the free carrier lifetime. The carrier velocity depends on the local electrical field strength and the carrier mobility.

In the fig. 6.1 additionally to the fast reduction and recover of the PPT signal near t=0 a second component is observed: a long time reduction of the THz amplitude after the excitation to about 80 percent, which continues until the end of the observation. This effect increases with higher laser pump power and does not depend on the bias

voltage. It could be caused by diffusion of hot carriers from the LT-GaAs layer into the bulk GaAs with longer free carrier lifetime and hot carriers, which are optically injected in the wafer itself [Engh 93]. In the semi-insulating GaAs wafer on which the LT-GaAs layer is grown band-to-band or Auger recombination can occur with a characteristic time constant of about 100 ps [Tono 02]. Experiments on GaAs, which is not low-temperature grown, shows only this long time PPT signal reduction [Jeps 96]. Therefore for higher laser fluences a charging effect of the GaAs substrate reduces the transmission of the probe signal on such a long time scale, leading to the observed effects.
Recently Stellmacher *et al.* [Stel 00] pointed out that the acceptor band due to the Ga vacancies in LT-GaAs could play an important role in the carrier dynamics and trapping processes in such acceptors could lead to a slow component in the carrier relaxation [Stel 00]. If the pump laser fluence is increased the general probe amplitude even at time delays t < 0 decreases compared to the value without pumping, like indicated in fig. 6.1 by the solid line without points. Here it must be taken into account, that the laser repetition rate is about 82 MHz and for processes, which take longer than the duration between two laser (pump-)pulses an averageing occurs and the lock-in technique can not be used. Therefore such processes can not be studied using a system with pulses of such a fast repetition. This effect of THz field reduction on a long time scale ($>$ 12 ns) is caused by heating and will be discussed in more detail in section 6.1.2.

6.1.1 Bias Voltage Dependence

The PPT signal as function of the pump-probe time delay for different bias voltages between 1 and 20 V is indicated in fig. 6.3 and fig. 6.4. The electrical bias field strength $\vec{\mathcal{E}}_{bias}$, generated by the potential difference over the gap between the electrodes, is very high, because of the small gap size and the high resistivity of GaAs (a bias voltage of 1 V leads to a field strength of about 2 $kVcm^{-1}$). The general THz radiation amplitude increases linear with higher bias voltage like mentioned in section 5.2.1.

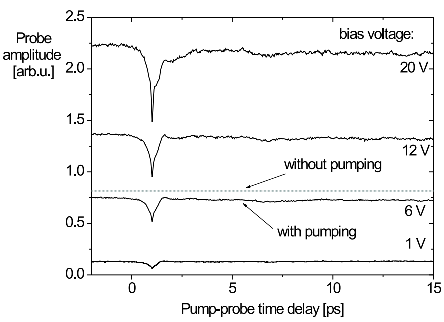

Fig. 6.3: Probe amplitude as function of the pump-probe time delay for a fixed pump power of 2 mW and different bias voltages between 1 V and 20 V.

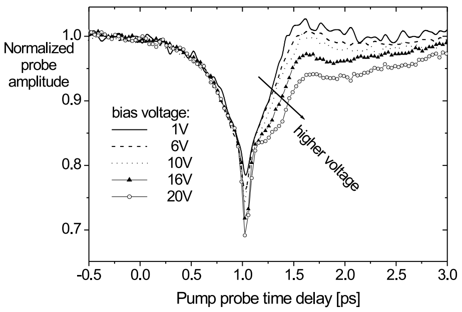

Fig. 6.4: Normalized probe amplitude of the data shown in fig. 6.3, focused on the delay times near t = 0.

The fast decrease of the PPT-signal after optical excitation takes about 1 ps, what means that the screening effect continues to develop for about 500 fs after the optical pulse vanished. In fig. 6.4 clearly a non-exponentially decay behavior can be observed. This implies that several processes of carrier trapping, scattering and recombination are involved in the recovering of the PPT signal [Tono 02]. Until t = 1.1 ps, while the PPT-signal is decreasing, the temporal evolution of the signal is equal for all bias voltages and does not depend on the electrical field strength and therefore the reduction of the PPT amplitude is field independent. That means electron-electron and electron-phonon scattering occurs mainly within the first 500 fs. This scattering erases first the coherence of the carrier motion and destroys the instantaneous polarization P_{inst}, which is generated by the electrical field of the coherent laser photons. The recover of the probe amplitude at t > 1.1 ps depends on the bias field strength, see fig. 6.4. This process slows down substancially at higher electrical fields above 25 $kVcm^{-1}$. This value is very close to the value of the bias saturation of the PPT amplitude, see fig. 6.5. With increasing the bias voltage, or equal the electrical field strength, the minima at t = 1 ps do not shift in time. The minimum of the PPT signal increases with higher voltage (fig. 6.5) and three small peaks at 3 V, 6 V and 14 V are observed. At bias voltages above a treshold of 14 V (28 $kVcm^{-1}$) the PPT-signal minima saturates at around 75 % of the signal amplitude before pumping. The bias voltage dependence of the THz signal (section 5.2.1) shows *no* saturation effect.

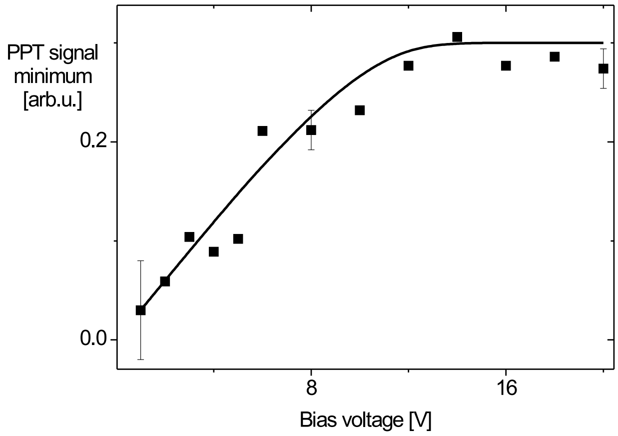

Fig. 6.5: Dependence of the minimum in the PPT signal on the bias voltage. As solid line a fit to a saturation effect dominated by scattering on the ionized donor centers is shown.

This effect of PPT signal saturation at high fields can be explained by the saturation effect of the *drift velocity* at higher fields, which is observed in all semiconducting materials. The *drift velocity* saturation takes place at electric field strengths of about 2 to 10 $kVcm^{-1}$, what is comparable to our results. This saturation is generally explained by LO-phonon emission which increases with higher field strength [Otho 98]. Nevertheless in the case of LT-GaAs the ionized donor centers have a significant influence on the carrier scattering, too. The scattering of electrons by the ionized donor centers is due to Coulomb interaction and the scattering rate depends on the velocity like [Ibac 99]:

$$\Gamma \sim |\vec{v}|^4. \tag{6.1}$$

Using such a dependence the experimental data can be fitted by calculating the deviation from the linear (Ohmic law) behavior, see fig 6.5 (solid line).
At t = 1.6 ps a small maximum in the probe amplitude is observed (fig. 6.3 and 6.4). This maximum is not observed in experiments on GaAs, which is not low-temperature grown [Jeps 96]. It appears at all bias voltages and does only shift slightly with higher bias voltages, what should be caused by changes in the relaxation time. This maximum can be understood by the carrier trapping in the midgap states of LT-GaAs and/or velocity overshoot effects and will be analyzed in a later section.

6.1.2 Pump Power Dependence

The general PPT amplitude without pumping, indicated as a grey line in fig. 6.3, decreases a constant offset value for all time delays if the sample is pumped, like mentioned above in section 6.1. This decrease of the PPT signal depends on the pump power, like shown in fig. 6.6, but does not depend on the bias voltage. This effect is caused by an average heating of the antenna area (with duration longer than the laser repetition time) due to the illuminated laser fluence, which changes the gap energy, the resistivity and the dielectric constant and generates this offset in the PPT signal. With higher temperature the gap energy decreases and the number of thermally excited electrons increases. The dark conductivity of the sample rises and that leads to a reduction of the THz efficiency. Temperature changes can therefore influence the excitation substantially. The temperature increase of the emitting area due to the laser illumination can be calculated by using the spreading resistance model [Verg 97]. The thermal conductance

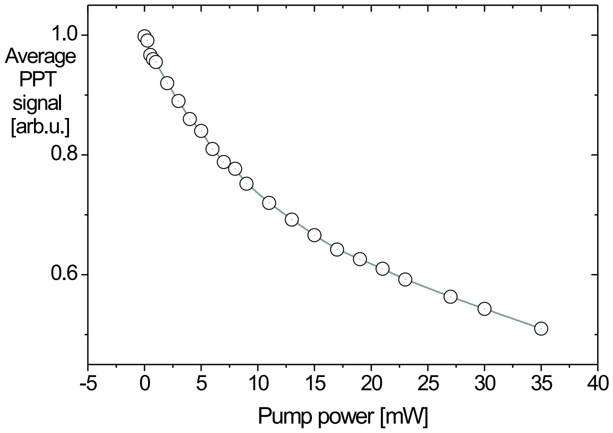

Fig. 6.6: Average PPT signal amplitude in dependence on the pump power (heating effect). The solid line is a guide to the eye.

G is given by the assumption that the active area is a hot hemisphere that emit heat by conduction into the semi-infinite substrate with thermal conductivity κ:

$$G = \kappa\sqrt{2\pi A}, \tag{6.2}$$

where $\kappa = 0.46\ Wcm^{-1}K^{-1}$ is the thermal conductivity of GaAs at T = 290 K. The emitting area A of a diameter of 5 μm (gap size) results in G = $5\times10^{-4}WK^{-1}$, a very similar result as measured by Verghese *et al.* [Verg 97]. Assuming a laser power of P_{laser} = 35 mW the calculated temperature rise is about: ΔT $\approx$ 70 K. The PPT signal amplitude as a function of the pump-probe time delay at different laser powers is indicated in fig. 6.7. The optically injected free carrier density is calculated from the pump laser fluence by assuming linear photon absorption, following equation 3.3. The total density of states for electrons in the conduction band is estimated to be $7\times10^{18}cm^{-3}$ and the effective density of states to be $4\times10^{17}cm^{-3}$ [Benn 90]. Taken the band shrinkage into account it follows a value of about $8\times10^{18}cm^{-3}$ for the density of states. In this PPT experiment the laser pump power is varied between 1 mW and 35 mW, while the probe power (1 mW) and bias voltage (7 V) are kept constant. Therefore the optical injected free carrier density is about $1 \times 10^{18}cm^{-3}$ to $3.5 \times 10^{19}cm^{-3}$. The carrier acceleration may increase the capacity for the carrier injection and therefore the fastest PPT signal recover process vanishes at a smaller carrier density than explained by the band filling model [Tono 02]. At such high free carrier densities scattering works very efficient and the *Drude model* is assumed to be appropriate to describe the dynamics of this early stage after excitation [Jeps 96].

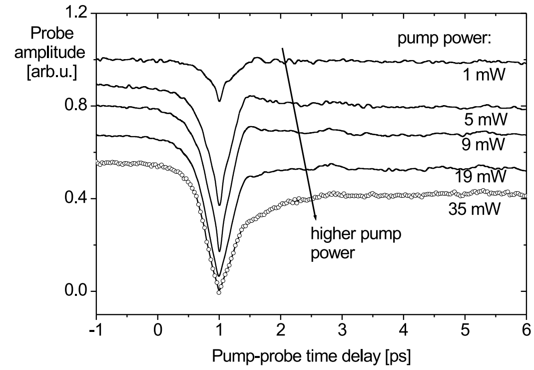

Fig. 6.7: The PPT signal as function of pump-probe time delay at different pump powers, between 1 and 35 mW.

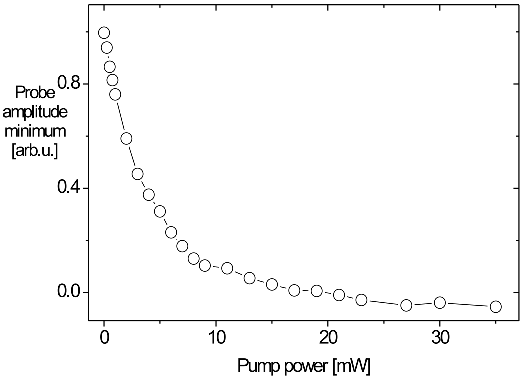

Fig. 6.8: Dependence of the PPT amplitude minimum on the pump power.

The probe amplitude minimum at t = 1 ps does not shift in time with changing pump power. The minimum of the PPT amplitude depends on the laser power, like shown in fig. 6.8. For laser pump powers above 20 mW ($n_{free} \approx 5 \times 10^{18}cm^{-3}$) the probe THz sinal is completely suppressed. We recognize, that this is the same laser power at which

the emitted THz pulse amplitude saturates as well (section 5.2.2). It was suggested that this THz pulse saturation effect can be explained by bias field screening [Darr 92]. This is now proofed by our PPT experiment, because as mentioned before in chapter 4, the PPT signal itself is produced by the bias field screening.
The dynamics of the PPT signal decay varies with the carrier density and there is evidence of trap saturation by trap filling at carrier density above $5 \times 10^{18} cm^{-3}$, what is in a good aggreement with usual trapping state densities in this material. A slowing down of the carrier trapping with increasing carrier density was reported previously [Sosn 97]. For higher carrier densities not the trapping time governs the free carrier lifetime, but the emptying of the trap states and the carrier recombination. The small maximum in the probe amplitude at t = 1.6 ps, mentioned in the previous section, is only observed at pump powers below 20 mW and vanishes above. This can be explained by a filling of the trapping states by excited electrons at a density of about $5 \times 10^{18} cm^{-3}$. Another possibility to explain the small maxima is the velocity overshoot, which can occur while the local field strength increases with the decreasing space charge field and at the same time electrons are scattered to the X and L valleys. If the velocity overshoot does not play a role, the increase in the carrier relaxation time with higher pump power could be caused by filling of the mid-gap trapping states, which are supposed to lead to the rapid carrier relaxation in LT-GaAs [Otho 98]. In this case the filled trapped states act as a bootleneck for the carrier relaxation and a suppression of the THz signal occurs. The minima in the PPT amplitude decreases for low pump powers ($< 5mW$) nearly linear with the power. For power above 5 mW the minima deviates from the linear dependence and becomes zero for $P_{pump} > 20mW (n \approx 5 \times 10^{18} cm^{-3})$ at the same laser power, when the small maximum at t = 1.6 ps vanishes. Therefore both effects could be connected.

6.1.3 Model Description

Some authors has previously used the *Drude-Lorentz model* to describe the carrier dynamics in a photoconductive THz antenna, without screening effects [Beni 93] and with screening included [Jeps 96]. This model is in detail described in section 3.1.3. Because of the 10 times lower mobility of the holes, the small contribution to the polarization resulting from hole motion is neglected in this model [Tono 02].

At first a simple *one-level* carrier excitation and relaxation following equation 3.2 of section 3.1 is assumed. More details of the processes of the relaxation dynamics of LT-GaAs, which is modified because of the high number of trapping states, will be included in the calculations in the next step.
In this first simple model the excitation from the midgap states, the two photon absorption and the carrier diffusion are not taken into account. The free carrier lifetime of LT-GaAs is dominated by the fast trapping at the ionized As precipitates. Than the carrier dynamics can be described by solving the coupled differential equations 3.10 - 3.13. A result of the fit to the observed PPT data, which uses this model, is shown in fig. 6.9 for a bias voltage of 10 V and a laser pump power of 2 mW. The fixed parameters of the model are therefore the bias field $\vec{\mathcal{E}}_{bias} = 20\ kVcm^{-1}$, the laser pulse width l_{laser} = 100 fs, the effective mass m^* =$0.07m_e$, the geometrical factor $\eta = 3$ and the dielectric constant $\epsilon = 12$. The parameters of the fit based on the *Drude-Lorentz model*, which is indicated as solid line in the fig. 6.9, are the carrier momentum relaxation time τ_{rel} =

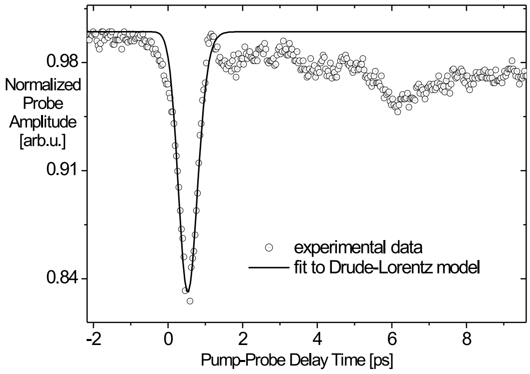

Fig. 6.9: PPT signal as function of the pump-probe time delay for a pump power of 2 mW and a bias voltages of 10 V. As solid line a fit following the Drude-Lorentz model is shown.

30 fs, the carrier recombination time τ_{rec} = 100 fs and the injected carrier density n_{free} = $0.8\times10^{18} cm^{-3}$. In literature the carrier momentum relaxation time is reported to be about some ten femtoseconds [Hu 95], [Otho 98] and $\leq$ 50 fs[Jeps 96], what is very close to the fitted value of the PPT experiment. The effective carrier trapping time in LT-GaAs depends strongly on the growing conditions of the material and is reported to be as fast as about 200 fs [McIn 96] for probe photon energies well above the band gap energy. Nevertheless the dynamics of the motion of the hot electrons in the conduction band will influence the results of this experiments and therefore results of experiments with probe photon energy close to the band gap are more reliable [Segs 02]. Such measurements yielded values of about 300 to 500 fs [Gren 97]. The short momentum relaxation time is a sign that the carrier-carrier scattering works efficiently to erase the coherence of the carrier motion after excitation due to the coherent laser pulse photons. Therefore the dephasing of the carrier motion occurs very fast. The thermal equilibrium between the carriers is reached within some ten femtoseconds. This is caused by the high injected carrier density of the experiment and therefore the data of the PPT experiment can be described well by the *Drude-Lorentz model* [Jeps 96]. Nevertheless the long time effect, which is observed at higher pump laser powers and the small peaks at time delays of about t = 1.6 ps, which are observed at not to high pump laser powers, can not be explained by this simple model.

The fig. 6.10 shows a fit following the *Drude model* with including the relaxation from the hot carriers and the relaxation of the carriers from the bottom of the conduction band to the midgap states. The modification of the carrier dynamics because of the excistence of midgap states is described in detail in section 3.1.1 and three differential equations (equation (3.4), (3.5) and (3.6)) were suggested by Othonos *et al.* to calculate the carrier recombination- and trapping times. Two photon absorption from the valence band and direct absorption from the localized states in the energy gap are included in this model. By using these rate equations and including the resulting free carrier density

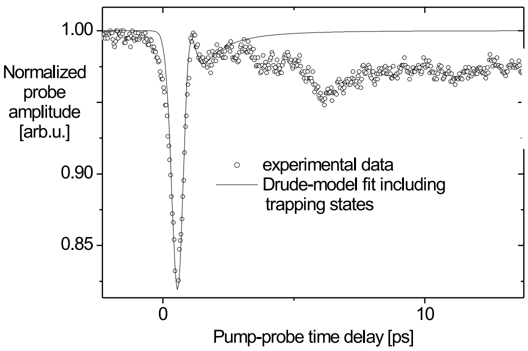

Fig. 6.10: PPT amplitude as function of the pump-probe time delay. A fit following the Drude-Lorentz model including the influence of trapping states is shown.

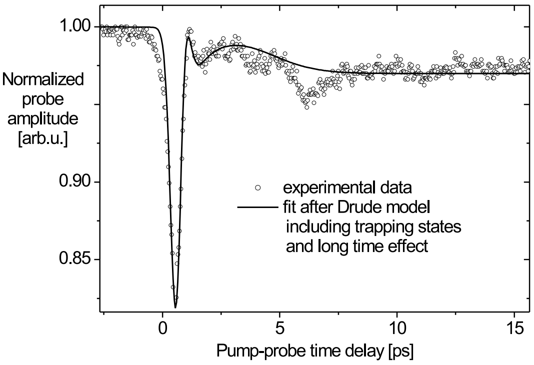

Fig. 6.11: Probe amplitude as function of the pump-probe time delay. A fit following the Drude-Lorentz model including the influence of trapping states and the long time effect is shown.

in the calculation of the temporal evolution of the polarization the model is modified. The parameters of the fit, which is shown in fig. 6.12 are the following: a ratio of the absorption constants $\alpha/\alpha_T/\beta$=0.07/0.5/0.001 (valence state/trapping state/two photon absorption) is obtained. Because the fit based on the normalized data only a ratio of the absorption constants can be defined. To fit the measured normalized data properly a multiplication factor of 1×10^9 has to be introduced in the carrier generation term I_0, which has a Gaussian shape. Because this factor influence the absolute values of α, α_T and β only their ratio can be estimated. The characteristic relaxation time constants of the fit are a momentum relaxation time τ_{rel} = 65 fs, a carrier trapping time of the hot carriers by τ_{trap1} = 250 fs and a carrier trapping time of the electrons at the bottom of the conduction band τ_{trap2} = 2.2 ps. Trapping times of LT-GaAs are reported to be τ_{trap1} = 0.6 ps for 250°C grown LT-GaAs and τ_{trap1} = 0.31 ps for LT-GaAs grown at 300 °C, τ_{trap2} = 3.0 ps for 250°C grown LT-GaAs and τ_{trap1} = 1.4 ps for LT-GaAs grown at 300 °C, respectively [Otho 98]. These reported results were calculated by fitting the used rate equations to all optical time-resolved transmission measurements.

It is possible, nevertheless, to explain the small peaks in the PPT signal at t = 1.6 ps also by the velocity overshoot effect, which was mentioned earlier. With the change in the polarization the local field strength changes. At low electrical fields the conductivity σ depends linear on the mobility μ and the current is proportional to the electrical field $\vec{\mathcal{E}}$. At field strength above 3 $kVcm^{-1}$ the drift velocity $\vec{v}_d$ is no longer proportional to $\vec{\mathcal{E}}_{bias}$ and saturates, like already mentioned in the discussion of the bias dependence. This is schematically shown in the figs. 6.12 and 6.13. In GaAs a maximum of the drift velocity as function of $\vec{\mathcal{E}}_{bias}$ occurs, because of scattering of electrons to the X and L valleys, where the electron mobility is lower. Such scattering takes place if the energy of the electrons due to the field strength is sufficient to reach the neighbour minima. With beginning of the scattering to the X and L minima, more and more electrons

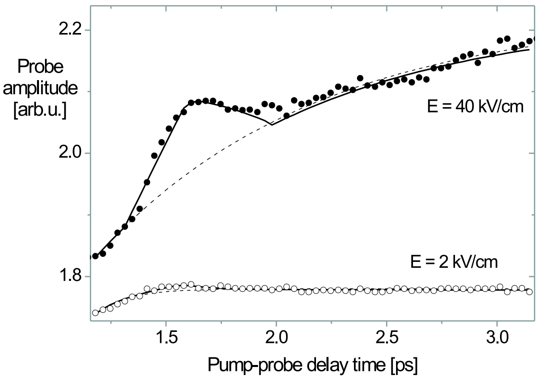

Fig. 6.12: Probe amplitude as function of the pump-probe time delay at two different bias voltages: 1 V and 20 V. The solid line indicates fits based on the velocity overshoot.

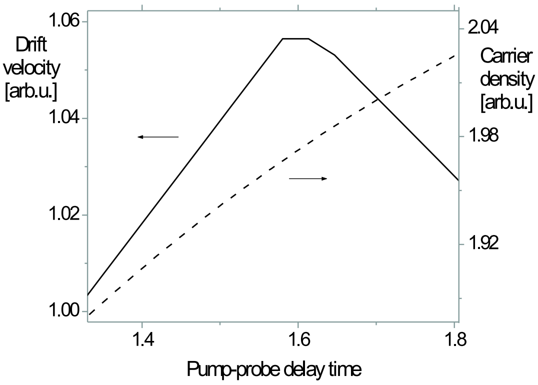

Fig. 6.13: Schematic picture of the time scale of the evaluation of the drift velocity (left, solid line) and the free carrier density (right, dashed line).

exhibit larger effective masses and $\vec{v}_d$ decreases. This could cause the observed increase in the probe amplitude recovering time, because of the longer free carrier lifetime in the neighbour valleys and the lower mobility which reduces the conductivity.
Simply said: after the excitation the sreening of the bias field leads to the described reduction in the *local* field $\vec{\mathcal{E}}_{loc}$. When the local field recovers, it changes over a range where the maximum of the drift velocity in dependence on the field strength is situated. Therefore the velocity first increases and then decreases with higher fields. If we assume a simple linear dependence of the drift velocity on the time delay, like indicated in fig. 6.13, the small maximum can be fitted well by an exponential carrier relaxation. The vanishing of the effect at small bias voltages (fig. 6.12) and at high carrier densities supports this model. Instantaniously after excitation the local field is reduced and electron-intervalley-scattering takes place rapidly as the electrons are ballistically accelerated by the field. With a higher temporal resolution then we were able to use, the velocity overshoot can be observed in this ballistic regime, too [Hu 95].

6.1.4 Discussion of the Results

Despite the fact that by using the rate equations proposed by Othonos *et al.* [Otho 98] the data of the PPT experiment can be fitted very well, it is doubtfully that for the first 1 ps instantaniously after the optical excitation this theory properly describes the physical processes, because many body and hot carrier effects will play a key role in the early stage of carrier relaxation [Segs 02]. For instance the Electron-LO-phonon scattering time is measured to be 170 fs [Kash 85] and by using only the PPT signal the influences of the mobility change and the influences of the carrier scattering and trapping can not be seperated. Another important point is, that because at time delays before the coher-

ent artifact (observed at t = 1 ps), the pump laser THz signal may be influenced by the probe laser beam, which arrives *before* it and which modulates the pump THz signal, as mentioned earlier in section 4.4. This could influence our results at time delay t< 1 ps. Therefore it is assumed to get more reliable results of the carrier trapping time by using a simply exponential fit, but only to data of pump-probe time delays of 1 ps after the excitation, because at this time delays the carrier trapping should contribute mainly to the PPT signal, while the drift velocity can be assumed to be roughly constant on one side, and on the other side the pump THz signal definitely not influence the PPT signal. If we do not assume the velocity overshoot to take place, then only for not to high bias voltages the PPT signal can be fitted well by an exponential decay. With higher bias voltages the behavior changes to a clear non-exponential law. This could be explained in the Anderson localization model by an energetically shift of the mobility edges to deeper Urbach tail states with higher electrical fields. Due to this shift Urbach tail states start to contribute to the THz radiation, which do not contribute to it at lower fields. This effect could be caused by effects of the band bending near the Schottky contacts of the metal electrodes. The carrier trapping could be substantially reduced, because the band bending leads to an effective vanishing of localized states in the gap, if higher bands can overlapp in E-k-space with the midgap states.
But the explanation of the non-exponential behavior by the existence of a velocity overshoot, remains a tempting possibility. If we in that case assume the exponential decay of the carrier trapping a dependence of the carrier trapping on the bias voltage and the laser pump power as indicated in the fig. 6.14 and 6.15 follows.

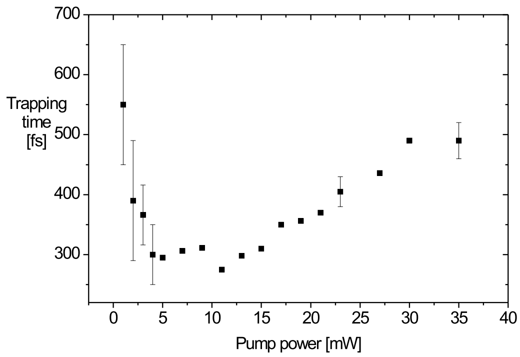

Fig. 6.14: Carrier trapping time as function of the pump power between 1 mW and 35 mW.

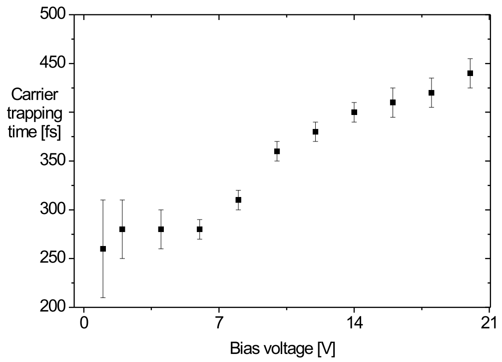

Fig. 6.15: Carrier trapping time as function of the bias voltage between 1 V and 20 V.

The *Drude-Lorentz* model can be used to explain the carrier dynamics in the photoconductive THz emitter, because the carrier density is high enough: 10^{18}-$10^{19} cm^{-3}$ and the scattering leads very fast to a thermal equilibrium in the material. At thermal equilibrium the carrier density of states can be described by the *Fermi-Boltzman* distribution function, i.e. the carrier dynamics follows the *Drude-Lorentz* model. Because of the very fast scattering the dephasing time of the coherence of the carriers, which are coherent accelerated in the laser field, is very short. The random scattering erases the coherence effectively. As mentioned above Deep donor centers of As percipitates play a key role in the carrier relaxation. At higher bias voltages scattering on the ionized donor center as well as LO phonon emission leads to saturation of the drift velocity. Higher pump powers and injected carrier densities lead to trap state saturation and a bottleneck effect. The details of the carrier relaxation based on the experiments of this work is published together with the author [Tono 02]. The behavior at pump powers between 5 and 15 mW could be explained by a change in the quantum efficiency of the optical exciation which depends on laser fluence or the mobility saturation effect of the GaAs emitter. At high bias fields the main contribution to the THz field gives the drift current $\vec{j}(t)$, but at very low bias fields the χ^2 process (resulting in a displacement current) may also play an important role, if the exciation energy is near the band gap of the semiconductor [Jeps 96]. To exclude the bulk χ^2 effect [Zhan 92], [Gree 92] an investigation of the dependence of the PPT signal on the crystall orientation would be nessecary. In the case of GaAs (not low-temperature grown) Hu *et al.* repeat their PPT measurements while rotating the azimuth angle of the sample. They could not find an orientation dependence and concluded that the bulk χ^2 effect is negligible. Therefore in our LT-GaAs experiments this effect should be negligible, too.

The temperature dependence of the PPT signal was not investigated here. Nevertheless previously time-domain photoreflectance experiments indicated a negligible dependence of the photo-excited carrier lifetime on temperature [Wang 93].

6.2 Results of PPT on YBCO

After using the PPT-method to investigate the ultrafast carrier dynamics of LT-GaAs, the system is putted forward to measurements at low temperatures by extending the set-up with an optical He-cryostat. That makes it possible to operate the emitter of the THz pulses at temperatures between 17 K and 300 K. In the case of the cuprate superconductors a cooling below T_C is neccesary, which is about 90 K.

The process of THz emission of YBCO, as reported previously in chapter 5, contains two different physical processes of the carrier dynamics, which are investigated by the PPT technique:

- the ultrafast generation and relaxation of hot quasiparticles and
- the recombination of quasiparticle to Cooper pairs.

The following sections concentrate on the results of the PPT techique on superconducting YBCO thin films. The emission process of superconducting microbridges differs fundamentally from the emission of photoconductive switches, because the device is not voltage but current biased. Therefore the boundary conditions are completely different. While at the LT-GaAs samples an external bias field accelerates the carriers and leads to a polarization, in the case of YBCO the energy is stored in the kinetic energy of the Cooper pairs in coherent motion. The pump laser pulse excites the sample and leads to a non-equilibrium hot quasiparticle distribution and to a reduction of the Cooper pair density. The carrier polarization in the case LT-GaAs screens the bias voltage thus the local field is reduced leading to PPT signal, what is measured. In the case of the superconductor there exist *no* local field before the laser pulse illuminates the sample. The device is biased by a dc current, which is produced either by an external source or trapped flux.

6.2.1 Time Resolved Probe Amplitude

Like in the experiments on LT-GaAs the detector trigger time delay is fixed exactly at the point in time, when the maximum amplitude of the probe THz pulse is measured. Again only the probe laser pulse is chopped at 2 kHz and can be detected. This leads to the same problem as before: if the probe pulse arrives *before* the pump laser pulse: the pump THz pulse could be influenced by the probe laser, chopped at 2 kHz and detected by the lockin amplifier, therefore the probe laser power must be much smaller than the pump power. By changing of the time delay between the pump laser pulse and the probe laser pulse and leaving the detector trigger time constant, the time resolved evaluation of the probe THz signal amplitude (PPT signal) as a function of the time delay between pump and probe is measured. The PPT signal is observed at time delays, which vary from -30 ps (before pumping) to 120 ps (after pumping), limited by the lenght of the translation stage. The measured probe pulse THz amplitude (PPT signal) as function of the pump-probe time delay for a pump power of 20 mW, a probe power of 3 mW and a bias current of 300 mA at T = 17 K is shown in fig. 6.16. The change of the THz signal under this excitation conditions occurs mainly on a time scale of about 20 ps, much longer than in the case of the PPT signal of LT-GaAs. The zero point of the pump-probe time delay, as indicated in fig. 6.16, is choosen where the PPT signal deviates from zero more than the noise limit of 1 μV at the amplifier.

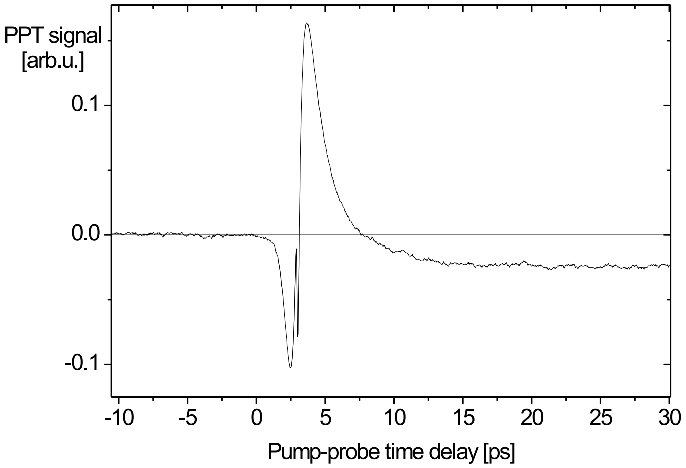

Fig. 6.16: Temporal evolution of the PPT signal of YBCO at a pump power of P_{pump}=20 mW, a probe power of P_{probe} = 3 mW, a bias current of I_{bias} = 300 mA and a temperature of T = 17 K.

To analyze the PPT signal of YBCO, the different measurement-regimes, introduced in section 4.4 with the figs. 4.10 to 4.14, are used. At negative time delays t < 0 the PPT signal is not influenced by the pump laser/pump THz, see fig. 4.10. After t = 0 the PPT signal amplitude decreases. This change in the signal exhibits a characteristic decay time of about 1 ps and a minimum is observed at t = 2.5 ps and it is located *before* the coherent artifact. That means the time regime of fig. 6.17 is valid, the PPT signal is influenced by the THz pump pulse. The effect can be explained as follows: the electrical field of the probe laser pulse accelerates the *normal* carriers inside the superconductor and produces a polarization current additionally to the bias current and this current leads to a reduction of the pump THz pulse. The reduction of the pump THz pulse can be observed because the probe laser is chopped and the induced changes therefore visible. In the case of LT-GaAs this does not play a rule because of the low equilibrium carrier density. Because the observed changes are due to the pump THz pulse, it has to be taken care that the pump-probe time delay has to be inversed to analize these data. This effect should increase at higher temperatures, because of the temperature dependence of the normal carrier fraction. At a time delay of about t = 3 ps the coherent artifact of pump and probe laser pulse is measured (see fig. 6.18, dashed line, or the schematic picture at fig. 4.13, chapter 4). This coherent artifact can be suppressed completely by the usage of orthogonally polarized laser beams. After the coherent artifact, at t > 3 ps, the PPT signal is solely influenced by the pump laser. Here the pump THz is not influenced by the probe laser pulse, which follows *after* the pump laser pulse. A fast increase of the PPT signal is observed, which leads to a maximum at about t = 3.5 to 3.7 ps, followed by a relaxation to a constant level. The equilibrium is reached at about t = 15 ps. This temporal evaluation of the PPT signal can be explained by laser induced quasiparticle excitation and Cooper pair breaking and subsequent relaxation of the quasiparticles by LO phonon emission with the recombination of unpaired holes to Cooper pairs. This processes lead to a temporal increase in the output coupling of the probe THz pulse,

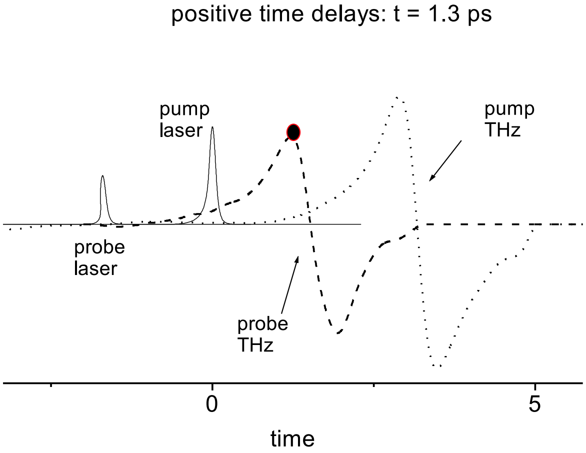

Fig. 6.17: Schematic picture of the position of the PPT signal at 0 < t < 3 ps compared to the pump laser and THz pulse.

which can be observed. Because this effect is connected to Cooper pair breaking, it should decrease at higher temperatures and vanish near T_C.

The equilibrium level of the PPT signal, after t = 15 ps, is well below the PPT amplitude before pumping, see fig. 6.16. This reduction of the equilibrium level depends on the change in the *number of flux lines*, which are trapped in the excitation area.

The evaluation of the measured probe amplitude after pumping depends on the concrete excitation condictions (pump power, bias current, temperature). This is described in the following sections.

The FT of the observed PPT signal of fig. 6.16 and for a lower excitation power and bias current (at P_{pump} = 17 mW, P_{probe} =1 mW, I_{bias} = 100 mA and T = 17 K) is indicated in fig. 6.19 and 6.20.

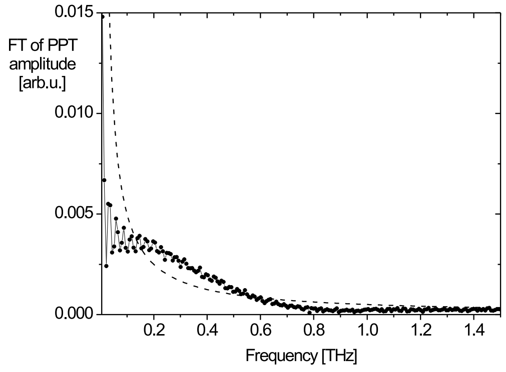

Fig. 6.18: FT of time resolved data shown in fig. 6.16.

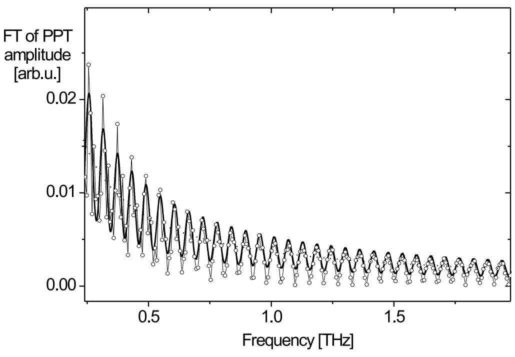

Fig. 6.19: FT of the PPT signal at lower excitation. The fit (thick solid line) is calculated by a typical resonance structure with an additional 1/f behavior (dotted line).

The FTs show a frequency dependence with strong oscillations due to multiple reflection and interference in the substrate material. The oscillating feature is visible in both FT, but more pronounced at weaker excitation. By fitting the curve to a resoncance behavior $f(\omega) = \frac{1}{\omega} sin(\frac{\omega}{\omega_0})$, as shown in the figure 6.20 with the thick solid line, a resonance frequency of $2\pi\omega_0$ = 58 GHz can be determined. With the refractive index of MgO ($n_{MgO} = 3.1$) the $\lambda/2$ value of this resonance is 0.8 mm, what corresponds to the substrate thickness. Because this resonance frequency does not depend on the excitation conditions, the superconducting film itself can not be the reason for it (because of e.g. the strong temperature depependence of $\bar{n}_{YBCO}$).

This observed behavior of the PPT amplitude of YBCO after optical excitation is different compared to the results of the measurements on the LT-GaAs dipole antenna at room temperature. The FT of fig 6.19 clearly does not show a *Drude like* frequency behavior, but the FT of the PPT signal at weaker excitation can well be described by the *Drude like* frequency behavior.

6.2.2 Pump-Power Dependence

The emitted THz pulse amplitude of a YBCO emitter depends linear on the excitation laser fluence, like mentioned in section 5.2.2, fig. 5.9. This linear dependence is explained by the increase in the number of optical broken pairs with increase in the laser fluence, see equations 4.26 and 4.27.

To obtain the dependence of the PPT signal on the pump laser fluence, the pump power P_{pump} is varied while the bias current (I_{bias} = 300 mA), the probe power (P_{probe} = 3 mW) and the device temperature (T = 17 K) are kept constant. Fig 6.21 shows the PPT signal as function of the pump-probe time delay t at different pump powers 1..50 mW. The PPT signal amplitude at different measurements before t = 0 in fig. 6.21 remains at a nearly constant value (about 0.15 arb.u.), because the probe THz pulse is generated under the same excitation conditions. Nevertheless it is shifted slighltly up and down because of changes in the *flux trapped state* of the sample, if the laser pump power is below 30 mW. If the laser power is increased further, the probe signal before t = 0 decreases significantly and shows a linear dependence on t. This effect can be explained by the influence of the probe laser pulse on the pump THz pulse plus pump induced changes in the *flux density*, which causes a drift that can be detected. Here the probe THz signal itself is still at time delays *before* the pump laser and therefore it can not be influenced by it.

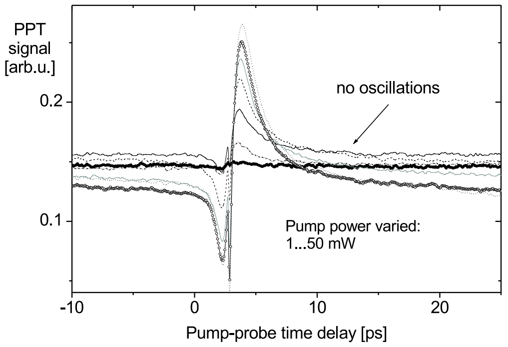

Fig. 6.20: Temporal evolution of the PPT signal of the YBCO at different pump powers.

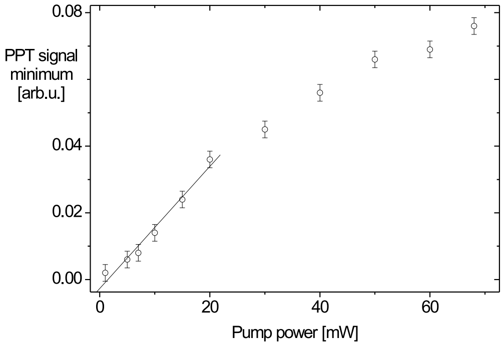

Fig. 6.21: Pump power dependence of the PPT signal minimum. As solid line a linear fit is shown.

Fig. 6.22 shows the dependence of the minimum in the PPT signal at t = 2.2 ps on the pump power until P_{pump} = 70 mW. Up to pump powers of about 20 mW a linear dependece is observed. Above 30 mW the PPT minimum deviats from the linear behavior. The linear dependence can be explained simply by the linear power dependence of the THz pulse amplitude (here the THz pump pulse). At higher pump powers flux dissipation sets in, explaining the deviations.

Fig. 6.23 indicates the pump power dependence of the PPT signal maximum at t = 3.5 to 3.7 ps. A more clear linear dependence on the pump laser fluence up to powers of about 30 mW is observed. If the pump power is increased further the PPT signal maximum decreases. We ressume: though a linear dependence of both peaks of the

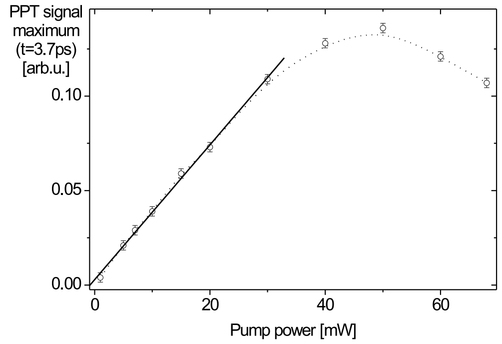

Fig. 6.22: Pump power dependence of the PPT signal maximum at t = 3.5 to 3.7 ps. As solid line a linear fit is shown.

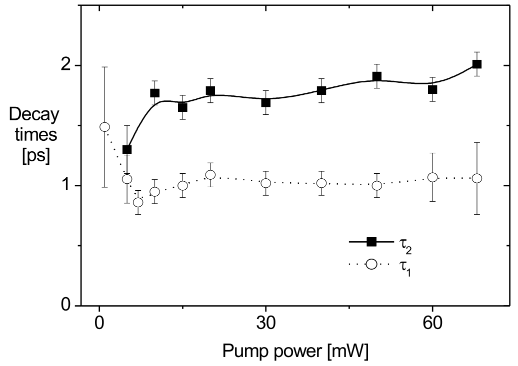

Fig. 6.23: Decay times of the peaks of the PPT signal: minimum decay time is τ_1 and maximum decay time is τ_2.

PPT signal (minimum and maximum) at low pump powers is observed, at higher pump powers the dependencies are different. The mentioned shift in the general probe THz signal at t = 0 occurs at a time scale longer than 12 ns. That means an average effect as described also in the case of LT-GaAs occurs. Nevertheless here this effect can not be due to heating, because with higher temperature the THz signal would be nearly uneffected ($T << T_C$) or increase ($T \approx T_C$) (section 5.2.3). As calculated in chapter 2 the optical induced temperature change is not high enough to influence our measurements at T = 17 K significantly. The temporal evolution of both peaks can well be described by an exponential decay. The pump power dependencies of the decay times of the minimum of the PPT signal τ_1 and the maximum of the PPT signal τ_2 are shown in fig. 6.24. At pump powers below 5 mW the PPT signal is small and therefore the calculated error large, indicated by the error bars. We will ignore this part in our discussion. At powers above 5 mW we get the following picture: Both decay times τ_1 (0.8 to 1 ps) and τ_2 (1.5 to 2.5 ps) remains nearly constant, τ_2 increases slightly, but not signcantly with higher pump power. Therefore we can assume that the Cooper pair recombination time (decay time τ_2) depends not on the pump power, i.e. the injected quasiparticle density, in the used range and at T = 17 K. Cooper pair recombination times reported elsewhere are $\tau_{rec} \approx$ 1.5 to 2 ps at 20 K [Jaek 96], [Aver 01], [Han 90] in very good agreement with our experiment.

6.2.3 Bias Current Dependence

To measure the dependence of the PPT signal on the bias current the pump power P_{pump}, the probe power P_{probe} and the temperature T = 22 K are hold constant in this experiment. The bias current of the YBCO device is varied between -350 mA < I_{bias} < 350 mA. We measure the PPT signal as before by changing the pump-probe time delay t, while the detector trigger time is fixed at the probe THz pulse maximum.

Because the THz pulse amplitude itself depends linearly on the bias current (section 5.2.1) the PPT signal at t = 0 increases linearly with the bias current as well. The PPT

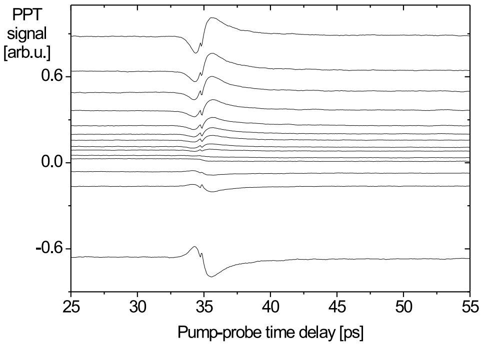

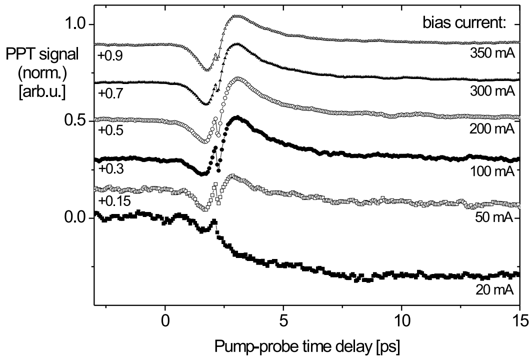

Fig. 6.24: Temporal evolution of the PPT signal at different bias currents at T = 22 K.

Fig. 6.25: Temporal evolution of the normalized PPT signal at different bias currents at T = 22 K. The curves are shifted for visibility.

signal as function of the pump-probe time delay at different bias currents is shown in fig. 6.25. To extract the bias current dependence of the PPT signal, we have to normalize the experimental data to the general probe THz amplitude at t = 0, see fig. 6.26. We get the following experimental results: at a small bias current, I_{bias} = 20 mA, the observed signal changes substantially, compared to previous results at higher bias current, used for measurements of the pump power dependence. At small bias currents below a certain threshold, wich depends on the trapped flux density of the device, *no* maximum in the PPT signal is observed and the PPT signal decreases to a signal equilibrium level below the value at t = 0. After warming up the device above T_C and start the measurement again at low bias currents this behavior is not observed. After a change in the direction of the applied current, the PPT signal is increased instead of decreased. Therefore we conclude that we measure an additional contribution to the THz probe signal, generated by the shielding current of the trapped flux, which is influenced by optical induced changes in the flux density of the excited area. At high bias currents this behavior does not play a role. The dependence on the current direction is easy to explain: optically activated vortices will be moved by the Lorentz force induced by the current and leave the sample what reduces the shielding current. The THz signal depends on the sum of bias and shielding current and therefore if both are in the same direction the signal decreases with decreasing shielding current. If the bias current is in the opposite direction of the shielding current, the PPT signal increases. Over a wide range of the bias current the maximum of the PPT signal is current independent, fig. 6.26. Below 100 mA (this value depends on the trapped flux density) the maximum of the PPT decreases significantly under the influence of optical induced flux motion in the device, see fig. 6.26. At $I_{bias} \rightarrow I_c$, above 250 mA, the maximum of the PPT signal decreases.

In fig. 6.27 the bias current dependence of the PPT minimum is indicated. The minimum of the PPT signal is not influenced by the bias current and roughly constant, but shows a small peak at a bias current of about 100 mA. Because of the small PPT signal at I_{bias} < 100 mA the conclusion if the minima changes or not is difficult (large

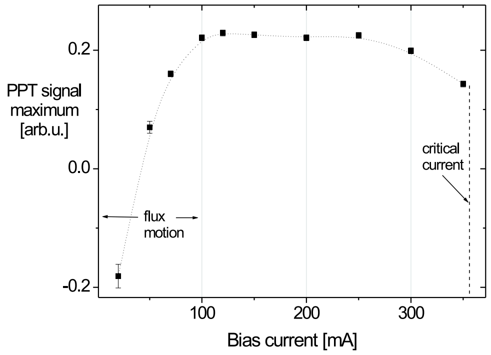

Fig. 6.26: Maximum of the PPT signal as function of the bias current at T = 22 K. The dash-pointed line is a guide for the eye.

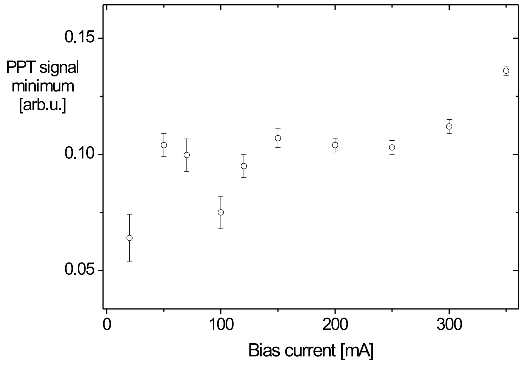

Fig. 6.27: Minimum of the PPT signal as function of the bias current at T = 22 K.

error bars). At high bias currents above 250 mA and near T_C the minima increases significantly. We recognize that this is the same value at which the maximum decreases. The measured decay times of the minimum and the maximum in the PPT signal do not depend on the bias current significantly, see fig. 6.29. For the THz radiation emission of high-T_C superconductors the flowing of a current is required. This current can be either an externally biased current (transport current) or a shielding current of flux, which is trapped inside the device (remanent state). The waveform of the THz radiation itself does not depend on the type of the current significantly [?]. If flux is trapped in our emitter and a current is biased additionally, then the THz signal results from the sum of both current components: transport and shielding. With the PPT signal we can now seperate both contributions, because transport and shielding current results in different PPT signals. At high bias current the flux dynamics does not play a role and the PPT signal is produced solely by the transport current. Nevertheless at low current densities the PPT signal is mainly influenced by optical induced flux flow.

We now try to observe the flux activation dynamics and therefore the following experiment is carried out: a small permanent magnet is brought near the YBCO sample, and generates magnetic flux vortices, which are pinned inside the superconducting thin film. After the magnet is took away the resulting THz radiation *without* bias current is observed. The result is shown in fig 6. 30. At first the PPT signal remains constant at $t < 0$. After $t = 0$ we observe a small decrease in the PPT signal until the laser pump excitation occurs at about t = 1 ps. After the pump excitation the PPT signal decreases fast in about 600 fs to a new equilibrium plateau. From the bias dependence of the THz signal amplitude we can estimate the value of the shielding current: $I_{before} = 15$ mA before and $I_{after} = 5$ mA after pump excitation. Following to equation 5.2 the value of the trapped magnetic flux density $|\vec{B}|$ can be estimated by the shielding current of the microbrigde and the bridge size like: $|\vec{B}_{before}| = 470\ \mu$T and $|\vec{B}_{after}| = 160\ \mu$T. The magnetic flux can be calculated by $\Phi_{before} = 7.5 \times 10^{-9}$ Tcm$^2 \approx 3\times10^4\ \Phi_0$ and $\Phi_{after} = 2.5 \times 10^{-9}$ Tcm$^2 \approx 10^4\ \Phi_0$. The laser pump power is $P_{pump} = 20$ mW resulting in a laser

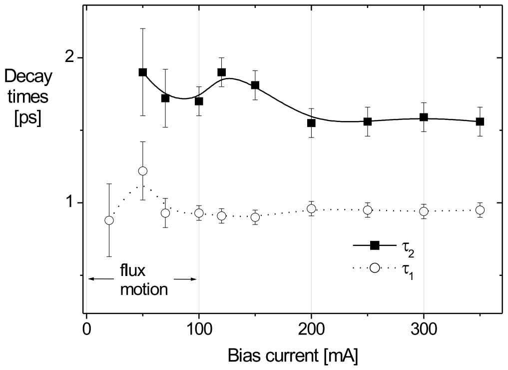

Fig. 6.28: Decay times of the minimum and the maximum of the PPT amplitude YBCO as function of the bias current I_{bias} at T = 22 K.

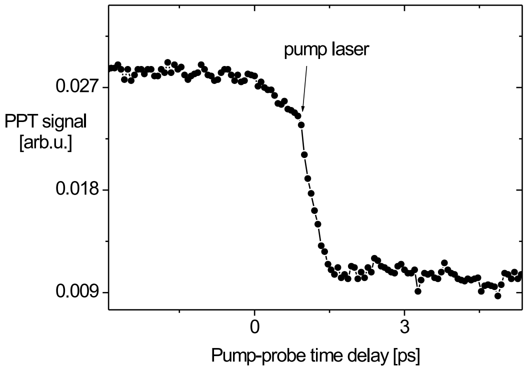

Fig. 6.29: Temporal evolution of the PPT signal of YBCO at a bias current of I_{bias} = 0 mA in the flux trapped state.

fluence of $F_{pump} = 320\ \mu Jcm^{-2}$. One pump laser pulse has an energy of 2.5 $\times 10^{-10}$ J. Taken the 2 kHz chopping and the 80 MHz repetition into account, the energy, which is nessecary for the flux activation, is therefore about: 3.125 $\times 10^{-19}$ J or 2 eV per vortice. This experimental data is much larger than the value estimated by theory (equation): 30..70 meV for the pinning potential. This is clear, because not the whole pump laser energy will be transfered to the vortices, but rather to other excitation processes in the interaction with quasiparticles and phonons. From the time of the decrease of the PPT signal and the width of the bridge the flux velocity can be roughly approximated by: $|\vec{v}_{flux}| = 3.3\ \times 10^7 m/s$. This value is in good agreement with reported data of ?

6.2.4 Temperature Dependence

After the measurement of the pump power and bias current dependency of the PPT signal the influence of the temperature on the experimental results is investigated. The temperature dependence of the superconducting properties, like described in the chapters 2 and 3, should lead to an observable change in the temporal evolution of the PPT signal. Because the THz emission of superconductors can only be observed below T_C, we can not compare the results we achieved at the superconducting state with the results measured in the normal state of the same sample. Nevertheless especially the transition region between these both states is of great physical interest. Optical transient reflectivity measurements and TDS methods can be applied in the normal and superconducting state, what is a clear advantage of these techniques to the PPT method.

The probe THz amplitude increases with temperature as described in chapter 5, section 5.2.3. Therefore the PPT signal is normalized to the average value at t = 0.

Because we assumed that the PPT signal response *before* and *after* the coherence peak is different in its origin, the PPT signal is seperated at the coherence peak for clearness. The results of the PPT experiment at different temperatures between T = 17 K and

T = 73 K for pump probe delay times *before* the coherence peak are shown in fig. 6.30 and for delay times t after the coherence peak in fig. 6.31. Because the results *before* the coherence peak are due to the THz pump changes, the pump-probe time delay has to be reversed, see fig. 6.30. From T = 17 K to about 50 K the PPT signal does not change significantly with temperature. At temperatures between 50 and 75 K the PPT amplitude changes dramatically: a) as visible in fig. 6.30, the minimum increases and shifts significantly to earlier times; b) the maximum of the PPT signal in fig. 6.31 decreases with increasing temperature and seams to shift slightly to earlier times (this shift is within the error bars and will be neglected); it vanishes near T_C. The temperature dependence both peaks in the PPT signal can be fitted well by the two-fluid model [Gort 34], indicated as solid (maximum) and dashed (minimum) lines in fig. 6.32. At the highest used temperatures of the experiments, fluctuations due to flux-flow and current induced heating influence the measurements, see error bars at fig. 6.32. Because of thermal effects of hot spot formation in the microbridge area, the sample temperature should be higher then the controller temperature, which is measured. Therefore at $T/T_C > 0.8$ the fit is not as good as at low temperatures. The highest temperature for the measurements is determined by the point where the bias current (which is nessecary for the THz emission and here about 50 mA) reaches the critical current and not the thermodynamical critical temperature T_C of the sample itself. Near T_C flux motion will occur and the PPT signal changes like described in the previous section. A further increase in the temperature leads to a measureable voltage drop at the sample.

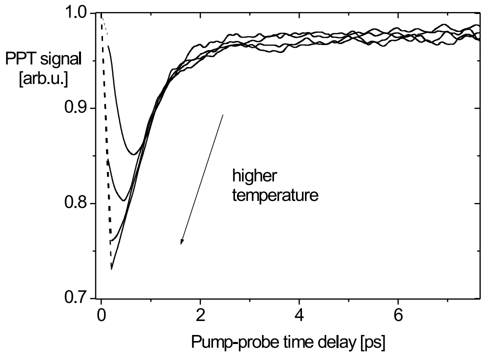

Fig. 6.30: Temporal evolution of the PPT minimum at different temperatures of 17 K < T < 73 K. The solid line represents the measured data points and the dashed line an estimated behavior near t = 0.

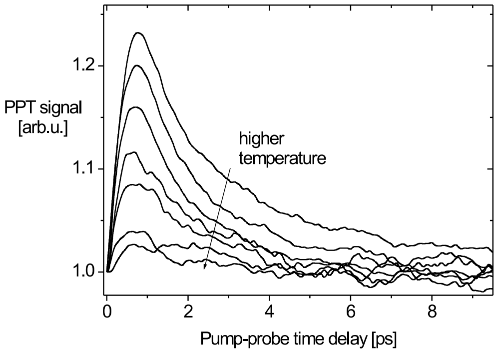

Fig. 6.31: Temporal evolution of the PPT maximum at different temperatures of 17 K < T < 73 K.

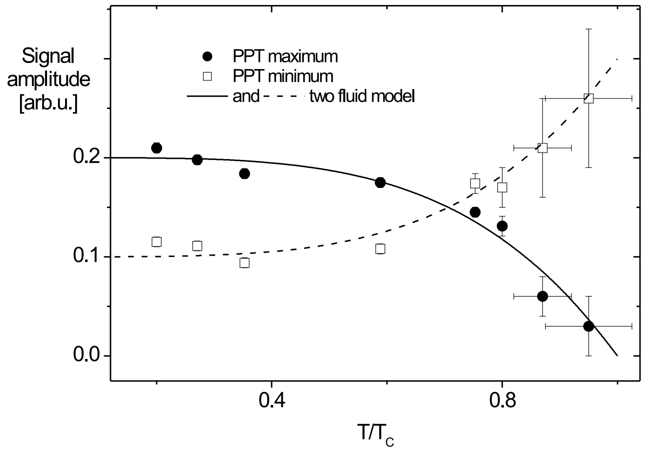

Fig. 6.32: Temporal evolution of the PPT amplitude of YBCO at different temperatures of 17 K < T < 75 K.

6.3 Discussion of the Results

An analysis of the data of the PPT experiment gives clear evidence, that the PPT signal includes two different responses of the superconductor to external fields. We conclude: the first one is the response to a THz field (this process is observed before the coherence artifact) and the second one is a response to the femtosecond laser field of the pump laser beam. This conclusion bases on the following arguments:
a) the temporal evolutions of the PPT signal *before* and *after* the coherent artifact are different,
b) the pump power and bias current dependence *before* and *after* the coherent artifact is different,
c) the temperature dependence of both responses are different,
d) the flux motion is only observed *after* the coherent artifact,
e) the probe THz pulse can not be influenced by the laser pump beam *before* the coherent artifact appears and
f) the calculations of the decay times of both effects are in very good agreement to carrier scattering times and Cooper pair recombination times obtained by optical measurements [Han 90] and TDS [Bror 96], respectively.
Therefore the PPT techniques shows a high potential: the possibility of a measurement of the carrier dynamics at excitation frequency above and below the gap frequency. The results before the coherent artifact can be described by a normal carrier response to a THz field. The revealed scattering times at THz frequencies (see fig. 6.34) depend on temperature and are in a good agreement to data observed at about 450 GHz by means of TDS [Bror 96]. The response of the *normal* carrier fraction to the THz field is observed, while the supercarriers response is not measureable, because the field generated by the supercarriers is the measured general THz field and does not contribute to a change in

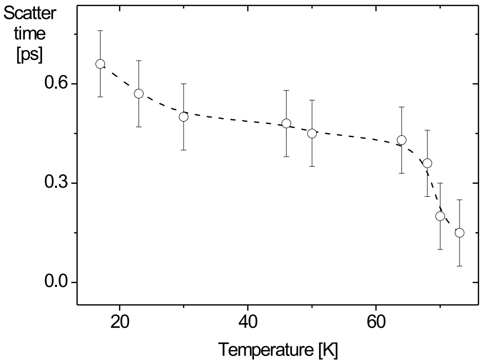

Fig. 6.33: Temperature dependence of the scattering time of the normal component of the PPT signal in fig. 6.30 at 17 K < T < 75 K. The dashed line is a guide to the eye.

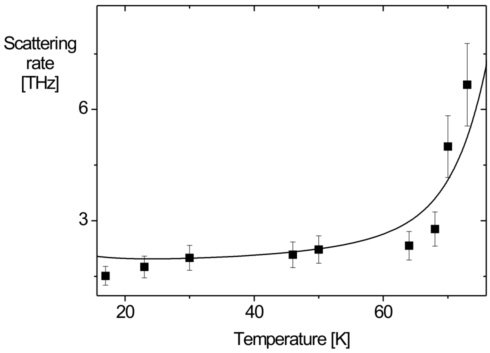

Fig. 6.34: Temperature dependence of the scattering rate of the normal electrons, calculated from the data shown in fig. 6.34. The solid line is a fit of the weak coupling model equation (3.25).

the THz signal itself. The observed temperature dependence of the scattering rate can be fitted by the *weak coupling model* introduced in section 3.2.1 with the *same* parameters as reported by Wilke *et al.* [Wilk 00]: $a = 0.11$, $b_1 = 15$, $b_2 = 1$. The in the model described temperature independent elastic scattering rate is $\Gamma_N^{el} = 7.8$ meV ([Wilk 00]: 1.2 meV) and the inelastic temperature dependent scattering rate with the value at T_C of $\Gamma^{inel}(T_C) = 41.4$ meV ([Wilk 00]: 35.8 meV). This temperature dependence of the scattering rate was proposed previously to explain the so called " anomalous coherence peak" of the real part of the conductivity of YBCO at low temperature [Bror 96]. This peak has been observed by means of microwave techniques [Bonn 92] and measurements of the thermal conductivity [Yu 92]. The origin of the "anomalous coherence peak" has been attributed to the rise in the scattering time of the normal carriers. From the Drude equation (3.20) it follows that the real part of the conductivity is proportional to $\tau(T) \times f_n(T)$.

The temporal evolution of the PPT signal *after* the coherent artifact can be explained by avalanche Cooper pair breaking after the optical excitation due to the pump pulse. The change in the Cooper pair density changes the transmittivity. This modifies the output coupling and leads to an increase in the THz probe amplitude (PPT signal). The time scale of this effect is dominated by the avalanche effect of the Cooper pair breaking and the time the recombination requires. Therefore the results are very similar to the pump-and-probe experiments to investigate the transient changes in the transmittivity and reflectivity [Han 90]. In fig. 6.33 the temperature dependence of the decay time of the PPT maximum, which we attribute to the Cooper pair recombination time, is indicated. It can be notified, that the measured decay times and their temperature dependence are in a very good agreement with previous measurements of the quasiparticle relaxation time of YBCO by means of time resolved reflectivity measurements by Han *et al.* [Han 90]

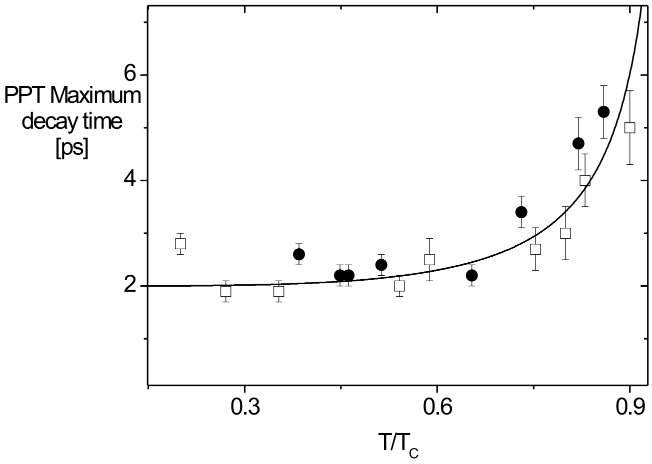

Fig. 6.35: Temporal evolution of the PPT amplitude of YBCO at different temperatures of 17 K < T < 75 K. The solid line is a fit to a temperature dependence with $\alpha = 2$.

and Kabanov *et al.* [Kaba 99]. The temperature dependence of the PPT maximum decay time can be fitted well, as indicated in fig. 6.34 with equation (3.35) and $\alpha = 2$. This supports our suggestion that we observe the quasiparticle relaxation and Cooper pair recombination. Typical cuprate superconducting materials indicate Cooper pair recombination times of some picosecond which is follows the hot carrier thermalization and quasiparticle avalanche production by ultrafast laser excitation.

7 Summary and Prospects

This work describes the usage of the novel PPT method to measure the carrier dynamics of semiconductors and cuprate superconductors on a subpicosecond time scale.
For the first time this method was used to investigate the materials LT-GaAs and YBCO. Because the emission of THz pulses by the material under observation is a requirement of the technique, we analized the THz emission of LT-GaAs and YBCO dipole antennas carefully. In this analyzis we measured for the first time the doping dependence (Pr atoms in YBCO) of the THz emission efficiency and could proof a relation to the change in the output coupling of the device. The efficiency could be increased by 6 times compared to the undoped YBCO samples avery important step forward for an application. Further the temperature dependence of the THz emission of YBCO samples was observed and compared to recent theories of the temperature dependence of the London penetration depth λ_L and the THz emission process (*kinetic inductance*- and *current modulation* model). The best fit to the measured data could be obtained by the current modulation model with output coupling included and $\alpha = 2$. This is for the first time a direct comparison of both models, which desribe the THz emission process. Nevertheless because of heating the data near T_C includes large errors which complicates an exact conclusion.
In the past PPT experiments were realized on GaAs (not low-temperature grown) [Jeps 96] and on LT-GaAs [Hu 95]. While Hu *et al.* measured the ballistic carrier transport due to a high resolution of 10 fs, we measured for the first time the carrier trapping process in LT-GaAs under different electrical field strengths by the PPT method. By fitting the experimental results to rate equations, proposed by Othonos *et al.* [Otho 98], the most important characteristic time constants of the carrier dynamics in this material could be obtained: the momentum relaxation time $\tau_{rel} = 65$ fs, a hot carrier trapping time $\tau_{trap1} = 250$ fs and a trapping time of electrons from the bottom of the conduction band $\tau_{trap2} = 2.2$ ps. An alternative explanation of the observation was given by the *velocity overshoot*, which could in principle result in the observed deviation from the exponential behavior. Nevertheless following to [Jeps 96] the velocity overshoot is only observable at lower carrier density than that used in our experiment. An increase of the trapping time, calculated from the measured PPT signals, on the carrier density and on the bias electrical field was observed for the first time. The results were explained by trapping state saturation and an energetically shift of the mobility edges to deeper Urbach tail states (*Andersons localization model*).
In the case of the YBCO the PPT method was used for the first time to investigate the carrier dynamics of this material. It turns out that the PPT method is an unique tool because it offers the possibility to observe the response of the material to *two* external electrical fields: the THz field and the femtosecond laser field (pump laser). Compared to GaAs this difference is caused by the high amount of free charge carriers in the material without pumping. Therefore the THz field accelerates the normal carriers, leading to a

contribution to the PPT signal and the femtosecond laser changes the Cooper pair density leading to a further contribution to the PPT signal. The conclusion is that the PPT method combines two other techniques: the optical *pump-and-probe* and the TDS THz technique. As results of the measurements quasiparticle scattering rates and Cooper pair recombination times (governed by a phonon decay time because of the avalanche process) were obtained. For the first time the dependence of these time constants on the bias current, the injected carrier density and the temperature were measured and compared to the *two fluid model*, the *weak coupling model* and a model proposed by Kabanov *et al.* to explain the phonon decay in YBCO. Quasiparticle scattering times of 100 to 600 fs, and phonon decay times of 2 to 6 ps, depending on temperature, were measured in good agreement to other experimental methods.

Furthermore because of the bias current dependence of the emitted THz signal, the PPT method were used to observe the vortice dynamics directly and time resolved for the first time. The flux velocity were obtained to be about 3.3 $\times 10^7 m/s$.

Despite the fact that the PPT method is very usefull the requirement of the THz emission from the sample is a clear disadvantage because cuprate superconductors can only emit THz pulses below T$_C$. Nevertheless especially the change in the behavior from below to above T$_C$ is of physical interest. Other methods are capable to measure this (e.g. TDS). In the case of GaAs the possibility to observe the material under high electrical fields is an interesting possibility and by using other sample geometries even higher fields up to the break down field are future prospects. For the cuprate superconductors a comparison of the PPT results of YBCO to other compounds could reveal much interesting physics.

Bibliography

[Alex 94] S. Alexandrou, C. C. Wang, R. Sobolewski, T. Y. Hsiang, IEEE J. Quantum Electron. **30**, 1332 (1994)

[Alfa 84] R. R. Alfano, *Semiconductors Probed by Ultrafast Laser Spectroscopy*, Volumes I and II, Academic Press, New York (1984)

[Alle 87] P. B. Allen, Phys. Rev. Lett. 59, 1460 (1987)

[Alle 88] P. B. Allen, W. E. Picket, H. Krakauer, Phys. Rev. B **37**, 7482 (1988)

[Ande 62] P. W. Anderson, Phys. Rev. Lett. **9**, 309 (1962)

[Anis 75] S. I. Anisimov, B. L. Kapeliovich, T. L. Perel′man, Sov. Phys. JETP 39, 375 (1975)

[Anla 89] S. M. Anlage, H. Sze, H. J. Snortland, S. Tahara, B. Langley, C. B. Eom, M. R. Beasley, R. Taber, Appl. Phys. Lett. **54**, 26, 2710 (1989)

[Atake 91] T. Atake, A. Honda, H. Kawaji, Physica C **190**, 70 (1991)

[Aust 84] D. H. Auston, K. P. Cheung, P. R. Smith, Appl. Phys. Lett. **45**, 284 (1984)

[Aver 01] R. D. Averitt, G. Rodriguez, A. I. Lobad, J. L. W. Siders, S. A. Trugman, A. J. Taylor, Phys. Rev. B **63**, 140502(R) (2001)

[Bake 74] J. W. Baker, J. D. Lejeune, D. G. Naugle, J. Appl. Phys. **45**, 5043 (1974)

[Bedn 86] J. G. Bednorz, K. A. Mller, Z. Phys. B **64**, 189 (1986)

[Beni 93] P. K. Benicewicz, A. J. Taylor, Opt. Lett. **18**, 1332 (1993)

[Beni 94] P. K. Benicewicz, J. P. Roertz, A. J. Taylor, J. Opt. Soc. Am. B, **11**, 2533 (1994)

[Benn 90] B. R. Bennet, R. A. Soref, J. A. Del Alamo, IEEE J. Quantum Electron. **26**, 113 (1990)

[Bluz 91] N. Bluzer, Phys. Rev. B **44**, 10222 (1991)

[Bluz 92] N. Bluzer, J. Appl. Phys. 71, 1336 (1992)

[Bonn 88] D. A. Bonn, A. H. O′Reilly, J. E. Greedan, C. V. Stager, T. Timusk, K. Kamaras, D. B. Tanner, Phys. rev. B **37**, 1574 (1988)

[Bonn 92] D. A. Bonn, P. Dosanjh, R. Liang, W. N. Hardy, Phys. Rev. Lett. **68**, 2390 (1992)

[Borc 93] J. Borck, Dissertation, University of Jena (1993)

[Bras 92] J. Brasunas, B. Lakew, C. Lee, J. Appl. Phys. **71**, 3639 (1992)

[Bror 94] S. D. Brorson, J. Zhang, S. R. Keiding, Appl. Phys. Lett. **64**, 2385 (1994)

[Bror 96] S. D. Brorson, R. Buhleier, I. E. Trofimov, J. O. White, Ch. Ludwig, H. U. Habermeier, J. Kuhl, Journal of the Optical Society of America **B**, Vol. 13, issue 9, (1996)

[Brov 95] L. R. Brovelli, U. Keller, T. H. Chiu, J. Opt. Soc. Am. B **12**, 311 (1995)

[Brow 93] E. R. Brown, F. W. Smith, K. A. McIntosh, J. Appl. Phys. **73**, 1480 (1993)

[Brun 95] B. Brunner, Dissertation, University of Regensburg (1995)

[Bunt 00] P. S. Bunt, T. G. Ference, K. A. Puzey, D. B. Tanner, N. Tache, W. J. Varhue, Proc. SPIE 4111 (2000)

[Ciep 94] M. Z. Cieplak, S. Guha, S. Vadlamannati, T. Giebultowicz, P. Lindenfeld, Phys. Rev. B, **50**, Issue 17, 12876 (1994)

[Chan 77] J. J. Chang, D. J. Scalapino, Phys. Rev. B 15, 2651 (1977)

[Chan 79] W.H. Chang, Appl. Phys. Lett. 50, 8129 (1979)

[Chev 98] R. A. Cheville, D. Grischkowsky, Opt. Lett. **23**, 531 (1998)

[Chri 94] D. B. Chrisey, G. K. Hubler, Pulsed Laser Deposition of thin films, John Wiley & Sons, New York (1994)

[Chua 92] S. L. Chuang, S. Schmitt-Rink, B. I. Greene, P. N. Saeta, A. F. J. Levi, Phys. Rev. Lett. **68**, (1992)

[Chwa 90] J. M. Chwalek, C. Uher, J. F. Whitaker, G. Mourou, J. Agostinelli, M. Lelental, Appl. Phys. Lett. **57**, 1696 (1990)

[Clar 77] J. Clarke, G. I. Hoffer, P. L. Richards, N.-H. Yeh, J. Appl. Phys. 48, 4865 (1977)

[Cohe 90] R. E. Cohen, W. E. Pickett, H. Krakauer, Phys. Rev. Lett. **64**, 2575 (1990)

[Crys 01] Product information Crystal GmbH, see $http://www.crystal-gmbh.com/$

[Darr 92] J. T. Darrow, X. Cheng, D. H. Auston, J. D. Morse, IEEE J. Quantum Electron. **28**, 1607 (1992)

[Easl 90] G. L. Easley, J. Heremanns, M. S. Meyer, G. L. Doll, S. H. Liou, Phys. Rev. Lett. **65**, 3445 (1990)

[Engh 93] J. Engholm, S. R. Keiding, C. B. Sorensen, P. E. Lindelof, W. W. R"uhle, X. Q. Zhou, J. Appl. Phys. **74**, (1993)

[Fatt 89] C. Fattinger, D. Grischkowsky, Appl. Phys. Lett. **54**, 490 (1989)

[Fior 90] A. T. Fiory, A. F. Hebard, R. H. Eick, P. M. Mankiewich, R. E. Howard, M. L. O′Malley, Phys. Rev. Lett. **65**, 3441 (1990)

[Flik 92] M. I. Flik, Z. M. Zhang, K. E. Goodson, M. P. Siegal, J. M. Phillips, Phys. Rev. B **46**, 5606 (1992)

[Flik 93] M. I. Flik, Z. M. Zhang, K. E. Goodson, Appl. Phys. Lett. **62**, 2862 (1993)

[Folde 89] M. Foldeaki, M. E. McHenry, R. C. O′Handley, Phys. Rev. B **41**, 2883 (1989)

[Fren 89] A. Frenkel, M. A. Saifi, T. Venkatesan, C. Lin, W. D. Wu, A. Iham, Appl. Phys. Lett. 54, 1594 (1989)

[Fren 90] A. Frenkel, M. A. Saifi, T. Venkatesan, P. England, X. D. Wu, A. Inam, J. Appl. Phys. **67**, 3054 (1990)

[Fren 91] A. Frenkel, Physica C **180**, 251 (1991)

[Fren 93] A. Frenkel, Phys. Rev. B **48**, 9717 (1993)

[Gers 84] E. M. Gershenzon, G. N. Gol′tsman, A. D. Semenov, A. V. Sergeev, Solid State Commun. 50, 207 (1984)

[Gers 89] E. M. Gershenzon, M. E. Gershenzon, G. N. Gol′tsman, A. M. Lyul′kin, A. D. Semenov, A. V. Sergeev, Sov. Phys. Tech. Phys. 34, 195 (1989)

[Golt 95] G. N. Gol′tsman, B. S. Karasik, O. V. Okunev, A. L. Dzardanov, E. M. Gershenzon, H. Ekstroem, S. Jacobsson, E. Kollberg, IEEE Trans. Appl. Supercon. **5**, 3065 (1995)

[Gork 88] L. P. Gorkov, N. B. Kopnin, Sov. Phys. Usp. **31**, 850 (1988)

[Gort 34] Gorter, Physica **1**, 306 (1934)

[Gree 92] B. I. Greene, P. N. Saeta, D. R. Dykaar, S. Schmitt-Rink, S. L. Chuang, IEEE J. Quantum Electron. **QE-28**, 2302 (1992)

[Gren 97] P. Grenier, J. F. Whitaker, Appl. Phys. Lett. **70**, 1998 (1997)

[Gris 90] D. Grischkowsky, S. Keiding, Appl. Phys. Lett. **57**, 1055 (1990)

[Gris 90b] D. Grischkowsky, S. Keiding, M. van Exter, C. Fattinger, J. Opt. Soc. Am. B **7**, 2006 (1990)

[Hage 89] S. J. Hagen, Z. Z. Wang, N. P. Ong, Phys. Rev. B **40**, 9389 (1989).

[Hall 66] R. T. Hall, D. Vrabec, J. M. Dowling, *A High-Resolution, Far Infrared Double-Beam Lamellar Grating Interferrometer*, Appl. Opt. **5**, 1147 (1966)

[Han 90] S. G. Han, Z. V. Vardeny, O. G. Symko, G. Koren, Phys. Rev. Lett. **67**, 1053 (1990); S.G. Han, Z. V. Vardeny, K. S. Wong, O. G. Symko, and G. Koren, Phys. Rev. Lett.**65**, 2708 (1990)

[Hang 96] M. Hangyo, S. Tomozawa, Y. Murakami, M. Tonouchi, M. Tani, Z. Wang, K. Sakai, and S. Nakashima, Appl. Phys. Lett. **69**, 2122 (1996)

[Hard 91] H. Harde, S. Keiding, D. Grischkowsky, Phys. Rev. Lett., **66**, 1834 (1991)

[Hegm 93] F. A. Hegmann, J. S. Preston, Phys. Rev. B 48, 16023 (1993)

[Hegm 95] F. A. Hegmann, D. Jacobs-Perkins, C. C. Wang, S. H. Moffat, R. A. Hughes, J. S. Preston, M. Currie, P. M. Fauchet, T. Y. Hsiang, R. Sobolewski, Appl. Phys. Lett. **67**, 285 (1995)

[Hein 99] M. A. Hein, High Temperature Superconducting Thin Films at Microwave Frequencies, Springer Tracts in Modern Physics Vol. 155 (Springer, Heidelberg, 1999)

[Hens 97] S. Hensen, G. M"uller, C. T. Rieck, K. Scharnberg, Phys. Rev. B **56**, 6237 (1997)

[Hins 96] H. Hinsch, *Elektronik*, Springer-Verlag, Berlin, Heidelberg, p25 (1996)

[Holc 94] M. J. Holcomb, J. P. Collman, W. A. Little, Phys. Rev. Lett. **73**, 2360 (1994)

[Hu 95] B. B. Hu, E. A. Souza, W. H. Knox, J. E. Cunningham, M. C. Nuss, A. V. Kuznetsov, S. L. Chuang, Phys. Rev. Lett. **74**, 1689 (1995)

[Ibac 99] H. Ibach, H. Lüth, *Festk"orperphysik*, Springer Verlag, Heidelberg, p.386 (1999).

[Ihle 91] D. Ihle, N. M. Plakida, Physica C **185-189**, 1637 (1991)

[Ilic 96] E. Il′ichev, L. D"orrer, G. Hildebrandt, F. SChmidl, V. Zakosarenko, P. Seidel, Appl. Phys. Lett. **68**, 5, 708 (1996).

[Jac 00] F. Jacob, Diploma thesis, University of Frankfurt am Main, p. 14 (2000)

[Jaek 96] C. Jaekel, H. G. Roskos, H. Kurz, Phys. Rev. B **54**, R6889 (1996)

[Jeps 96] P. U. Jepsen, R. H. Jacobsen, S. R. Keiding, J. Opt. Am. B, **13**, 2424 (1996)

[Kaba 99] V. V. Kabanov, J. Demsar, B. Podobnik, D. Mihailovic, Phys. Rev. B , (1999)

[Kaba 00] V. V. Kabanov, J. Demsar, and D. Mihailovic, Phys. Rev. B 61, 1477 (2000)

[Kadi 86] A. M. Kadin, A. Goldman, *Nonequilibrium Superconductivity*, edited by D. Langenberg, A. Larkin, North-Holland, Amsterdam (1986)

[Kama 90] K. Kamaras, S. L. Herr, C. D. Porter, N. Tache, D. B. Tanner, S. Etemad, T. Venkatesan, E. Chase, A. Inam, X. D. Wu, M. S. Hedge, B. Dutta, Phys. Rev. Lett. **64**, 84 (1990)

[Kapl 76] S. B. Kaplan, C. C. Chi, D. N. Langenberg, J. J. Chang, S. Jafarey, D. J. Scalapino, Phys. Rev. B **14**, 4854 (1976)

[Kash 85] J. A. Kash, J. C. Tsang, J. M. Hvam, Phys. Rev. Lett. **54**, 2151 (1985)

[Kaze 91] A. S. Kazeroonian, T. K. Cheng, S. D. Brorson, Q. Li, E.P.Ippen, X. D. Wu, T. Venkatesan, S. Etemad, M. S. Dresselhaus, G. Dresselhaus, Solid State Commun. **78** (1991)

[Kell 89] M. K. Kelly, P. Barboux, J. M. Tarascon, D. E. Aspnes, Phys. Rev. B **40**, 6797 (1989).

[Khre 91] I. A. Khrebtov, Sov. J. Opt. Technol. **58**, 261 (1991)

[Kim 64] Y. B. Kim, Rev. Mod. Phys. **36**, 39 (1964)

[Kiwa 98] T. Kiwa, private communications

[Krak 88] H. Kakauer, W. E. Pickett, R. E. Cohen, J. Supercond. bf 1, 111 (1988)

[Kroek 89] D. Kroekel, D. R. Grischkowsky, M. B. Ketchen, Appl. Phys. Lett. **54**, 1046 (1989)

[Krus 90] P. W. Kruse, Semicond. Sci. Technol. **5**, 229 (1990)

[Kuma 92] R. Kumar, S. K. Malik, S. P. Pai, P. R. Apte, R. Pinto, R. Vijayaraghavan, Phys. Rev. B **46**, 5766 (1992)

[Kuzn 93] A. V. Kuznetsov, C. J. Stranton, Phys. Rev. B **48**, 10828 (1993)

[Lee 93] J.-Y. Lee, T. R. Lemberger, Appl. Phys. Lett. **62**, 2419 (1993)

[Lee 95] S. Y. Lee, G. B. Kim, W. N. Kang, T. S. Hahn, S. S. Choi, B. Oh, S. H. Moon, A. G. Denisov, Physica **C 244**, 63 (1995)

[Leite00] A. Leitenstorfer, S. Hunsche, J. Shah, M. C. Nuss, W. H. Knox, Phys. Rev. B **61**, 16642 (2000)

[Levi 93] B. G. Levi, Physics Today **5**, 17 (1993)

[Lind 94] M. Lindgren, M. A. Zorin, V. Trifinov, M. Danerud, D. Winkler, B. S. Karasik, G. N. Gol′tsman, E. M. Gershenzon, Appl. Phys. Lett. **65**, 3398 (1994)

[Lind 99] M. Lindgren, M. Currie, C. Williams, T. Y. Hsiang, P. M. Fauchet, R. Sobolewski, S. H. Moffat, R. A. Hughes, J. S. Preston, F. A. Hegman, Appl. Phys. Lett. **74**, 853 (1999)

[Liu 94] X. Liu, A. Prasad, W. M. Chen, A. Kurpiewski, A. Stoschek, Z. Lilienthal-Weber, E. R. Weber, Appl. Phys. Lett. **65**, 3002 (1994)

[Look 93] D. C. Look, D. C. Walters, G. D. Robinson, J. R. Sizelove, M. G. Mier, C. E. Stutz, J. Appl. Phys. **74**, 306 (1993)

[Luys 98] M. Luysberg, H. Sohn, A. Prasad, P. Specht, Z. Lilienthal-Weber, E. R. Weber, J. Gebauer, R. Krause-Rehberg, J. Appl. Phys. **83**, 561 (1998)

[Mann 88] J. Mannhart, P. Chaudhari, D. Dimos, C. C. Tsuei, T. R. McGuire, Phys. Rev. Lett. **61**, 2476 (1988)

[McDo 87] D. G. McDonald, Appl. Phys. Lett. **50**, 775 (1987)

[McIn 95] K. A. McIntosh, E. R. Brown, K. B. Nichols, O. B. McMahon, D. F. DiNatale, T. M. Lyszczarz, Appl. Phys. Lett. **67**, 3844 (1995)

[McIn 96] K. A. McIntosh, K. B. Nichols, S. Verghese, E. R. Brown, Appl. Phys. Lett. **70**, 354 (1996).

[McMi 68] W. L. McMillan, Phys. Rev. **167**, 331 (1968)

[Mell 95] M. R. Melloch, J. M. Woodall, E. S. Harmon, N. Otsuka, F. H. Pollack, D. D. Nolte, R. M. Feenstra, M. A. Lutz, Annu. Rev. Mater. Sci. **25**, 547 (1995)

[Mesc 99] D. Meschede, *Optik, Licht und Laser*, Teubner Verlag, Stuttgart, p.51 (1999)

[Miha 93] D. Mihailovic, K. F. McCarty, D. S. Ginley, Phys. Rev. B **46**, 8910 (1993)

[Mill 91] D. Miller, P. L. Richards, S. Etemad, A. Inam, T. Venkatesan, B. Dutta, X. D. Wu, C. B. Eom, T. H. Geballe, N. Newman, B. F. Coole, Appl. Phys. Lett. **59**, 2326 (1991)

[Mühl 59] B. M"uhlschlegel, Z. Phys. **155**, 313 (1959)

[Mura 01] H. Murakami, T. Fukui, T. Kiwa, M. Tonouchi, T. Uchiyama, I. Iguchi, Z. Wang, proc. of ISEC 2001, 299 (2001)

[Nahu 91] M. Nahum, S. Verghese, P. L. Richards, K. Char, Appl. Phys. Lett. **59**, 2034 (1991)

[Nash 00] S. Nashima, M. Tonouchi, M. Hangyo, K.-U. Barholz,F. Schmidl, P. Seidel, Jpn.J.Appl.Phys. Vol. 39, pp.L663-666 (2000)

[Nebo 93] R. S. Nebosis, M. A. Heusinger, W. Schatz, K. F. Renk, G. N. Gol′tsman, B. S. Karasik, A. D. Semenov, G. M. Gershenzon, IEEE Trans. Appl. Superconductivity **3**, 2160 (1993)

[Nebo 94] R. S. Nebosis, M. A. Heusinger, W. Schatz, A. Piehler, R. Loew, N. Reschauer, K. F. Renk, A. D. Semenov, P. Kouminov, I. G. Goghidze, E. M. Gershenzon, *High Temperature Superconducting Detectors: Bolometric and Nonbolometric*, edited by M. Nahum and J. C. Villegier, Proc. SPIE 2159, 77 (1994)

[Nuss 91] M. C. Nuss, P. M. Mankievich, M. L. O′Malley, E. H. Westerwick, Phys. Rev. Lett. **66**, 3305 (1991)

[Oren 90] J. Orenstein, G. A. Thomas, A. J. Millis, S. L. Cooper, D. H. Rapkine, T. Timusk, L. F. Scheemeyer, J. V. Waszczak, Phys. Rev. B **42**, 6342 (1990)

[Osba 97] C. J. Osbahr, Master thesis: *Subpicosecond pulse propagation on Au and* $YBa_2Cu_3O_x$ *transmission lines*, p5 (1997)

[Otho 98] A. Othonos, J. Appl. Phys. **83**, 1789 (1998)

[Otho 91] A. Othonos, H. M. van Driel, J. F. Young, P. J. Kelly, Phys. Rev. B **43**, 6682 (1991)

[Peac 91] S. D. Peacor, R. A. Richardson, F. Nori, C. Uher, Phys. Rev. B **44**, 9508 (1991)

[Pede 92] J. E. Pedersen, S. R. Keiding, IEEE J. Quan. El. **28**, 2518 (1992)

[Pede 93] J. E. Pedersen, V. G. Lyssenko, J. M. Hvam, P. U. Jepsen, S. R. Keiding, C. B. Sorensen, P. E. Lindelof, Appl. Phys. Lett. **62**, 1265 (1993)

[Pede 93a] J. E. Pedersen, S. R. Keiding, C. B. Sorensen, P. E. Lindelof, W. W. R"uhle, X. Q. Zhou, J. Appl. Phys. **74**, 7022 (1993)

[Perr 83] N. Perrin, C. Vanneste, Phys. Rev. B 28, 5150 (1983)

[Pfei 00] K. F. Pfeiffer, S. Tautz, P. Kiesel, S. Malzer, G. H. D"ohler, Appl. Phys. Lett. **77**, 2349 (2000)

[Pick 90] W. E. Picket, R. E. Cohen, H. Krakauer, Phys. Rev. B **42**, 8764 (1990)

[Pine 96] A. S. Pine, R. D. Suenram, E. R. Brown, K. A. McIntosh, J. Mol. Spectrosc. **175**, (1996)

[Plak 95] N. M. Plakida, *High-Temperature Superconductivity*, Springer Press (1995)

[Pond 87] J. M. Pond, J. H. Claassen, W. L. Carter, IEEE Trans. Microwave Theory and Techniques, **MTT-35**, 1256 (1987)

[Pool 95] C. P. Poole, H. A. Farach, R. J. Creswick, *Superconductivity*, Academic Press (1996)

[Pool 95p185] see [Pool 95] page 185

[Pool 95p28] see[Pool 95] page 28 and 29

[Poul 95] G. D. Poulin, J. Lachapelle, S. H. Moffat, F. A. Hegmann, J. S. Preston, Appl. Phys. Lett. **66**, 2576 (1995)

[Puze 93] K. A. Puzey, US Patent 5.210.637, (1993)

[Rado 95] H. B. Radousky, J.Mater.Res. Vol.7, Issue 7, pp. 1917-1955 (1995)

[Reiz 89] M. Reizer, Phys. Rev. B 39, 1602 (1989)

[Rich 89] P. L. Richards, J. Clarke, R. Leoni, Ph. Lerch, S. Verghese, M. R. Beasley, T. H. Geballe, R. H. Hammond, P. Rosenthal, S. R. Spielman, Appl. Phys. Lett. **54**, 283 (1989)

[Roth 67] A. Rothwarf, B. N. Taylor, Phys. Rev. Lett. **19**, 27, (1967)

[Ruva 96] J. Ruvalds, Supercond. Sci. Technol. **9**, 905 (1996)

[Sanc 92] D. Sanchez, A. Junod, J. Y. Genoud, T. Graf, J. Muller, Physica C **200**, 1 (1992)

[Sauv 91] J. E. Sauvageau, D. G. McDonald, E. N. Grossman, IEEE Trans. Magn. **27**, 2757 (1991)

[Schm 97] V. V. Schmidt, *The Physics of Superconductors* (P. M"uller, A. V. Ustinov (Eds.)), Springer Press, Berlin (1997)

[Seeg 88] K. Seeger, *Semiconductor Physics*, Vol. 40, Springer New York (1988)

[Segs 97] G. Segschneider, T. Dekorsky, R. Hey, K. Ploog, Appl. Phys. Lett. **71**, 2779 (1997)

[Segs 02] G. Segschneider, F. Jacob, T. L"offler, H. G. Roskos, S. Tautz, P. Kiesel, G. D"ohler, Phys. Rev. B **65**, (2002)

[Seme 93] A. D. Semenov, I. G. Goghidze, G. N. Gol′tsman, A. V. Sergeev, E. E. Aksaev, E. M. Gershenzon, IEEE Trans. Appl. Superconduct. 3, 2131 (1993)

[Seme 95] A.D. Semenov, R.S. Nebosis, Yu.P. Gousev, M.A. Heusinger, K.F. Renk, Phys. Rev. B 52, 581 (1995)

[Serg 94] A. V. Sergeev, A. D. Semenov, P. Kouminov, V. Trifonov, I. G. Goghidze, B. S. Karasik, G. N. Gol′tsman, E. M. Gershenzon, Phys. Rev. B **49**, 9091 (1994)

[Sha 92] W. Sha, J. K. Rhee, T. B. Norris, W. J. Schaff, IEEE J. Quantum Electron. **28**, 2445 (1992)

[Side 99] J. L. W. Siders, S. A. Trugman, F. H. Garzon, R. J. Houlton, A. J. Taylor, Phys. Rev. B **61**, 13633 (1999)

[Sieg 96] U. Siegner, R. Fluck, G. Zhang, U. Keller, Appl. Phys. Lett. **69**, 2566 (1996)

[Smit 88] P. R. Smith, D. H. Auston, M. C. Nuss, IEEE J. Quantum Electron. **QE-24**, 255 (1988)

[Sobo 01] R. Sobolewski, J. R. Park, IEEE Trans. Apl. Supercond. **11**, 727 (2001)

[Sosn 97] T. S. Sosnowski, T. B. Norris, H. H. Wang, P. Grenier, J. F. Whitaker, Appl. Phys. Lett. **70**, 3245 (1997)

[Spec] Spectra-Physics, 1335 Terra Bella Avenue, Mountain View, CA 94043

[Stel 00] M. Stellmacher, J. Nagle, J. F. Lampin, P. Santoro, J. Vaneecloo, A. Alexandrou, J. Appl. Phys. **88**, 6026 (2000)

[Sze 96] siehe Gürtler!

[Tani 94] M. Tani, K. Sakai, H. Abe, S. Nakashima, H. Harima, M. Hangyo, Y. Tokuda, K. Kanemoto, Y. Abe, N. Tsukada, Jpn. J. Appl. Phys. **1 33**, 4807 (1994).

[Tani 97b] M. Tani, S. Matsuura, K. Sakai, S. Nakashima, Appl. Optics, **36**, No. 30, 7853 (1997).

[Tani 97] M. Tani, M. Tonouchi, M. Hangyo, Z. Wang, N. Onodera, K. Sakai, Jpn. J. Appl. Phys. **36**, 3b, 1984 (1997).

[Tink 88] M. Tinkham, Helvetica Physica Acta **61**, 443 (1988).

[Tris 90] J.M. Triscone, O. Fischer, O. Brunner, L. Antognazza, A. D. Kent, M. G. Karkut, Phys. Rev. Lett. **64**, 804 (1990).

[Tomi 02] Y. Tominari, T. Kiwa, H. Murakami, M. Tonouchi, H. Wald, P. Seidel, H. Schneidewind, Appl. Phys. Lett. **80**, 3147 (2002).

[Tono 96] M. Tonouchi, M. Tani, Z. Wang, K. Sakai, N. Wada, and M. Hangyo, Jpn. J. Appl. Phys. **35**, L1578 (1996); M. Tonouchi, M. Tani, Z. Wang, K. Sakai, S. Tomozawa, M. Hangyo, Y. Murakami, and S. Nakashima, Jpn. J. Appl. Phys., Part 1 35, 2624 (1996).

[Tono 02] M. Tonouchi, N. Kawasaki, T. Yoshimura, H. Wald, P. Seidel, Jpn. J. Appl. Phys. **41**, 706 (2002).

[vanE 89] M. Van Exter, C. Fattinger, D. Grischkowsky, *THz time-domain spectroscopy of water vapor*, Opt. Lett. **14**, 1128 (1989)

[Verg 96] S. Verghese, N. Zamdmer, Q. Hu, E. R. Brown, A. F"orster, Appl. Phys. Lett. **69**, 842 (1996)

[Verg 97] S. Verghese, K. A. McIntosh, E. R. Brown, Appl. Phys. Lett. **71**, 2743 (1997)

[Vinc 90] J. D. Vincent, *Fundamentals of Infrared Detector Operating and Testing*, Wiley Publishing, New York (1990)

[Wald 00] H. Wald, C. Steigmeier, S. Nashima, M. Tonouchi, M. Hangyo, Physica C **341-348**, 1899 (2000)

[Wald 02] H. Wald, H. Schneidewind, P. Seidel, M. Tonouchi, Physica C (2002)

[Wald 02a] H. Wald, F. Schmidt, P. Seidel, M. Tonouchi, Supercond. Sience and Techn. **15**, 1494 (2002)

[Walt 96] S. B. Waltman, L. W. Hollberg, K. A. McIntosh, E. R. Brown, Proc. SPIE **2842**, 55 (1996)

[Wang 93] H. H. Wang, J. F. Whitaker, A. Chin, J. Mazurowski, J. M. Ballingall, J. Electron. Mater. **22**, 1461 (1993)

[Wilk 00] I. Wilke, M. Khazan, C. T. Rieck, P. Kuzel, T. Kaiser, C. Jaekel, H. Kurz, J. of Appl. Phys. 87, No. 6, 2984 (2000)

[Witt 93] G. D. Witt, Mater. Sci. Eng. B **22**, 9 (1993)

[Wu 87] M. K. Wu, J. R. Ashburn, C. J. Torng, P. H. Hor, R. L. Meng, L. Gao, Z. J. Huang, Y. Q. Wang, C. W. Chu, Phys. Rev. Lett. **58**, 908 (1987)

[Yasu 91] H. Yasuoka, H. Mazaki, T. Terashima, Y. Bando, Physica C **175**, 192 (1991)

[Ye 95] J. Ye, K. Nakamura, *Superconducting and Superconducting Materials Technologies*, Ed. P. Vincenzini, Techna Srl, Italy (1995)

[Yesh 88] Y. Yeshurun, A. P. Malozemoff, Phys. Rev. Lett. **60**, 2202 (1988)

[Yu 87] J. Yu, J. Freeman, S. Massidda, *Novel Superconductivity* (S.A. Wolf and V. Z. Kresin, Eds.) , Plenum, New York (1987)

[Yu 92] R. C. Yu, B. Salamon, J. P. Lu, W. C. Lee, Phys. Rev. Lett. **69**, 1431 (1992)

[Zhan 92] X. C. Zhang, Y. Jin, K. Yang, L. J. Schowalter, Phys. Rev. Lett. **69**, 2303 (1992)

[Zhan 94a] Z. M. Zhang, A. Frenkel, J. of Superconductivity **7**, No. 6, 871 (1994)

[Zhao 98] Y. G. Zhao, S. B. Ogale, R. Shreekala, Z. W. Dong, S. P. Pai, M. Rajeswari, T. Venkatesan, W. L. Cao, W. Lu, C. Lee, J. Appl. Phys. **83**, 1531 (1998)

[Zhou 92] X. Q. Zhou, H. M. van Driel, W. W. Ruhle, J. Kuhl, K. Ploog, Phys. Rev. B **46**, 16148 (1992)

[Zibo 92] A. Zibold, K. Widder, H. P. Geserich, T. Scherer, P. Marienhoff, M. Neuhaus, W. Jutzi, A. Erb, G. Muller-Vogt, Appl. Phys. Lett. **61**, 345 (1992)

[Zima 60] J. M. Ziman, ″Electrons and Phonons″, Oxford University Press, London (1960)

[Zimm 91] W. Zimmermann, E. H. Brandt, M. Bauer, E. Seider, L. Genzel, Physica C **183**, 99 (1991)